



Defense Special Weapons Agency
Alexandria, VA 22310-3398



DSWA-TR-96-63

MIGHTY NORTH 1 Precision Test

James K. Gran
Mark A. Groethe
SRI International
333 Ravenswood Avenue
Menlo Park, CA 94025-3434

September 1997

Technical Report

DTIC QUALITY INSPECTED 2

CONTRACT No. DNA 001-93-C-0066

Approved for public release;
distribution is unlimited.

19970923 077

DESTRUCTION NOTICE:

Destroy this report when it is no longer needed.
Do not return to sender.

PLEASE NOTIFY THE DEFENSE SPECIAL WEAPONS
AGENCY, ATTN: CSTI, 6801 TELEGRAPH ROAD,
ALEXANDRIA, VA 22310-3398, IF YOUR ADDRESS IS
INCORRECT, IF YOU WISH IT DELETED FROM THE
DISTRIBUTION LIST, OR IF THE ADDRESSEE IS NO
LONGER EMPLOYED BY YOUR ORGANIZATION.



REPORT DOCUMENTATION PAGE

Form Approved

OMB No. 0704-0188

Public reporting burden for this collection of information is estimated to average 1 hour per response including the time for reviewing instructions, searching existing data sources, gathering and maintaining the data needed, and completing and reviewing the collection of information. Send comments regarding this burden estimate or any other aspect of this collection of information, including suggestions for reducing this burden, to Washington Headquarters Services Directorate for Information Operations and Reports, 1215 Jefferson Davis Highway, Suite 1204, Arlington, VA 22202-4302, and to the Office of Management and Budget, Paperwork Reduction Project (0704-0188), Washington, DC 20503.

1. AGENCY USE ONLY (Leave blank)			2. REPORT DATE 970901	3. REPORT TYPE AND DATES COVERED Technical 930413 - 961031
4. TITLE AND SUBTITLE MIGHTY NORTH 1 Precision Test			5. FUNDING NUMBERS C - DNA 001-93-C-0066 PE - 62715H PR - AC TA - AB WU - DH00023	
6. AUTHOR(S) James K. Gran and Mark A. Groethe (SRI International); Dan Chitty (Applied Research Associates); and John G. Trulio (Applied Theory, Inc.)				
7. PERFORMING ORGANIZATION NAME(S) AND ADDRESS(ES) SRI International 333 Ravenswood Avenue Menlo Park, CA 94025-3434			8. PERFORMING ORGANIZATION REPORT NUMBER PYU-4631	
9. SPONSORING/MONITORING AGENCY NAME(S) AND ADDRESS(ES) Defense Special Weapons Agency 6801 Telegraph Road Alexandria, VA 22310-3398 PMT/Sensem			10. SPONSORING/MONITORING AGENCY REPORT NUMBER DSWA-TR-96-63	
11. SUPPLEMENTARY NOTES This work was sponsored by the Defense Special Weapons Agency under RDT&E RMC Code B4662D AC AB 00023 4300A AC 25904D.				
12a. DISTRIBUTION/AVAILABILITY STATEMENT Approved for public release; distribution is unlimited.			12b. DISTRIBUTION CODE	
13. ABSTRACT (Maximum 200 words) MIGHTY NORTH 1 was a precision test performed on a 0.4-m-diameter lined tunnel in a 2-m-cube of jointed limestone made from over 4000 50-mm-square x 0.6- to 1.2-m-long limestone bricks. The test article was embedded in a concrete testbed and loaded with an explosively produced, 100 MPa, cylindrical, stress wave. The velocity around the boundary of the jointed limestone test article was measured with 22 accelerometers and these data were used to generate a continuous velocity boundary condition for computational simulations. Additional internal instrumentation measured brick stress, brick slip, and tunnel closure. All gages provided clear and credible measurements, except the closure gages, which were inoperable at the time of the test. Stress at the tunnel depth was about 75 MPa. Very little horizontal slip occurred at the locations of the slip gages (at the interface tangent to the crown). The mechanism of response was vertical cleavage fractures emanating upward from the springlines, with the bricks between the cleavage planes moving downward about 10 mm relative to the brick outside. The cleavage planes also extended below the springlines, but the relative displacement was only about 2 mm, with the bricks outside the cleavage planes moving downward relative to those between the planes. Posttest liner deformation was -2.5% (closure) at the crown-invert diameter and +1.3% (opening) at the springlines.				
14. SUBJECT TERMS Tunnels MIGHTY NORTH 1			Precision Test Jointed Limestone Ground Waves	15. NUMBER OF PAGES 84
				16. PRICE CODE
17. SECURITY CLASSIFICATION OF REPORT UNCLASSIFIED		18. SECURITY CLASSIFICATION OF THIS PAGE UNCLASSIFIED	19. SECURITY CLASSIFICATION OF ABSTRACT UNCLASSIFIED	20. LIMITATION OF ABSTRACT SAR

UNCLASSIFIED

SECURITY CLASSIFICATION OF THIS PAGE

CLASSIFIED BY:

N/A since Unclassified.

DECLASSIFY ON:

N/A since Unclassified.

CLASSIFICATION OF THIS PAGE

UNCLASSIFIED

SUMMARY

The primary objective of the MIGHTY NORTH 1 precision test was to provide data to develop and evaluate computational models for tunnels in highly jointed rock. This objective required sufficient characterization of the jointed test article and adequate measurement of both the boundary conditions on the test article and the deformation of the jointed limestone.

Figure S-1 shows the test article. Its overall dimensions were approximately 2.15 m tall by 2.15 m wide by 2.4 m long. It was constructed with about 4000 bricks in 42 layers and contained a 406-mm-diameter cylindrical opening that was lined with an aluminum shell. The 42 layers of bricks were stacked on a cradle comprising a 150-mm-thick, lightly reinforced, concrete slab supported underneath by compacted sand and three, large, steel I-beams running transversely to the length of the bricks. Measurements indicated an average gap between layers of 163 μm , about 0.3% of the thickness of a brick (standard deviation = 32 μm). The entire test article was encased in a 150-mm-thick layer of lightly reinforced concrete. This assembly was supported and braced with steel beams and channels. The 50-ton unit was shipped to the Permanent High Explosive Test Site (PHETS) via crane and truck.

The test article was embedded in a large concrete testbed with an explosive load applied to the top surface. We estimated the mechanical properties of the jointed limestone test article and selected a concrete with similar properties for the testbed. The top surface of the testbed was formed into a cylindrical trough so that the surface pressure produced a divergent ground shock engulfing the test article.

We performed laboratory tests to characterize the physical and mechanical properties of both the intact limestone and the joints formed at the interface of adjoining blocks. To define the strength of the intact limestone, we conducted a series of conventional triaxial compression and triaxial extension tests. The shear strength of the joints was determined over the relevant range of normal stresses by a series of triaxial compression tests on specimens with a single joint oriented at 30° to the specimen axis. The normal compressibility of the joint surfaces was determined by unconfined compression tests on specimens with a single joint oriented at 90° to the specimen axis. We employed special specimen preparation procedures to ensure that the joint surfaces subjected to laboratory testing were truly representative of the joints in the test article.

The motions at the perimeter of the test article were measured at 14 locations using piezoresistive accelerometers mounted in shock-isolated canisters to limit the peak acceleration signals. Extremely high

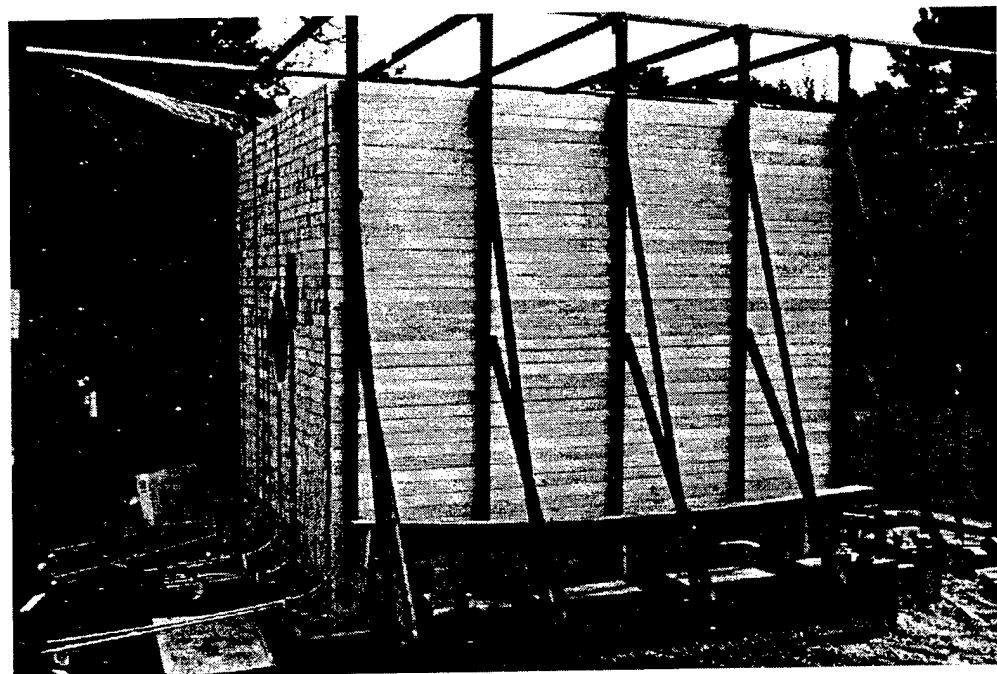
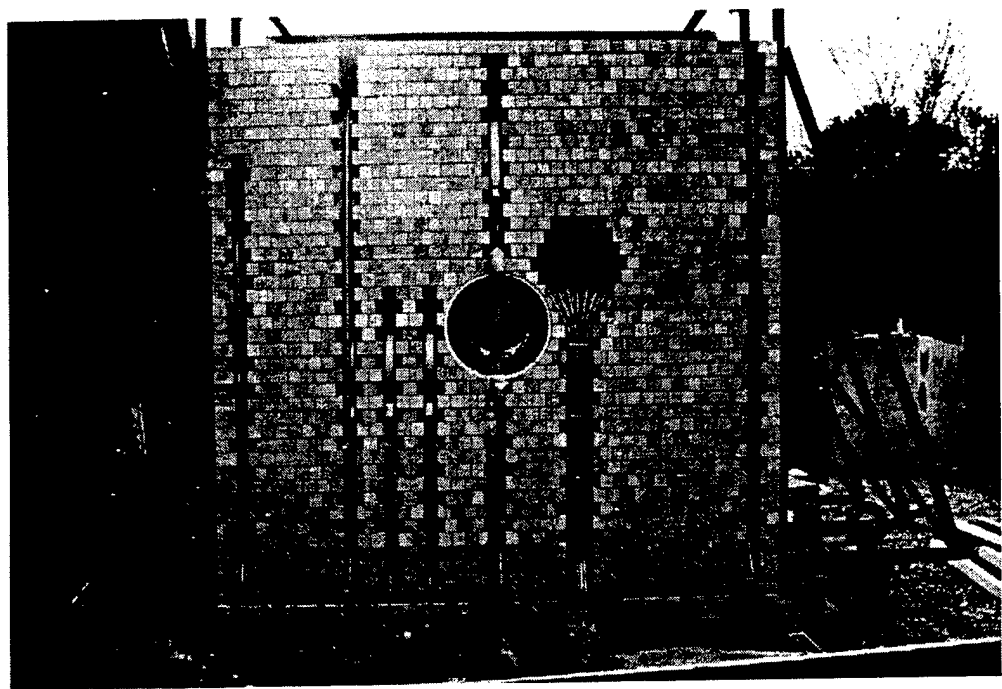
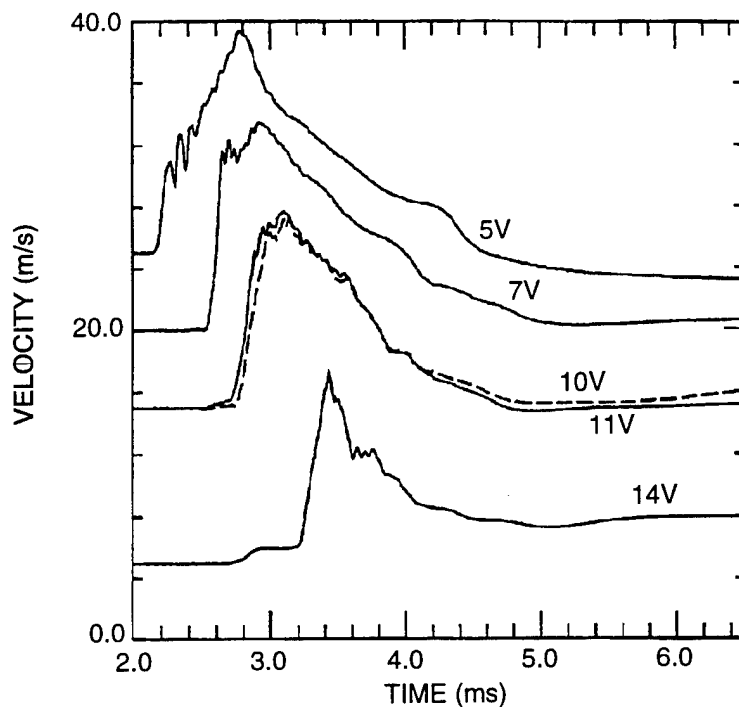
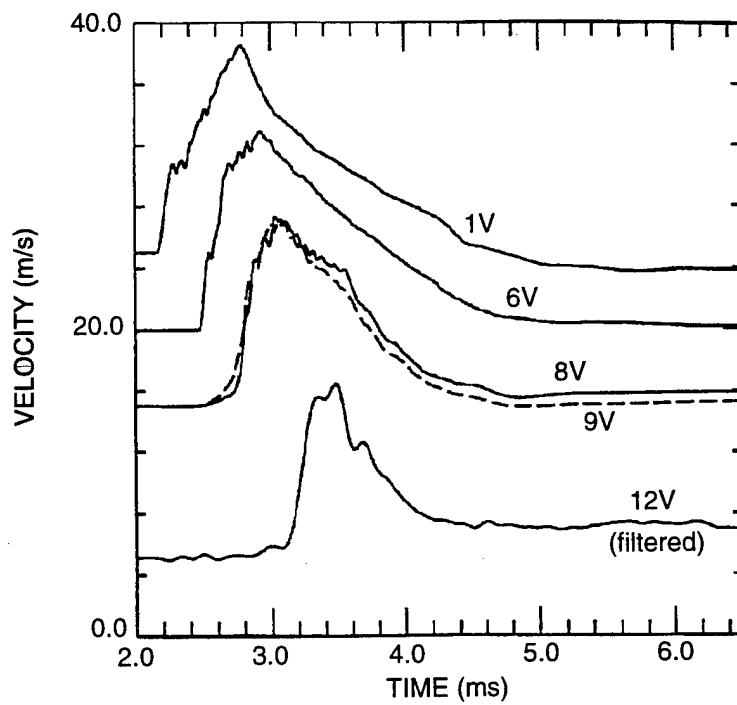


Figure S-1. MIGHTY NORTH 1 jointed limestone test article.



(a) North side



(b) South side

Figure S-2. Composite of test article vertical velocities.

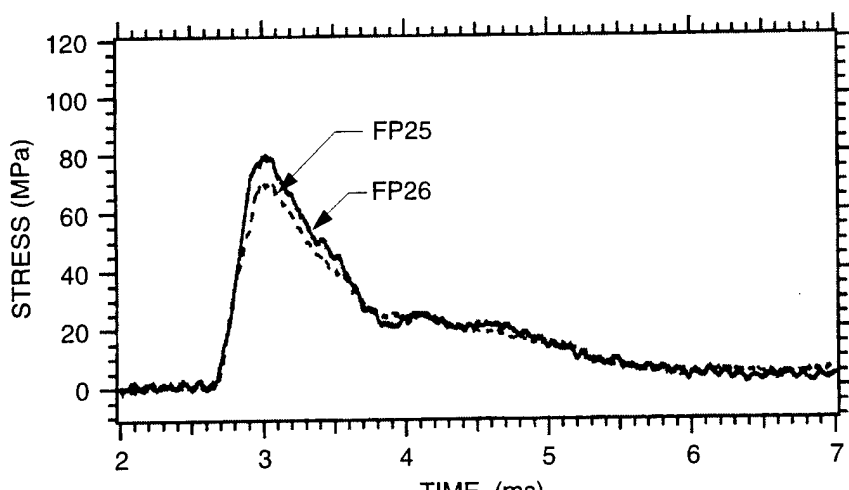
quality data were obtained from the accelerometers. Figure S-2 is a composite plot illustrating the excellent precision and symmetry obtained from the vertical velocities down the two sides of the test article.

The primary purpose of the velocity measurements was to provide data from which to define a continuous velocity boundary condition for computational analyses of the experiment. A symmetric velocity boundary condition was created by reconstructing the material velocity field all along the two-dimensional boundary defined by the locations of the accelerometers (slightly inboard of the actual limestone/concrete interface).

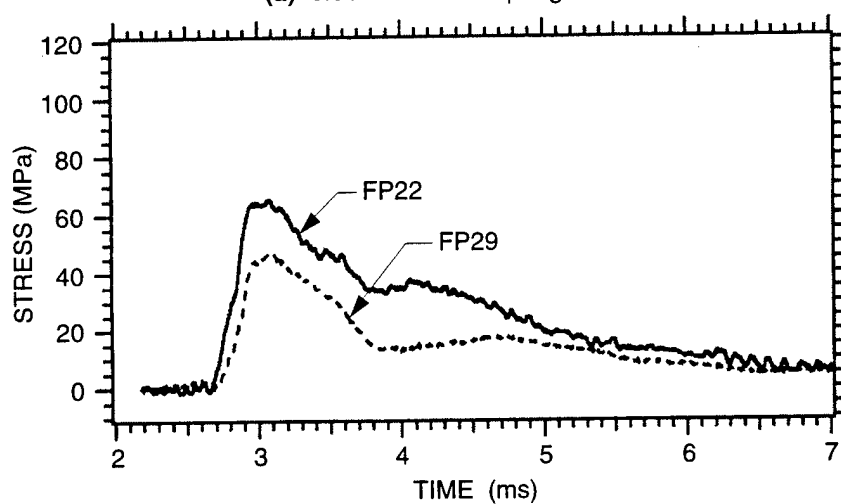
Limestone stresses were measured with flatpack stress gages, installed in the limestone bricks by machining a channel in the bottom half of a brick and bonding the gage and the brick halves together with epoxy. Figure S-3 shows the stresses measured adjacent to the springline and about 1 tunnel diameter from the springline on both sides of the tunnel. The three sets of records indicate good symmetry in the stress wave.

Following the test, the concrete surrounding the test article was removed so that the damage to the limestone bricks and the deformed shape of the liner could be observed. The bricks were removed layer by layer and we measured the profile of each layer. The locations of all visible cracks were noted. The liner was removed and its deformed shape was measured all along its length. These data provide invaluable insight into the response mechanisms of an opening in jointed rock. Only the surface of the liner showed evidence of limestone compaction. Almost all the brick damage was in the form of vertical splitting down a brick centerline, typically running the entire length of a brick. However, this damage was concentrated around the opening. Unsplit bricks removed from the test article had the same dimensions (statistically) as pretest.

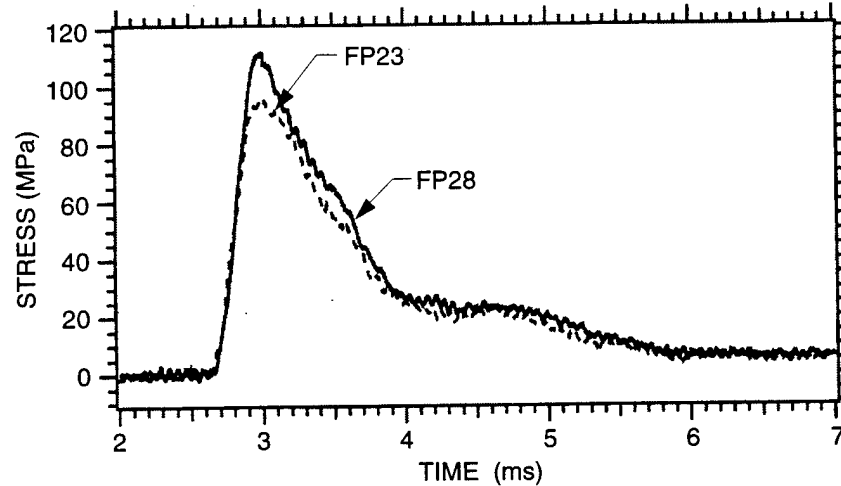
The displacement and fracture patterns that we observed and quantified are of vertical cleavage emanating upward from the springlines, forming a chimney of bricks separated from the rest. The cleavage fractures tended slightly toward each other and disappeared before reaching the top surface. Figure S-4 shows the vertical displacement patterns determined from the posttest measurements at a section near the miplane of the test article. In this figure, the relative vertical displacements have been amplified by a factor of 2 and no horizontal displacements are included. Above the springlines, the relative displacement at the cleavage planes was about 10 mm, with the bricks within the chimney moving downward relative to the rest of the test article. The cleavage planes also extended downward from the springlines, but only a few layers. In this region, the relative displacement was about 2 mm, with the material outside the cleavage planes moving downward relative to the material between the cleavage planes. The sum of the shear displacement above the opening and below the opening (about 12 mm) agrees very well with the average crown-invert deformation of the liner.



(a) 0.36 m from the springline



(b) 0.21 m from the springline



(c) 0.05 m from the springline

Figure S-3. Vertical stresses 25 mm above the plane of the springline.

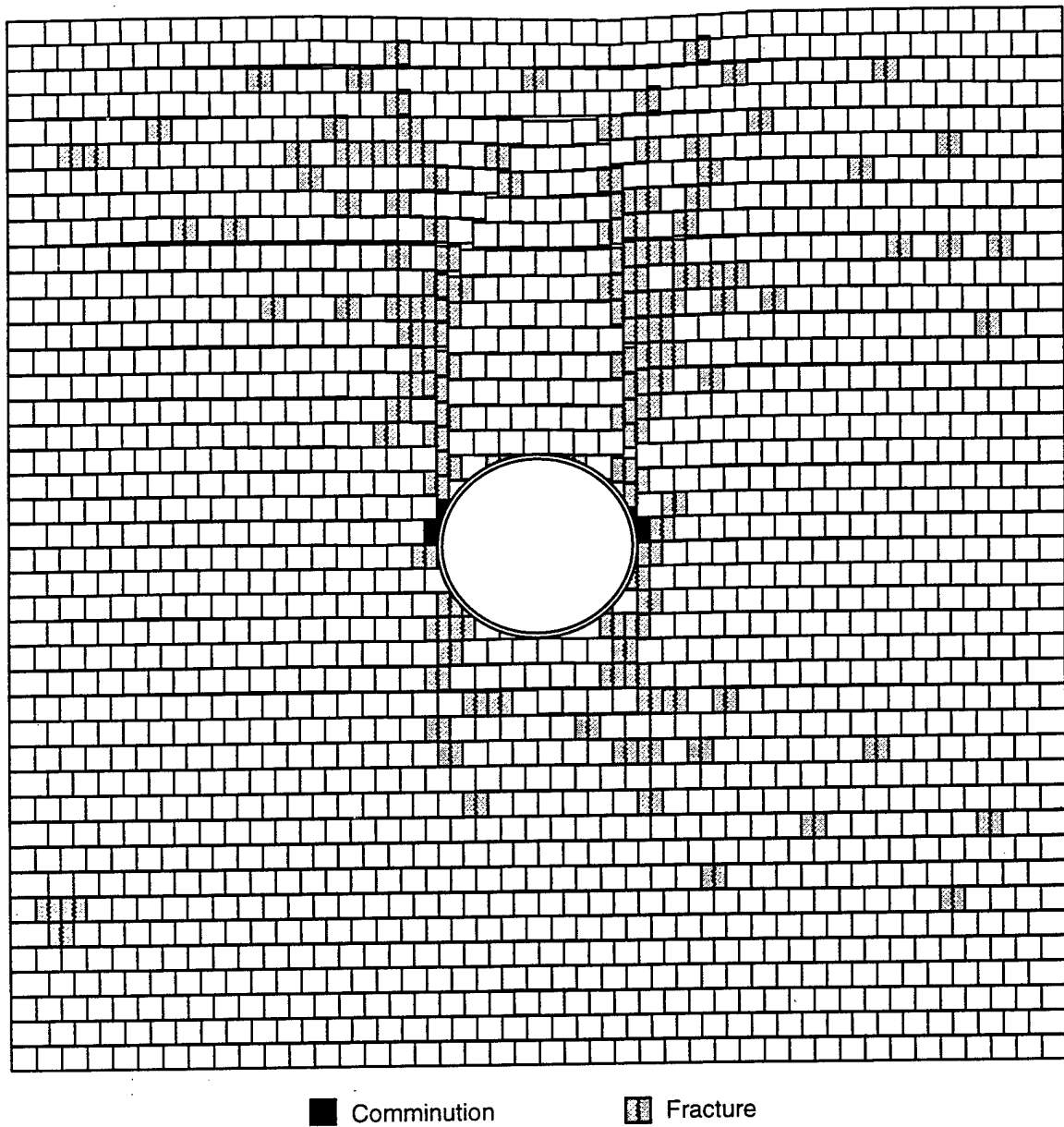


Figure S-4. MIGHTY NORTH 1 jointed limestone deformation and damage at $x = +305$ mm.
(Vertical Displacement Scale Factor = 2)

Over the central half of the length of the tunnel liner, the average crown-invert deflection was -10.31 mm (closure) with a standard deviation of 0.72 mm. The average springline diameter change was +5.43 mm (opening) with a standard deviation of 1.40 mm. Related to the original outer diameter, these measurements give an average vertical closure of 2.5% and an average springline opening of 1.3%.

The MIGHTY NORTH I event was an example of the DNA community's ability to design and execute precision tests involving explosive effects on rock structures. Technical expertise, combined with a commitment to quality, resulted in an extremely successful experiment. The precision with which the loading was applied and measured, and the precision with which the test article was built and its response measured provide a data set that is invaluable to developers of computational models for the dynamic response of structures in jointed rock.

PREFACE

The MIGHTY NORTH precision test series was conceived by Dr. Paul Senseny, DNA. He was the technical monitor of this contract and was instrumental in guiding the effort to a scientific and engineering success. Invaluable programmatic support and technical contributions were also provided by Dr. Eric Rinehart, FC/DNA.

This project was a team effort at many levels. The test article was designed, built, and fielded by SRI International. The accelerometers and slip gages were designed, fabricated, installed, fielded, and analyzed by the S-Cubed Division of Maxwell Laboratories. The stress gages and tunnel closure gages were designed, fabricated, installed, fielded, and analyzed by SRI. Limestone and brick joint properties were measured by Applied Research Associates. The velocity boundary condition was produced by Applied Theory, Inc. Posttest inspection was performed by SRI and S-Cubed.

At SRI, the project supervisor was Dr. James K. Gran. The project leader was Gary R. Greenfield. Fabrication of the test article was accomplished by Mario Oyola and Anthony Ware. Flatpack stress gages were built by Robert Boyle. Tunnel closure gages were developed by Rich Klopp. Instrumentation fielding was performed by Dan Walter and Paul DeCarli. Engineering analysis was performed by Alex Florence. Data analysis was performed by Bonita Lew. Photographic support was supplied by Ken Stepleton. Technical illustrations were prepared by Lee Gerrans.

At S-Cubed, the project supervisor was Dr. Carl F. Petersen. The project leader was Mark A. Groethe. Accelerometer packages and EM slip gages were built and installed by Lee Prasser. Instrumentation fielding was performed by John Morris.

At ARA, the project supervisor was Mr. Scott Blouin. The project leader was Dan Chitty.

At ATI, the project supervisor was Dr. John G. Trulio. Assistance was provided by Neil Perl and Jim Workman.

The success of the work reported here would not have been possible without the excellent contributions to the field test design and execution by many people at Field Command DNA, the PHETS, Titan Research & Technology, Applied Research Associates, U.S. Army Corps of Engineers Waterways Experiment Station, and SRI.

CONVERSION TABLE

Conversion factors for U. S. Customary to metric (SI) units of measurement

MULTIPLY TO GET	BY	TO GET DIVIDE	
angstrom	1.000 000	X E -10	meters (m)
atmosphere (normal)	1.013 25	X E +2	kilo pascal (kPa)
bar	1.000 000	X E +2	kilo pascal (kPa)
barn	1.000 000	X E -28	meter ² (m ²)
British thermal unit (thermochemical)	1.054 350	X E +3	joule (J)
calorie (thermochemical)	4.184 000		joule (J)
cal (thermochemical)/cm ²	4.184 000	X E -2	mega joule/m ² (MJ/m ²)
curie	3.700 000	X E +1	*giga becquerel (GBq)
degree (angle)	1.745 329	X E -2	radian (rad)
degree Fahrenheit	$T_K = (T^{\circ}F + 459.67)/1.8$		degree kelvin (K)
electron volt	1.602 19	X E -19	joule (J)
erg	1.000 000	X E -7	joule (J)
erg/second	1.000 000	X E -7	watt (W)
foot	3.048 000	X E -1	meter (m)
foot-pound-force	1.355 818		joule (J)
gallon (U.S. liquid)	3.785 412	X E -3	meter ³ (m ³)
inch	2.540 000	X E -2	meter (m)
jerk	1.000 000	X E +9	joule (J)
joule/kilogram (J/kg) (radiation dose absorbed)	1.000 000		Gray (Gy)
kilotons	4.183		terajoules
kip (1000 lbf)	4.448 222	X E +3	newton (N)
kip/inch ² (ksi)	6.894 757	X E +3	kilo pascal (kPa)
ktap	1.000 000	X E +2	newton-second/m ² (N·s/m ²)
micron	1.000 000	X E -6	meter (m)
mil	2.540 000	X E -5	meter (m)
mile (international)	1.609 344	X E +3	meter (m)
ounce	2.834 952	X E -2	kilogram (kg)
pound-force (lbs avoirdupois)	4.448 222		newton (N)
pound-force inch	1.129 848	X E -1	newton-meter (N · m)
pound-force/inch	1.751 268	X E +2	newton-meter (N/m)
pound-force/foot ²	4.788 026	X E -2	kilo pascal (kPa)
pound-force/inch ² (psi)	6.894 757		kilo pascal (kPa)
pound-mass (lbf avoirdupois)	4.535 924	X E -1	kilogram (kg)
pound-mass-foot ² (moment of inertia)	4.214 011	X E -2	kilogram·meter ² (kg·m ²)
pound-mass-foot ³	1.601 846	X E +1	kilogram/meter ³ (kg/m ³)
rad (radiation dose absorbed)	1.000 000	X E -2	**Gray (Gy)
roentgen	2.579 760	X E -4	coulomb/kilogram (C/kg)
shake	1.000 000	X E -8	second (s)
slug	1.459 390	X E +1	kilogram (kg)
torr (mm Hg, 0° C)	1.333 22	X E -1	kilo pascal (kPa)

*The becquerel (Bq) is the SI unit of radioactivity; 1 Bq = 1 event/s.

**The Gray (Gy) is the SI unit of absorbed radiation.

TABLE OF CONTENTS

Section	Page
SUMMARY	iii
PREFACE	x
CONVERSION TABLE	xi
FIGURES	xiii
1 INTRODUCTION	1
1.1 BACKGROUND	1
1.2 OBJECTIVES	2
1.3 MIGHTY NORTH 1 PRECISION TEST	2
2 EXPERIMENT	4
2.1 OVERVIEW	4
2.2 MATERIAL PROPERTIES	6
2.2.1 Limestone Properties	6
2.2.2 Joint Properties	10
2.2.3 Jointed Limestone Tests	14
2.2.4 Liner Properties	18
2.3 TEST ARTICLE CONSTRUCTION	18
2.4 INSTRUMENTATION	22
2.4.1 Instrumentation Plan	22
2.4.2 Accelerometers	26
2.4.3 Closure Gages	28
2.4.4 Stress Gages	31
2.4.5 Joint Slip Gages	33
3 RESULTS	35
3.1 GENERAL	35
3.2 VELOCITIES	35
3.3 BOUNDARY CONDITIONS	39
3.4 CLOSURES	42
3.5 STRESSES	43
3.6 JOINT SLIP	48
3.7 POSTTEST OBSERVATIONS	53
4 CONCLUSIONS AND RECOMMENDATIONS	62
4.1 CONCLUSIONS	62
4.2 RECOMMENDATIONS	62
5 REFERENCES	64

FIGURES

Figure		Page
S-1	MIGHTY NORTH 1 jointed limestone test article	iv
S-2	Composite of test article vertical velocities	v
S-3	Vertical stresses 25 mm above the plane of the springline	vii
S-4	MIGHTY NORTH 1 jointed limestone deformation and damage at $x = +305$ mm (vertical displacement scale factor = 2)	viii
1-1	MIGHTY NORTH test concept	3
2-1	MIGHTY NORTH test geometry	5
2-2	Triaxial compression stress-strain relations for Salem limestone	7
2-3	Triaxial compression pressure-volume relations for Salem limestone	8
2-4	Comparison of joint strength with strength of intact limestone	9
2-5	Triaxial extension stress-strain relations for Salem limestone	11
2-6	Strength envelopes from triaxial extension and triaxial compression tests	12
2-7	Triaxial compression tests on SRI sawn joints in Salem limestone	13
2-8	Normal compressibility of SRI sawn joint	15
2-9	Three unconfined compression tests on stacks of bricks	16
2-10	Two unconfined compression tests on an assemblage of bricks	17
2-11	Aluminum tensile test results	19
2-12	MIGHTY NORTH 1 jointed limestone test article	20
2-13	Placement of MIGHTY NORTH 1 test article in testbed	23
2-14	Elevation view of the gage array in the limestone	24
2-15	Plan view of the gage array in the limestone	25
2-16	Shock isolated accelerometer	27

FIGURES (Continued)

Figure		Page
2-17	Calibration tests to establish cross-axis sensitivity and zero offset susceptibility	29
2-18	Tunnel closure gages	30
2-19	Installation of flatpack stress gage in a 51- x 51-mm limestone brick	32
2-20	Electromagnetic slip gage brick	34
3-1	Four vertical velocities measured at the tunnel depth	36
3-2	Comparison of test article vertical velocities	37
3-3	Comparison of test article horizontal velocities	38
3-4	Zero-shifts and impact of correction	40
3-5	Decomposition of velocity pulses into phases	41
3-6	Circumferential variation of liner deformation	44
3-7	Axial variation of liner deformation	45
3-8	Typical resistance histories	46
3-9	Vertical stresses 25 mm above the plane of the springline	47
3-10	Vertical stress on the centerline, 0.84 and 0.53 above the tunnel axis (0.64 and 0.33 m above the crown)	49
3-11	EM slippage data	50
3-12	Posttest slip at the EM slip gage interface	51
3-13	Horizontal slip measurements	52
3-14	MIGHTY NORTH 1 jointed limestone faulting above the tunnel	54
3-15	MIGHTY NORTH 1 jointed limestone deformation and damage at x = +305 mm (vertical displacement scale factor = 2)	56
3-16	MIGHTY NORTH 1 jointed limestone deformation and damage at x = +305 mm (vertical displacement scale factor = 0)	57

FIGURES (Continued)

Figure		Page
3-17	MIGHTY NORTH jointed limestone test article posttest horizontal strains	58
3-18	Average symmetric cumulative slip measurements	59
3-19	Simplified kinematic interpretation of the slip pattern	61

SECTION 1

INTRODUCTION

1.1 BACKGROUND.

The failure mechanism of deep, underground, cylindrical tunnels in rock subjected to a strong dynamic loading from a large explosion is material failure at the springlines. Laboratory-scale tests of tunnels in intact limestone with static loading (Simons, et al, 1992) and with dynamic loading with pulse durations long compared to tunnel transit times (Klopp, et al, 1994) produced shear faults emanating from the springlines and diverting from each other at about 20°. The shear strength of the rock, especially at confinement pressures about equal to the hydrostatic strength of the liner, is the most important material parameter in tunnel response. Nearly all geologic formations are jointed or layered on some scale, and large underground facilities typically cross many discontinuities, hereafter referred to as joints. Joints significantly complicate the response of the rock mass.

A common approach for predicting tunnel response in jointed rocks is to reduce the rock strength (from its intact strength) as a function of the number of joints per tunnel diameter. This approach was based on standard design procedures for civil structures in rock and was developed to help explain damage to structures in underground tunnels (UGTs) in granite that experienced damage considerably greater than expected. This treatment of the effect of joints on tunnel response may be simplistic, because the relationship is based only on correlations taken from field data and lacks an account of the mechanics. In addition, this treatment cannot explain results from laboratory and field tests on structures in media with prepared joints. For example, laboratory tests performed at SRI show that the orientation of joints has a strong effect on tunnel closure (Senseney and Lindberg, 1979). Parallel bedding joints have little or no effect on tunnel closure if they are oriented to within 30 degrees of loading normal, but joints at 45 degrees do increase tunnel closure.

In a previous project, SRI studied small-scale tunnels in jointed material within grout cylinders. The joints were either single sets of parallel joints or orthogonal sets of parallel joints. The ratio of the number of joints to the tunnel diameter varied from 5 to 10. Posttest inspection showed that joint slipping tended to occur locally and that block motion was typically limited to a few small blocks. We also observed that material failure occurred as well as block motion. For example, in models with sets of parallel joints, cracks occurred across the plates. Furthermore, contrary to the simple strength reduction approach, tunnel deformation decreased with increasing joint-to-diameter ratios.

1.2 OBJECTIVES.

To better understand the role of joints on tunnel deformation, DNA began a series of precision tests named MIGHTY NORTH. The objectives of these tests are to

- (1) Investigate effects of joint orientation, roughness, and spacing on tunnel deformation
- (2) Provide data to develop and evaluate computational models for tunnels in highly jointed rock.

For both objectives, the loading is restricted to cylindrically divergent dynamic loading, making the MIGHTY NORTH test series a set of "benchmark experiments" akin to the recently completed series of "benchmark calculations" on tunnels in jointed media (Simons, 1993; Senseny and Simons, 1994).

Figure 1-1 shows the physical concept of the MIGHTY NORTH tests. The explosive charge produces a stress wave, and the length of the simulator (in the direction out of the page) is sufficient to produce a plane-strain environment on the test articles. The test articles are approximately 2 m on each side, and more than one can be tested in the same test by making the explosive charge and testbed longer.

By applying the same loading to several test articles that differ in joint orientation, roughness, or spacing, the effects of these parameters on tunnel deformation can be characterized (i.e., an empirical relation between tunnel deformation and joint characteristics can be obtained for this loading condition and range of parameters). This is Objective 1.

Objective 2 is more scientific and more challenging. It requires sufficient characterization of the jointed test articles and adequate measurement of both the boundary conditions on the test articles and the deformation of the jointed limestone to properly develop and evaluate computational models. That is, valid computational models must be able to start with the boundary conditions at the perimeter of the jointed limestone test articles and predict, with acceptable accuracy, the tunnel response. In addition, the tunnel response must be predicted accurately. To satisfy this condition, the computational model must be consistent with measured physical properties of the jointed limestone and the predictions consistent with measured stresses and motions in the jointed limestone.

1.3 MIGHTY NORTH 1 PRECISION TEST.

This report describes the MIGHTY NORTH 1 precision test in which a single test article made of jointed limestone was tested. The test article was design and fabricated at SRI and shipped to the DNA Permanent High Explosive Test Site (PHETS) on White Sands Missile Range (WSMR) for the test. Instrumentation in the test article was provided by SRI and S-Cubed Division of Maxwell Laboratories. Material characterization was performed by Applied Research Associates. Data analysis was performed by Applied Theory, Inc.

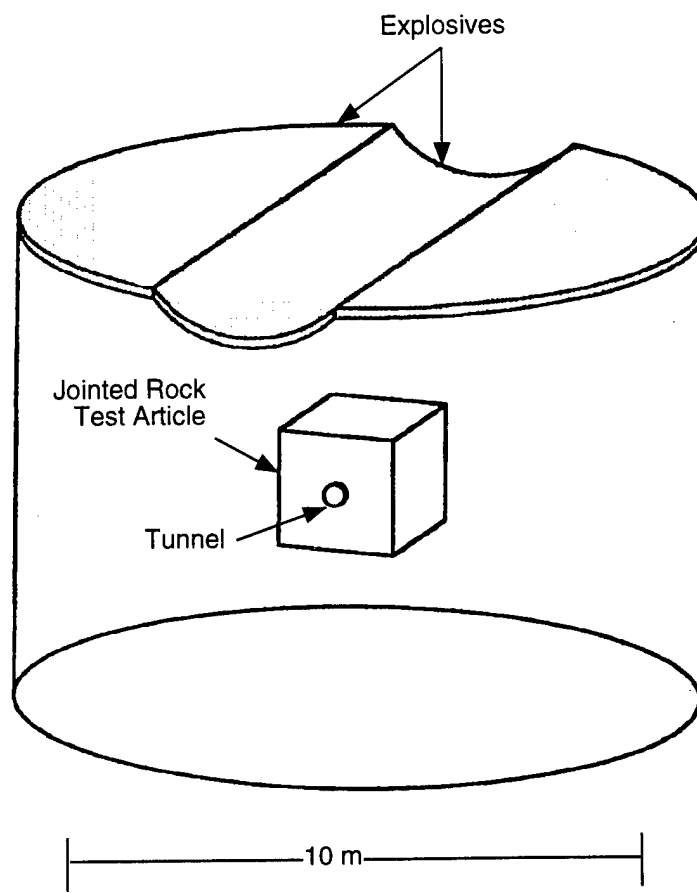


Figure 1-1. MIGHTY NORTH test concept.

SECTION 2

EXPERIMENT

2.1 OVERVIEW.

The test and model designs were motivated by an earlier numerical study (Simons, 1993; Senseny and Simons, 1994) and incorporate the "stack-of-bricks" model for jointed rock masses. This conceptual model, in which the intact rock and joint properties (such as orientation, spacing, and continuity) are approximated by a stack of bricks or irregular blocks, is the basis for all mathematical models for mechanical behavior of jointed rock masses in which the joints are treated explicitly rather than being smeared out to produce an "effective continuum."

The jointed rock test article was made of over 4000 limestone bricks, with each brick nominally 51 mm square and 0.6 to 1.2 m long. The bricks were stacked into a rectangular prism 2.1 m square and 2.4 m long with a central, 0.4 m diameter, circular hole lined with a thin aluminum tube. Although apparently large, the model size was close to the economical and technical optimum. The limestone bricks are the smallest commercially produced by quarries. Our instrumentation, developed through an intensive program to improve instrumentation for measurements of rock behavior (described later), was as miniature as has been developed for field testing.

Figure 2-1 shows the geometry of the experiment, performed at the DNA PHETS. The jointed limestone test article was placed in a deep pit that was later filled with concrete. The properties of the concrete were selected to approximately match the estimated strength and mechanical impedance of the jointed limestone. HJC-7 concrete with 10 mm maximum aggregate and nominally 34 MPa unconfined strength was used. The top surface of the concrete testbed was formed to include a cylindrical section. The entire top surface of the concrete pit was covered with about 3.5 Mg (TNT equivalent) of Iremite and Dilute Explosive Tiles (DET), detonated in a timed sequence to produce a cylindrically diverging stress wave (Goodfellow and Rinehart, 1995). Measurements of surface pressure, particle velocity, and time-of-arrival demonstrated that the explosive pulse was symmetric, nearly perfectly timed, and matched nearly exactly the test specification. Stress and velocity gages embedded in the concrete at the depth of the test article confirmed the symmetry, cylindrical divergence, and match to the test specification. The stress wave at the depth of the top of the test article had a radius of 4.4 m, a rise time of about 500 μ s, a peak stress of about 100 MPa, a peak particle velocity of about 14 m/s, a total radial displacement of about 25 mm, and peak circumferential strain of about 0.6%. This divergent dynamic environment was sufficient to exercise intact

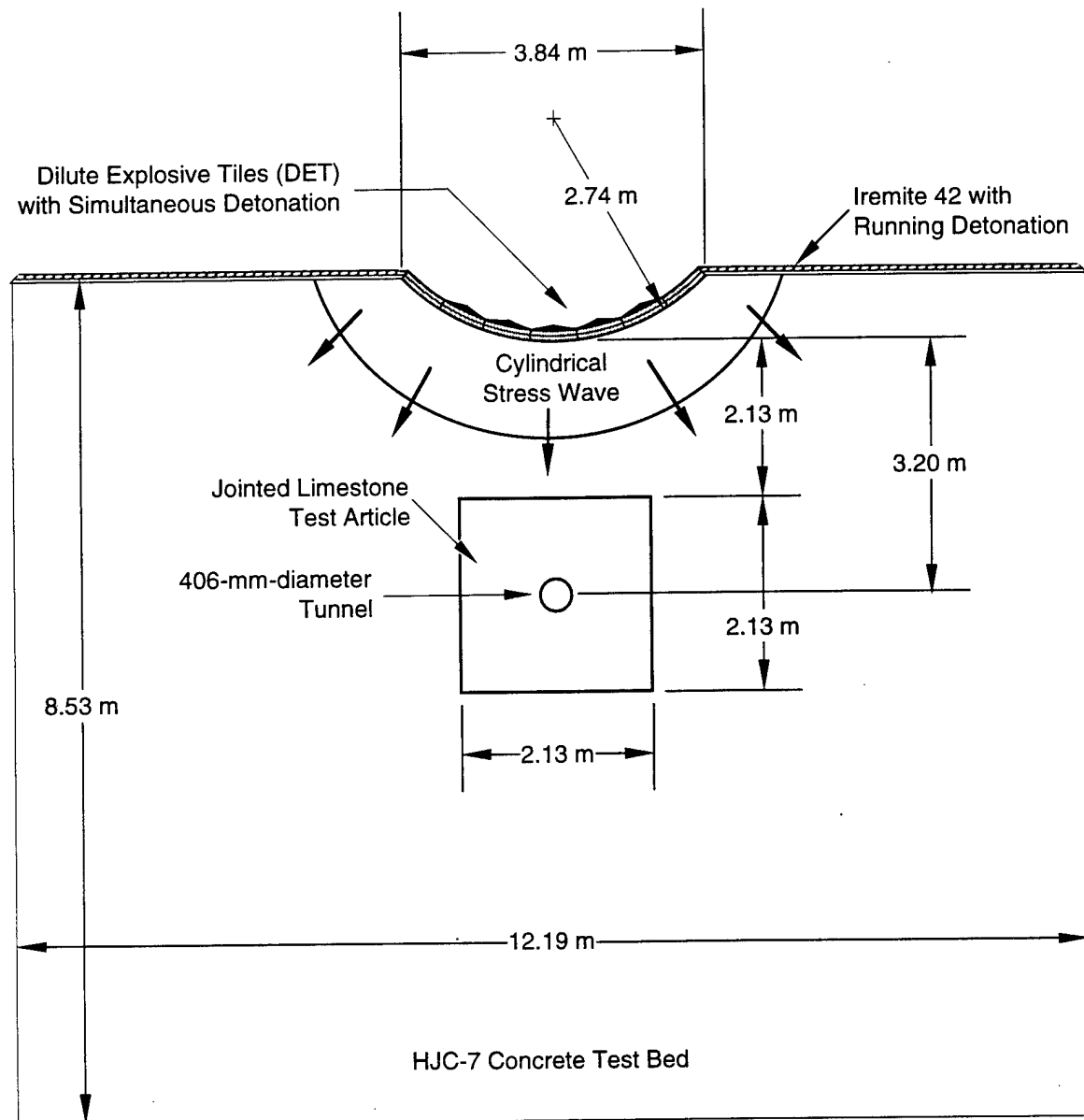


Figure 2-1. MIGHTY NORTH 1 test geometry.

rock comminution, joint slip, intact rock fracture, and permanent deformation of the lined opening in the jointed limestone test article.

2.2 MATERIAL PROPERTIES.

2.2.1 Limestone Properties.

The test article was constructed of porous limestone from the Salem formation near Bedford, Indiana USA. This material was thoroughly tested and Cap model parameters were determined by Fossum, et al. (1995). For completeness, additional laboratory tests were performed in this project to characterize the physical and mechanical properties of both the intact limestone and the joints formed at the interface of adjoining blocks. The index properties of the intact material, based on standard laboratory tests, are summarized in Table 2-1.

Table 2-1. Properties of Intact Salem Limestone.

<u>Property</u>	<u>Values</u>
Dry Bulk Density	2.21 - 2.34 Mg/m ³
Grain Density	2.71 Mg/m ³
Porosity	0.137 - 0.185
Unconfined Compressive Strength	50 - 56 MPa
Elastic Modulus	29 - 31 GPa
Poisson's Ratio	0.23 - 0.25

To define the strength of the intact limestone, a series of conventional triaxial compression tests was conducted at constant confining pressures ranging from 1 to 50 MPa. Figures 2-2 and 2-3 are composite plots of the results of these tests. One shows the axial and radial strains plotted against stress difference (the increment of axial stress above the confining pressure), and the other presents the relationship between mean stress (the average of three principal stresses) and volumetric strain.

The limestone exhibits a brittle-ductile transition at approximately 35 MPa confining pressure. The intact strengths derived from the triaxial compression tests in the brittle regime (i.e., at confining pressures up to 35 MPa) are represented by the solid line in Figure 2-4, which is a strength envelope of the form recommended by Hoek and Brown [1980], with parameters $m_j = 4.8$, $s = 1.0$, and $\sigma_c = 56$ MPa. Because the strengths of joints are best represented in terms of normal and shear stresses, the Hoek and Brown strength envelope has been transformed into Mohr's circle space for direct comparison.

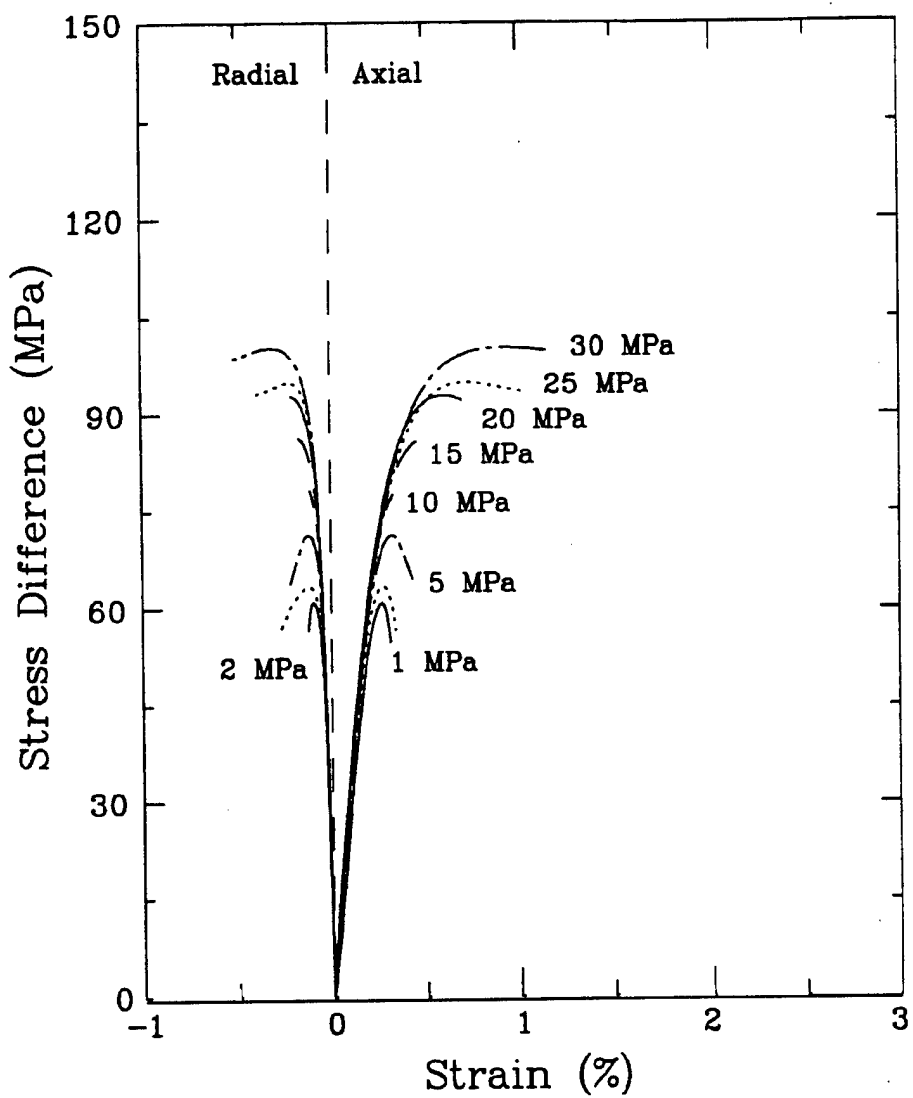


Figure 2-2. Triaxial compression stress-strain relations for Salem limestone.

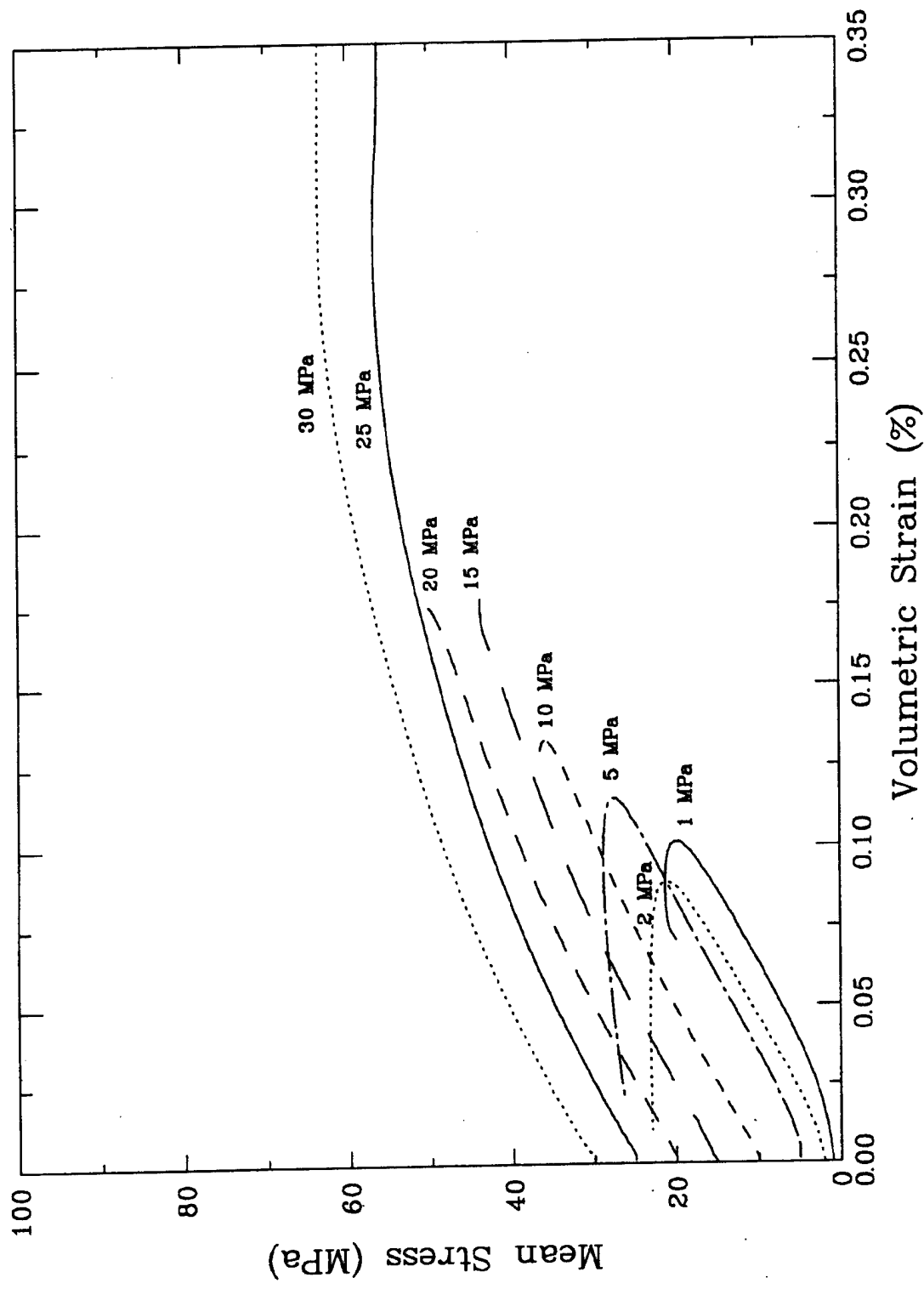


Figure 2-3. Triaxial compression pressure-volume relations for Salem limestone.

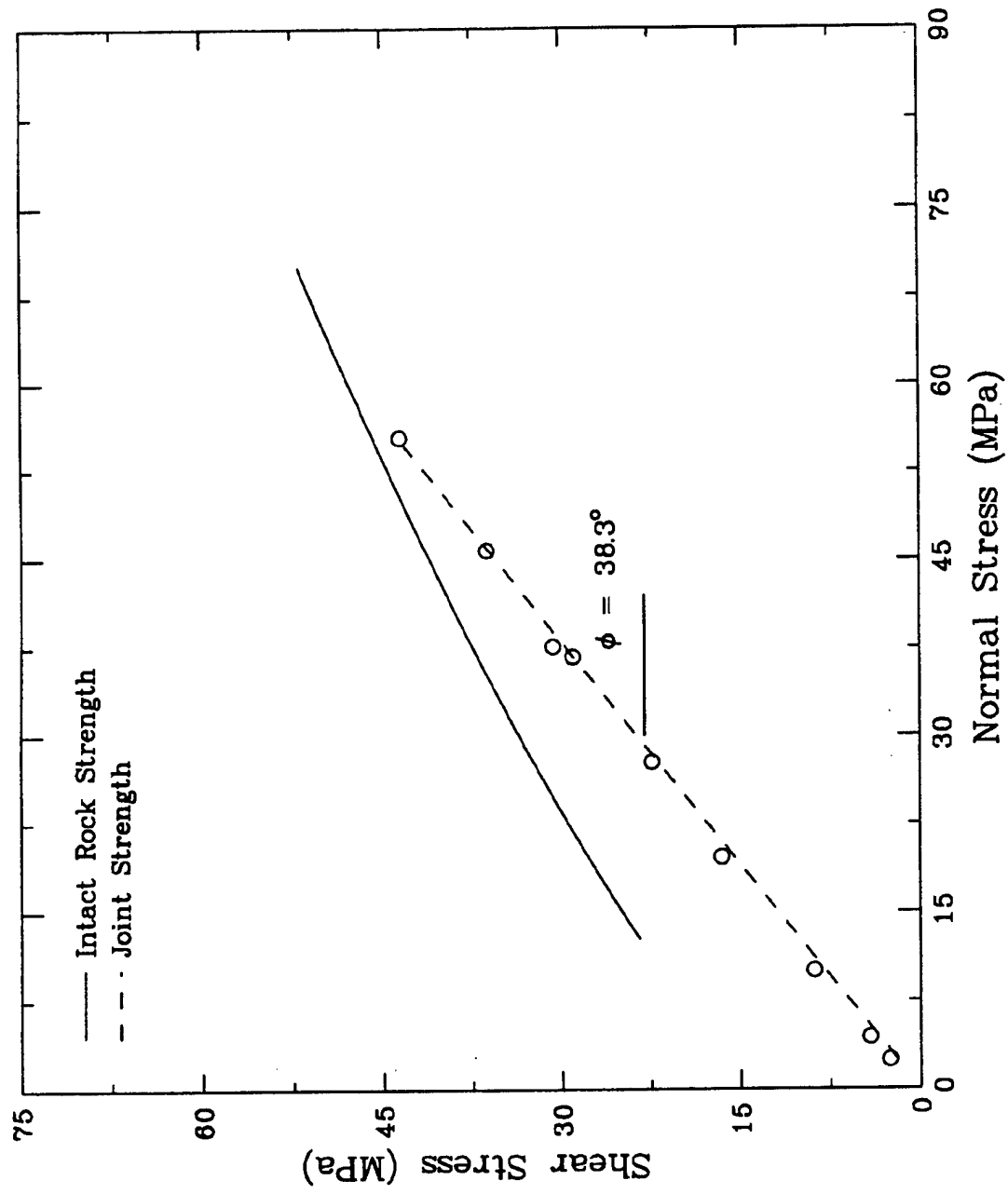


Figure 2-4. Comparison of joint strength with strength of intact limestone.

Because the triaxial compression tests were also intended to provide the reference for intact specimen deformation in subsequent tests of joints, the compression tests were conducted in exactly the same way as the joint tests (that is, with lubricated end caps). This tends to exacerbate a problem that naturally exists with tests in the brittle regime. Namely, as the specimen approaches failure, the strain field tends to become highly nonuniform and shear failure tends to localize in some region of the specimen. As a result of this localization, the strain in the specimen is not well defined, and the deformation measurements begin to lose their meaning. Thus, although deformation measurements were made for the full duration of each test, we have truncated the strains in the vicinity of the peak stress difference to avoid giving the impression that they correctly represent continuum material behavior.

We also performed triaxial extension tests (radial stress exceeding the axial stress, axial stress constant). Figure 2-5 shows the results. The strength points and a straight-line fit are shown in stress-invariant space in Figure 2-6. If we assume a Mohr-Coulomb material and that the strength is independent of the intermediate principal stress (i.e., that the maximum principal stress is a function of only the minimum principal stress), then the two lines shown in Figure 2-6 are equivalent for triaxial compression and triaxial extension, respectively.

2.2.2 Joint Properties.

The shear strength of the joints was determined over the relevant range of normal stresses by a series of triaxial compression tests on 48-mm-diameter cylindrical specimens, each containing a single joint oriented at 30° to the specimen axis. We employed special specimen preparation procedures to ensure that the joint surfaces subjected to laboratory testing were truly representative of the joints in the test article. Limestone bricks that were planed on the same equipment used to construct the test article were cut and ground to the cylindrical specimen shape in such a way that the planed surfaces formed joints in the test specimens. As with the production sawing operation, the laboratory test specimen preparation was performed without using any liquid coolant so that the properties of the finished surfaces would not be changed. The jointed cylindrical specimens were tested in triaxial compression at constant confining pressures ranging from 1 to 35 MPa. Measurements of axial and radial deformations were made through the joint.

Figure 2-7 plots the stress difference versus axial and radial deformation for this set of tests. At confining pressures up to 30 MPa, the specimens failed by sliding of the joints at approximately constant stress. When loaded with 35 MPa confining pressure, the intact portion of the test specimen failed without sliding along the 30° sawn joint. For each test performed at a confining pressure less than 35 MPa, the stress state that caused sliding failure of the joint was measured in terms of axial and radial stress on the cylindrical test specimen. Standard tensor transformations were applied to determine the shear and normal stresses on the plane of the joint. Figure 2-4 shows data points representing the failure stress determined from each test.

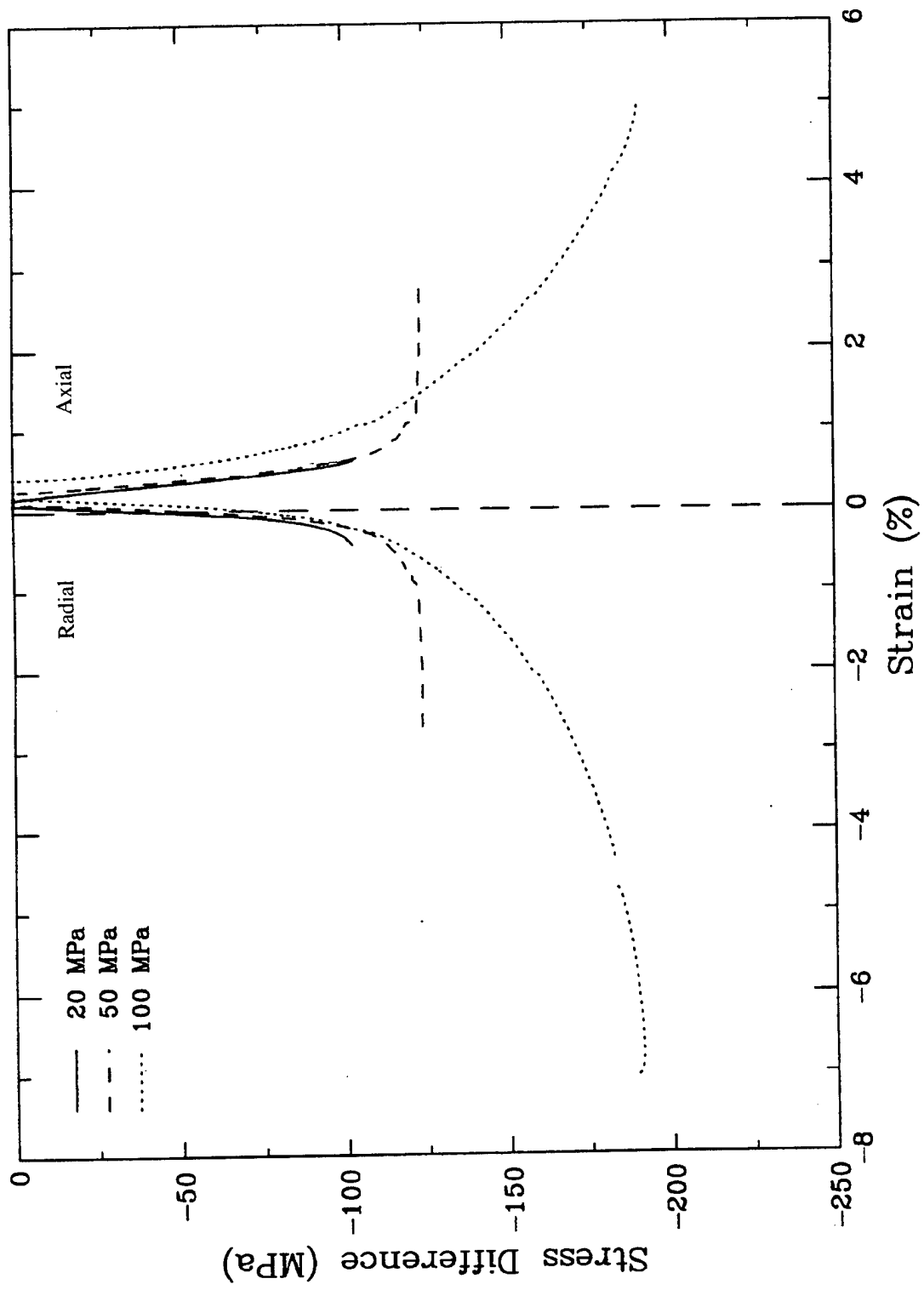


Figure 2-5. Triaxial extension stress-strain relations for Salem limestone.

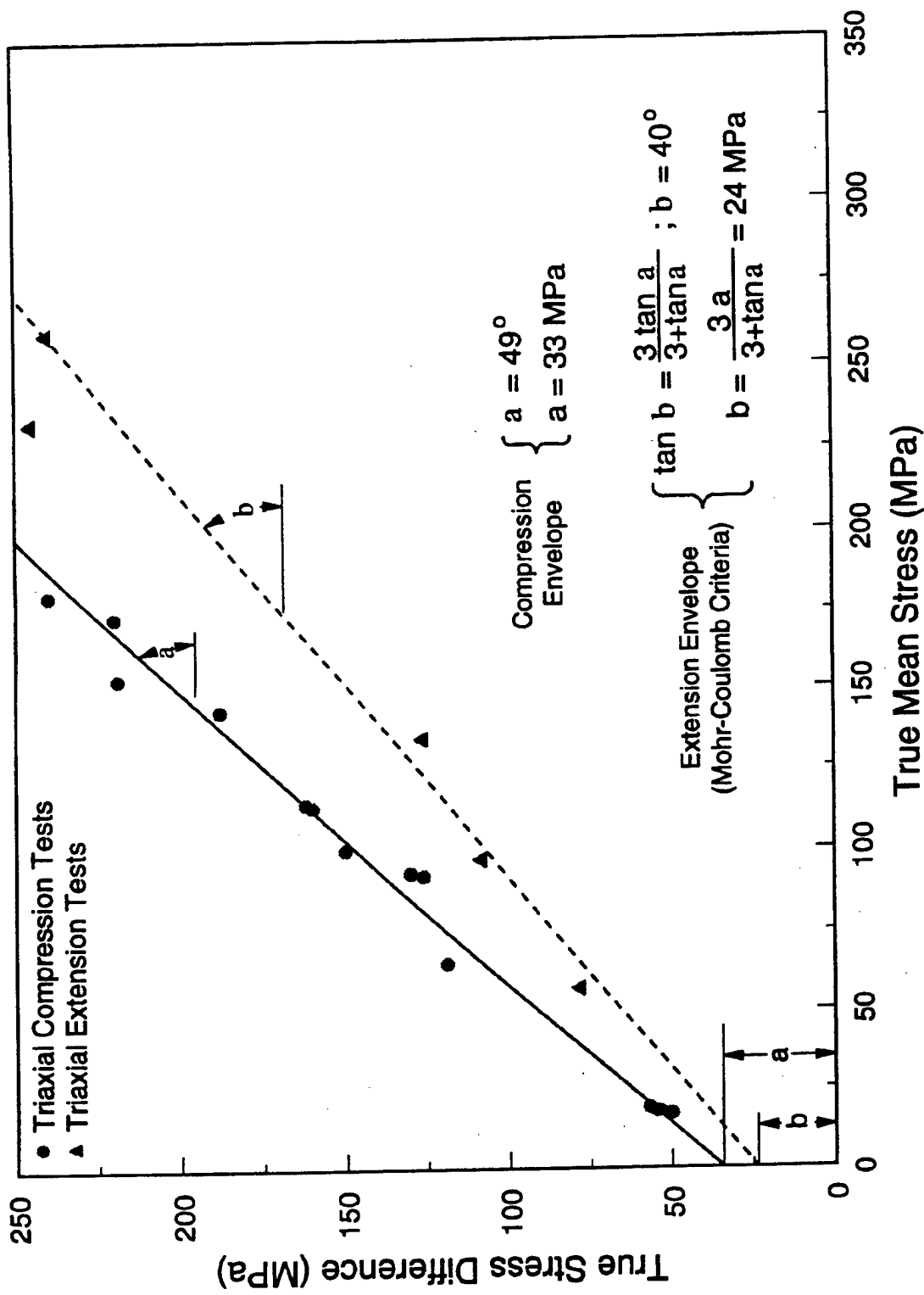


Figure 2-6. Strength envelopes from triaxial extension and triaxial compression tests.

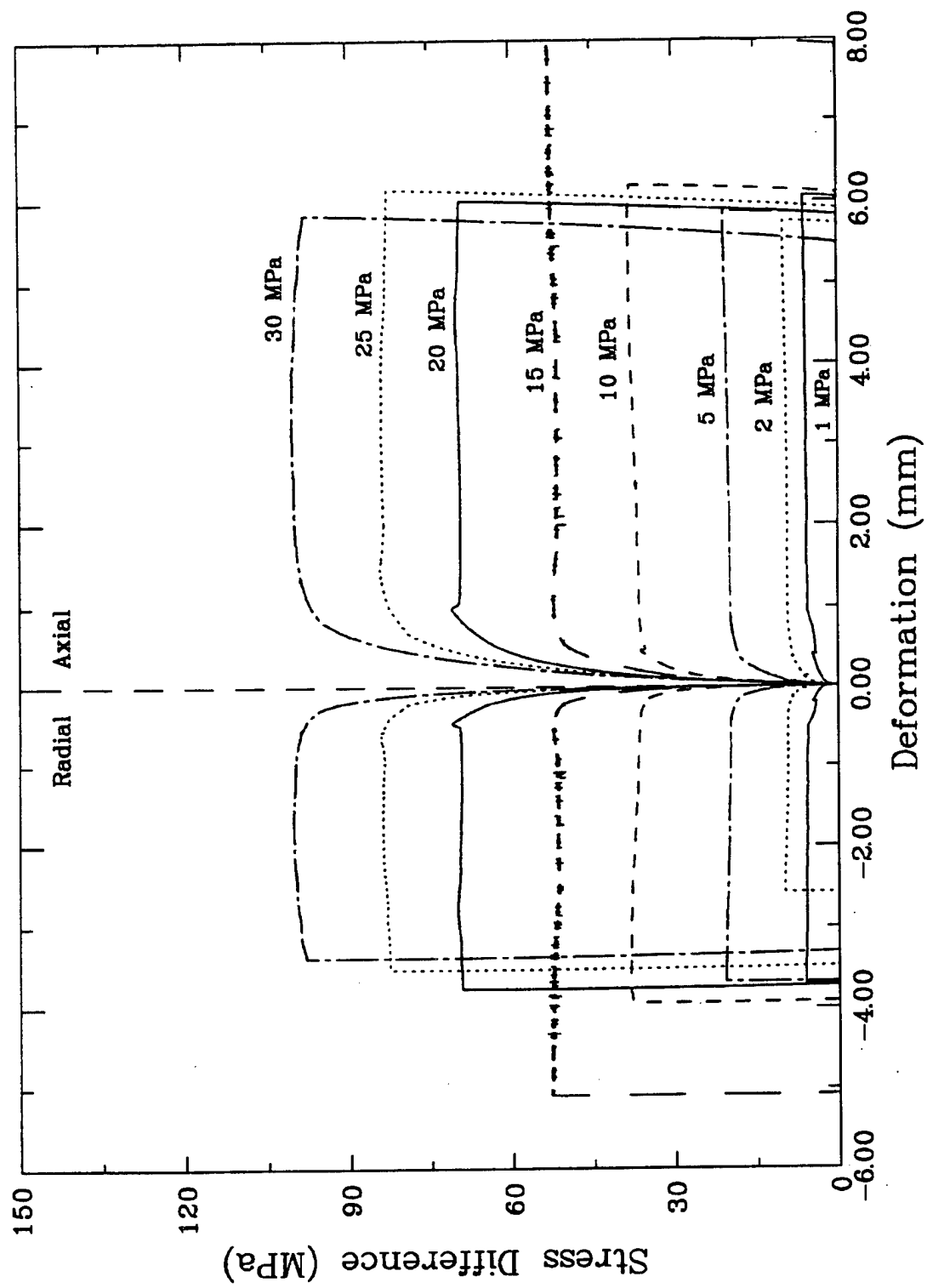


Figure 2-7. Triaxial compression tests on SRI sawn joints in Salem limestone.

The joint strength data are well represented by a straight line (with a 38.3° friction angle) passing through the origin. The normal compressibility of the joint surfaces was determined by unconfined compression tests on 48-mm-diameter cylindrical specimens with a single joint oriented at 90° to the specimen axis. Each specimen was loaded to approximately 75% of its unconfined strength and then unloaded. The axial deformation of the central quarter of the specimen was determined by averaging the outputs of two diametrically opposite displacement transducers mounted to the rock specimen. Based on an independent determination of its elastic modulus, the deformation of the intact rock included in the measurement was subtracted from the measured deformation, leaving only the deformation associated with the joint.

Figure 2-8 presents two, typical, normal compressibility curves. Under normal loading, the joints are fully locked after approximately 0.05 mm displacement.

2.2.3 Jointed Limestone Tests.

We performed three unconfined compression tests on stacks of the bricks that were prepared for the field test article (described below). In all cases, the nominally 51-mm bricks were cut to 300-mm length. Six rows of six bricks were stacked in imbricate sequence, matching the joint pattern of the field test article. External extensometers with a gage length of 200 mm were attached to the ends of the bricks to measure deformation. Measurements from these tests are presented in Figure 2-9 in terms of stress and strain, despite the fact that neither the stress nor the strain states were homogeneous. In each test, the stack failed by vertical splitting of the bricks. In the first test, the jointed stack failed at approximately 26 MPa or about half the strength of the limestone, as determined by the unconfined compression test results presented above. The second specimen failed at about 19 MPa, the third at 18 MPa.

In the process of preparing the specimens for testing, we made measurements to estimate how well the bricks fit together. The quality (dimensional tolerances and surface finish) of the bricks used in the first test was better than the second and the second was better than the third.

We performed two other tests to investigate the strength of an assemblage of limestone bricks. In the first, 51-mm square bricks were cut to 200-mm lengths, then they were ground on all sides with a precision surface grinder, resulting in a finish that was flat within approximately 25 μm over each surface. A four-layer stack of these bricks was tested, and the results are presented in Figure 2-10. The observed strength of 43 MPa is much closer to the intact limestone. To further refine the fit of the bricks, a test was performed on a 50- x 100-mm cylindrical specimen assembled from blocks that were very carefully ground and matched. The estimated flatness of these pieces was 10 μm . The measured strength of 61 MPa exceeds the nominal unconfined strength of 55 MPa presented above. For comparison, we have included, in Figure 2-10, data from another unconfined compression test on an oven-dried intact specimen with a strength of approximately 61 MPa.

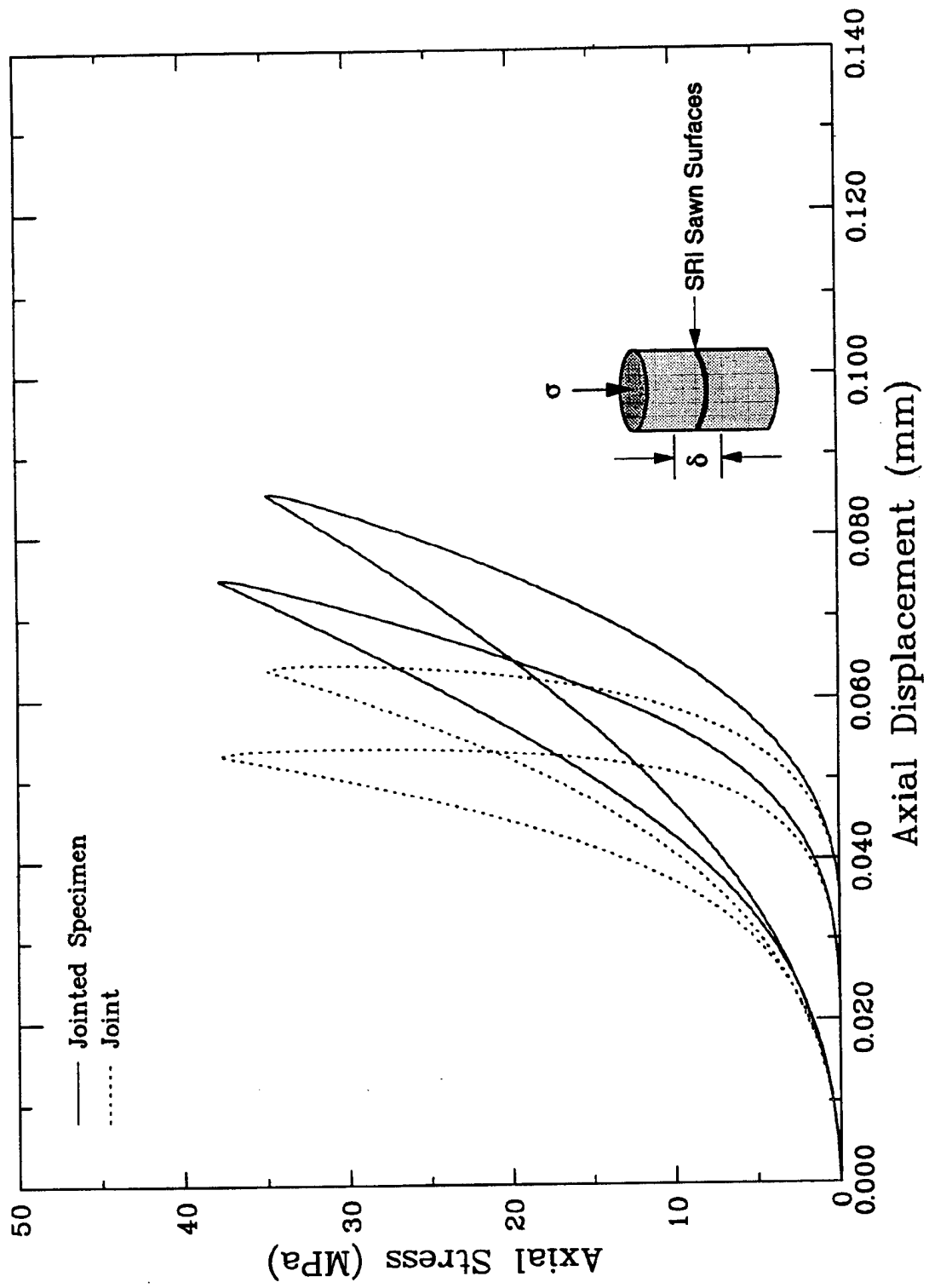


Figure 2-8. Normal compressibility of SRI sawn joint.

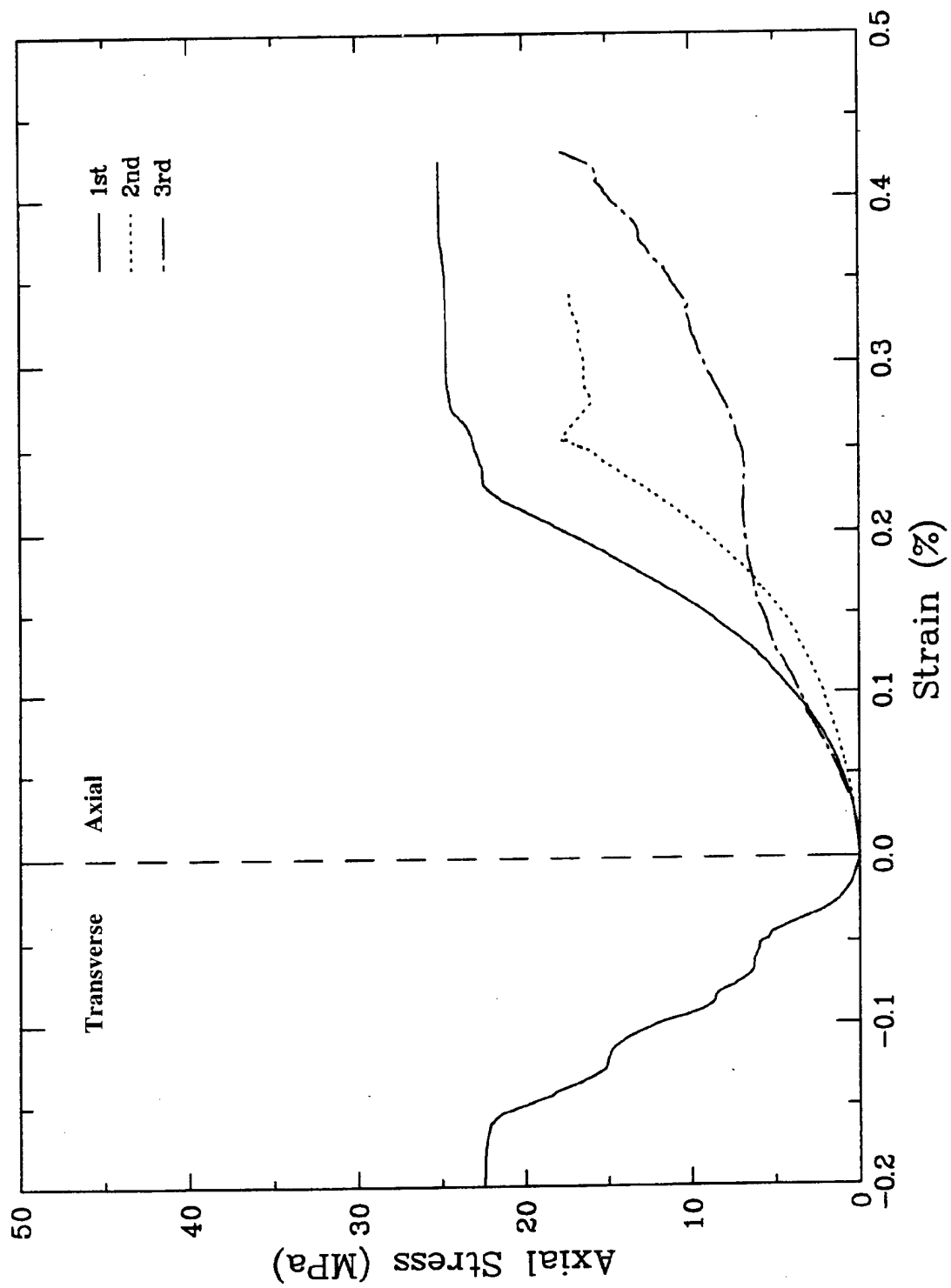


Figure 2-9. Three unconfined compression tests on stacks of bricks.

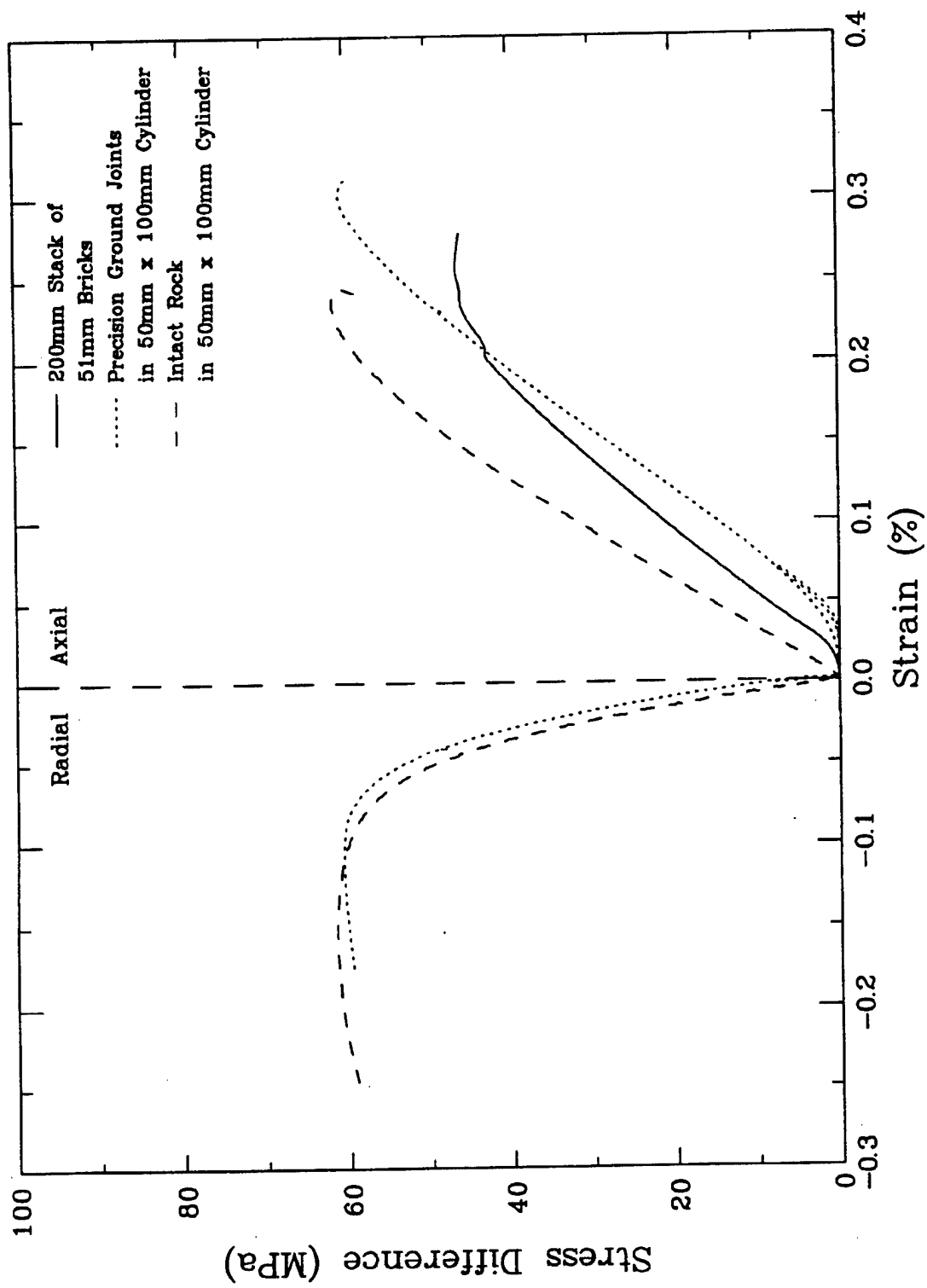


Figure 2-10. Two unconfined compression tests on an assemblage of bricks.

The results of these jointed limestone tests indicate that the apparent strength of an assemblage of bricks is correlated with the goodness of fit of the bricks. We believe that the reduction in apparent strength is simply due to the fact that, if the fit of the blocks is poor, only a fraction of the total cross section is being fully loaded at any time in the test.

2.2.4 Liner Properties.

We performed tensile tests to determine the stress-strain response of the 6061-T0 aluminum liner material. Two tests were performed at an engineering strain rate of 0.001 s^{-1} . Round-bar specimens were cut from the liner such that the specimen axis was tangent to the circumferential direction. The specimens were loaded in a servo-hydraulic testing machine. A 25-mm-long clip gage was used to measure the engineering strain. The machine's load cell was used to measure load.

Figure 2-11 shows the resulting engineering stress-strain curves. The data show good repeatability except for the failure strains, which differ on the order of 20%. The yield strength, ultimate strength, and elongation are all close to the handbook values of 55 MPa, 124 MPa, and 25%, respectively, for 6061-T0 aluminum. The effect of strain rate on these properties is expected to be quite small, based on tests of 1100-0 aluminum (Sensey et al., 1978; Clifton, 1990) and 6061-T6 aluminum (Gilat, 1982).

2.3 TEST ARTICLE CONSTRUCTION.

The dimensions of the limestone bricks as received from the quarry were not sufficiently uniform for this precision experiment, varying in thickness and width by as much as 1 mm from brick to brick and from one end to the other. To prepare the bricks for placement in the test article, we trimmed each side of each brick in a fixtured table saw, using a carbide-tipped blade stiffened by a steel disk. The thickness and width of the finished bricks were 50.86 mm on average (measured at four locations on 24 randomly selected bricks), with a maximum variance of 100 μm and a standard deviation of only 40 μm . The bricks were not trimmed to precise lengths; their nominal lengths were 1.22 m and 0.61 m, with an estimated variance of about 3 mm. The bricks surrounding the opening were machined to have a curved surface matching the radius of the liner. This was accomplished by first trimming the bricks to trapezoidal cross sections, then running the angled surface across a 406-mm-diameter saw blade.

Figure 2-12 shows the finished test article. Its overall dimensions were approximately 2.15 m tall by 2.15 m wide by 2.4 m long. It was constructed of about 4000 bricks in 42 layers. The bricks were placed side by side and end to end so that the vertical joints were staggered from those above and below. Within a layer, end-to-end pairs of 1.22-m-long bricks were alternated with a single, centered, 1.22-m-long brick and two 0.61-m-long bricks at the ends of each layer. Odd-numbered layers were 42-bricks wide; in the

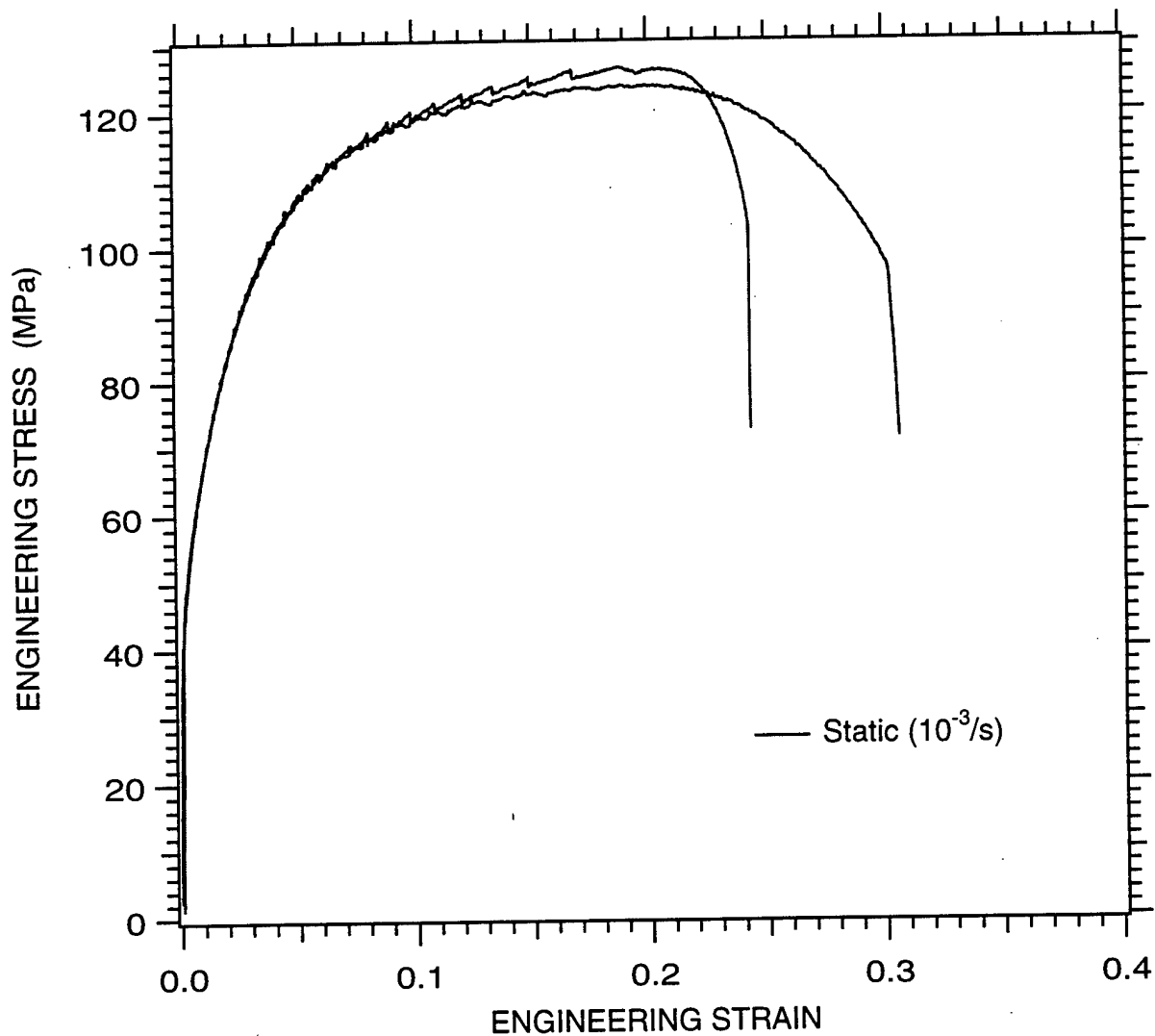


Figure 2-11. Aluminum tensile test results.

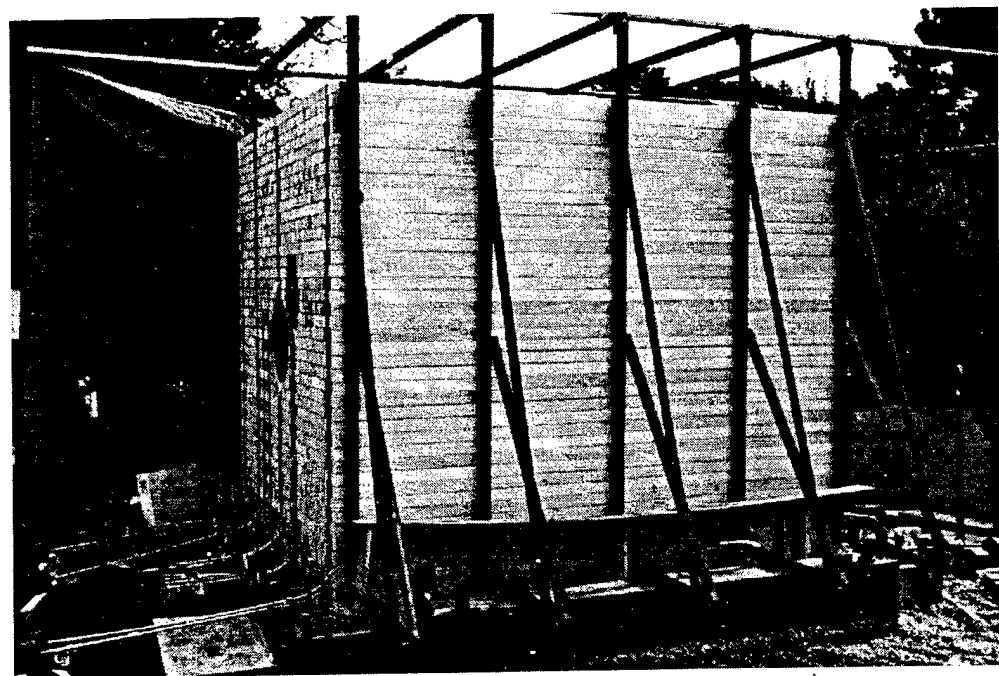
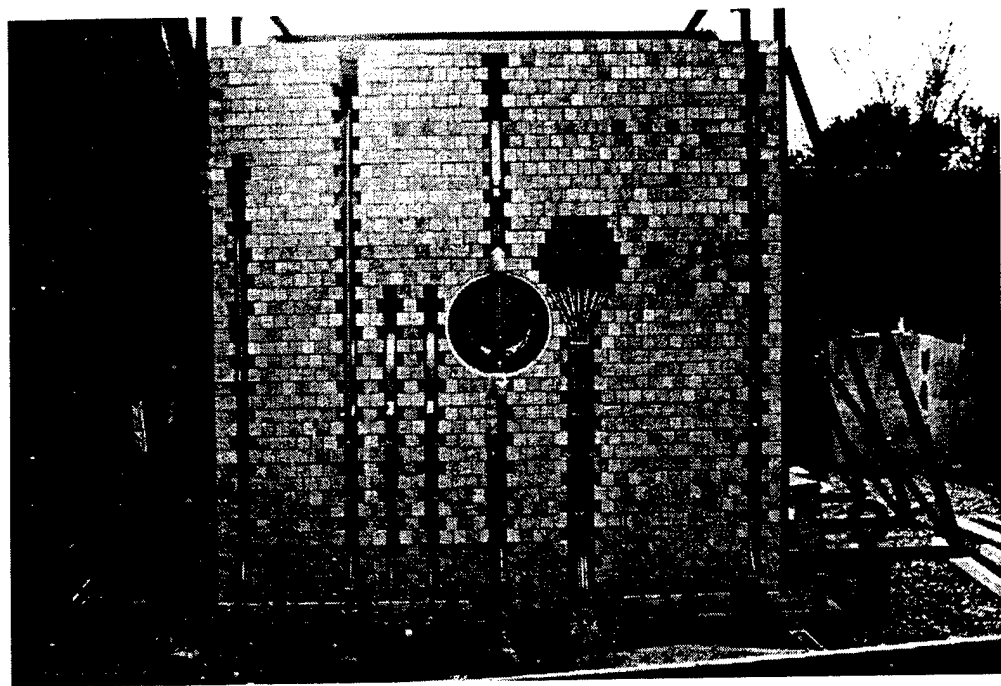


Figure 2-12. MIGHTY NORTH 1 jointed limestone test article.

even-numbered layers the overall nominal width was maintained with 40 standard bricks and two 76-mm-wide bricks at the outer edges. The vertical channels in each end of the test article housed hardened cables for the internal instrumentation.

The 42 layers of bricks were stacked on a cradle comprising a 150-mm-thick, lightly reinforced, concrete slab supported underneath by compacted sand and three, large, steel I-beams running transverse to the length of the bricks. (The cradle was used later to transport the test article to the explosive test site and place it in the testbed.) To produce a flat and level foundation for the stack, we attached the entire first layer of bricks to the bottom of a steel-stiffened, aluminum, tool and jig plate and set it about 20 mm into the concrete slab as the concrete was placed. Vertical steel rails on both sides were used to maintain vertical alignment of the stack; the bricks were placed against the rails on one side and shimmed tight on the other side.

The flatness of the first layer was measured to be within about 0.4 mm, with essentially immeasurable roughness. As the layers were stacked, the small but finite differences in brick thickness resulted in a limited growth of layer roughness in the form of slight ledges at the joints. Consequently, at a given point along its length, each brick rested on only the higher of the two bricks under it with a slight gap over the lower brick. This stack porosity was determined by measuring the average height of the stack up to specific layers (from 6 measurements equally spaced across the layer at each end) and subtracting the known thickness of the bricks (using the average brick dimensions). Quoted in terms of average gap between layers, these measurements indicated a gap of 163 μm , about 0.3% of the thickness of a brick (standard deviation = 32 μm). The average gap varied within the stack, being 112 μm (s.d. = 51 μm) in the bottom quarter (bottom 10 layers), 147 μm (s.d. = 105 μm) in the second quarter, 234 μm (s.d. = 104 μm) in the third quarter (above the opening and containing most of the close-in instrumentation), and 155 μm (s.d. = 53 μm) in the top quarter.

Measurements of surface flatness across the top of the test article, using a straight edge and feeler gages, showed that there was a rounded depression right over the axis of the opening, about 0.4 m wide and up to 2 mm deep. This depression is apparently associated with the installation of the cylindrical liner and the close-in instrumentation. Also, starting about 0.25 m from the sides, there was a gradual roll-off of about 2.5 mm owing to the slight difference in thickness of the 76-mm-wide edge bricks compared with that of the standard 51-mm-wide bricks.

The overall width of the test article was measured at each layer as it was stacked. Again subtracting the known width of the bricks, we determined the average side-to-side gap to be 188 μm , about the same as the average gap between layers. The range of side gaps (by layer) was from 63 to 254 μm , with a slight trend toward larger gaps near the midheight of the stack.

When the stacking was complete, the instrumentation cable channels were filled with mortar, the outside surface of the test article was painted with a sealant, and the entire test article was encased in a 150-mm-thick layer of lightly reinforced concrete. This assembly was supported and braced with steel beams and channels and the 50-ton unit was shipped to the test site via crane and truck. Placement of the test article in the testbed involved several steps. First, as shown in Figure 2-13(a), a concrete pedestal with three channels running across it was built on top of the lower concrete layer of the testbed. Next, leveling jacks were set at the end of each channel and grout was placed over the top surface of the pedestal. The test article was then lowered into the testbed so that the steel support beams underneath it fit in the channels and rested on the jacks, while the grout was compressed and extruded between the pedestal and the lower surface of the test articles, as shown in Figure 2-13(b). When the grout was cured, the jacks were lowered and the steel beams were removed. Finally, the channels under the test article were filled with concrete.

2.4 INSTRUMENTATION.

2.4.1 Instrumentation Plan.

As shown in Figures 2-14 and 2-15, a total of 46 transducers were installed in the test article to measure both the velocity at the boundary and the internal response. All the transducers were located as near as practical to the vertical plane normal to the axis of the cylindrical opening and at the midlength of the opening. Gage locations are referenced to the Blue and Red ends of the test article and to the North and South sides of the test article. All the instruments were installed during the stacking of the bricks. The fabrication and testing schedules resulted in some instruments being installed approximately 1 year prior to the test.

Twenty-two velocity gages defined a nearly square boundary slightly inboard of the actual limestone/concrete interface. Both vertical and horizontal velocities were measured, as indicated by the arrows on the velocity gage symbols in the figure. Vertical velocity was measured at five places along the top boundary, at four places along each side (with redundant measurements at the depth of the opening axis), and at three places along the bottom. Horizontal velocity was measured at four places along each side. These measurements, presented below, show that this gage array was adequate to establish the precision of the velocity measurements, to demonstrate the degree of symmetry of the environment, and to define a continuous velocity boundary condition.

The instrument array for measuring the test article response comprised four relative-displacement gages in the lined opening, eight stress gages in the jointed limestone, and twelve joint slip gages. Two of the

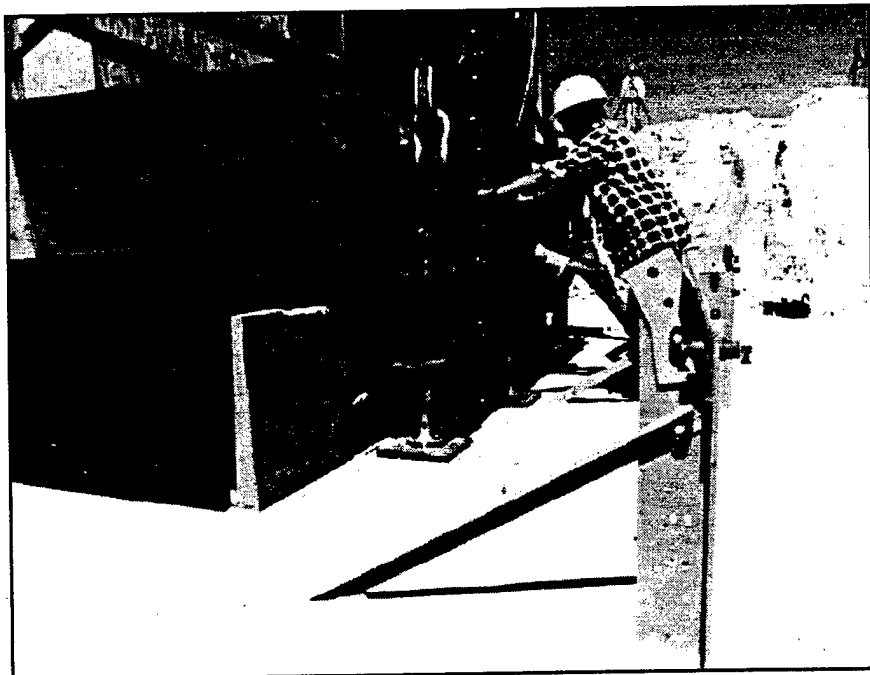
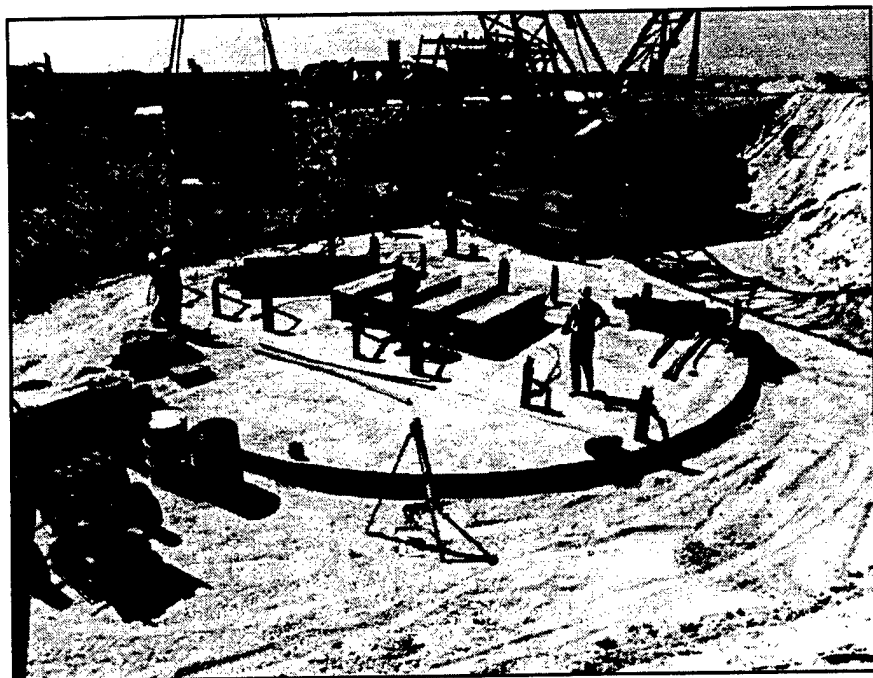


Figure 2-13. Placement of MIGHTY NORTH 1 test article in test bed.

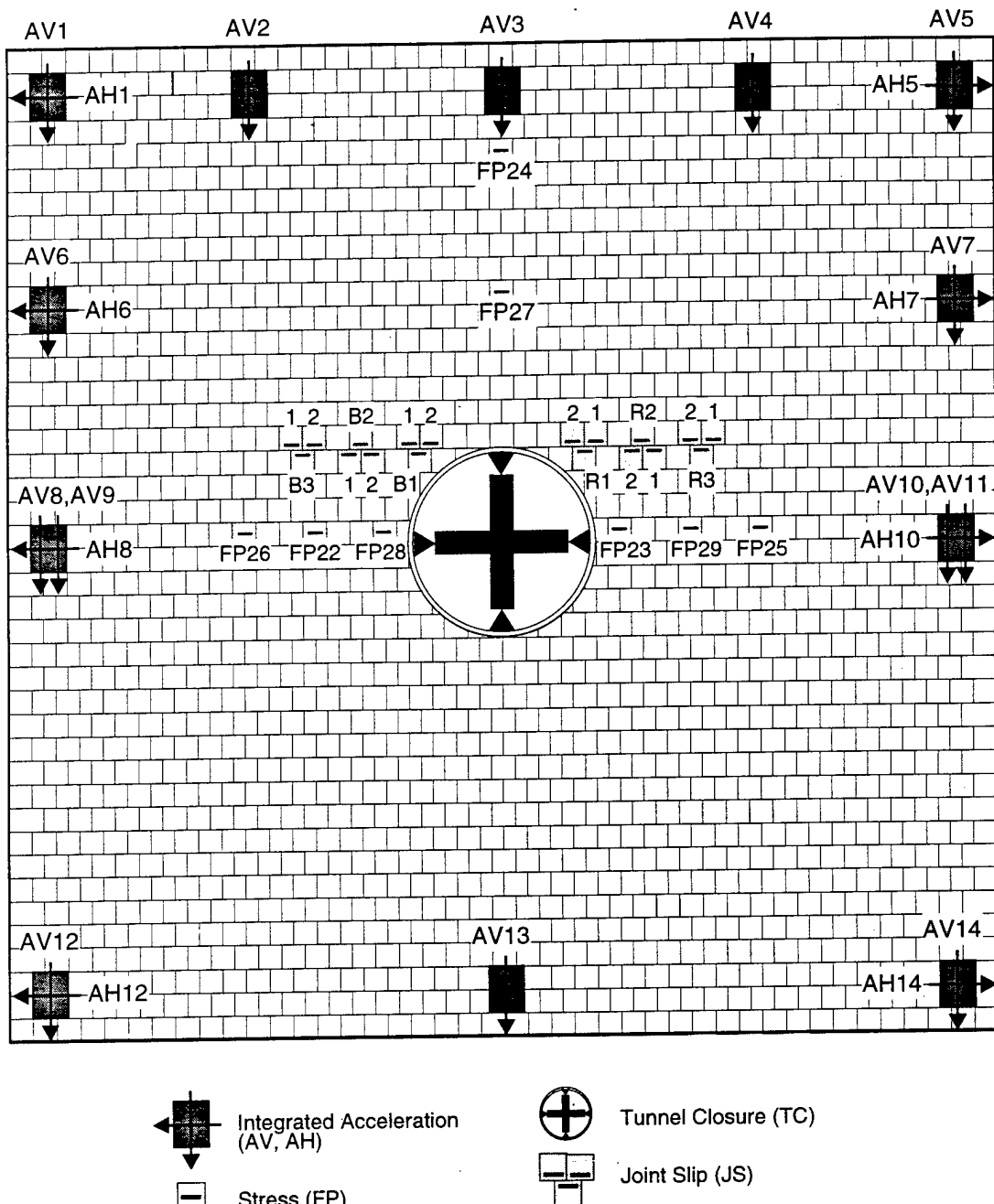


Figure 2-14. Elevation view of the gage array in the limestone.

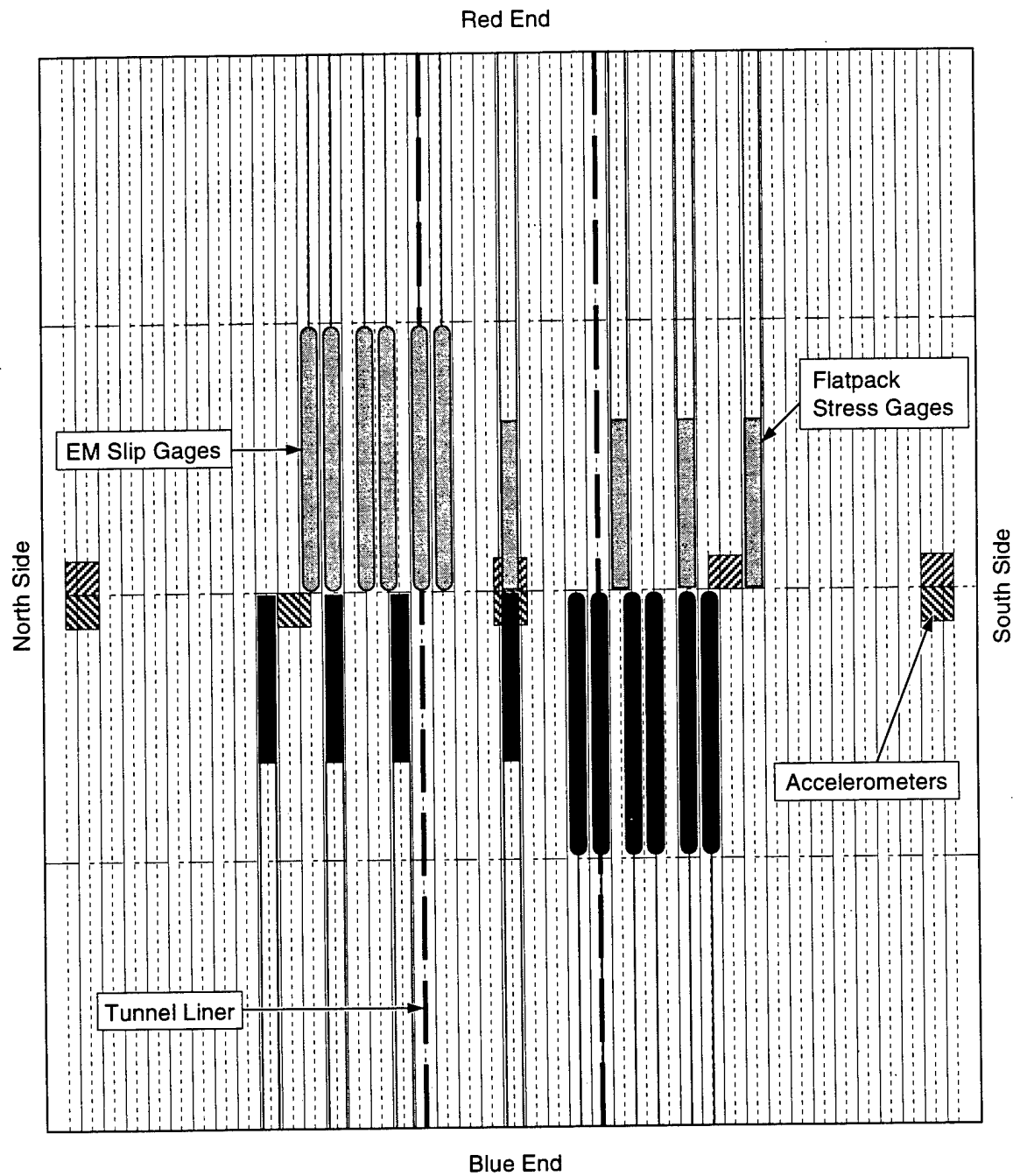


Figure 2-15. Plan view of the gage array in the limestone.

displacement gages were oriented to measure crown-invert diameter change (vertical closure), and two were oriented to measure springline diameter change (horizontal closure).

All the stress gages measured vertical stress. Two stress gages were located above the opening in the plane of symmetry. Six stress gages were placed symmetrically in a horizontal plane lying just above the axis of the opening, outboard of the springlines of the opening. The outermost pair of these stress gages was intended to provide approximately the unperturbed free-field vertical stress at the depth of the opening. The other stress gages were intended to measure the effect of the opening on the stress field.

Joint slip gages were concentrated in the horizontal plane tangent to the crown of the opening. The selection of this location was guided by the numerical analyses performed in the UTP benchmark activity (Simons, 1991). These gages measured horizontal slip between bricks of adjacent layers. The joint slip measurements were spaced symmetrically on either side of the opening.

2.4.2 Accelerometers.

The motions at the perimeter of the test article were measured using piezoresistive accelerometers mounted in shock-isolated canisters to limit the peak acceleration signals. Shock isolation was used to prevent overrange of the measurement system in case the predicted acceleration levels were exceeded. Figure 2-16 is a cross section through an accelerometer package. The nominally 102-mm-tall by 102-mm-long by 76-mm-wide aluminum canisters were designed to match the density of the limestone bricks and were individually machined to the height of the adjacent bricks ($\pm 25 \mu\text{m}$) and for a friction fit in their respective cavities in the test article.

The vertical and horizontal sensors were installed into a friction-coupled shock-isolator consisting of a piston in a split clamping bore. The sensors were mounted on the piston and the bore was rigidly coupled to the canister. The motion that can be transmitted to the piston was limited by the friction between the bore and piston. This friction force was the product of the normal force across the boundary and the coefficient of friction at the surface. The clipping acceleration level was adjusted by the torque applied to the clamp screws in the split bore. The pistons and bores were calibrated using a hydraulic press fitted with a load cell. They were set to clip at an acceleration of nominally 50,000 g. The shock isolation was activated only when the acceleration reached or surpassed the clipping level. At acceleration levels below this threshold, the piston followed the motion of the bore and canister. Thus, the shock isolation system, if activated, limited the slope of the rise to peak of vertical velocity, but the horizontal velocity was unaffected.

The signals coming from the accelerometers were conditioned by a hardened differential in, differential out (DIDO) electronics package located within the concrete testbed near the base of the jointed limestone test

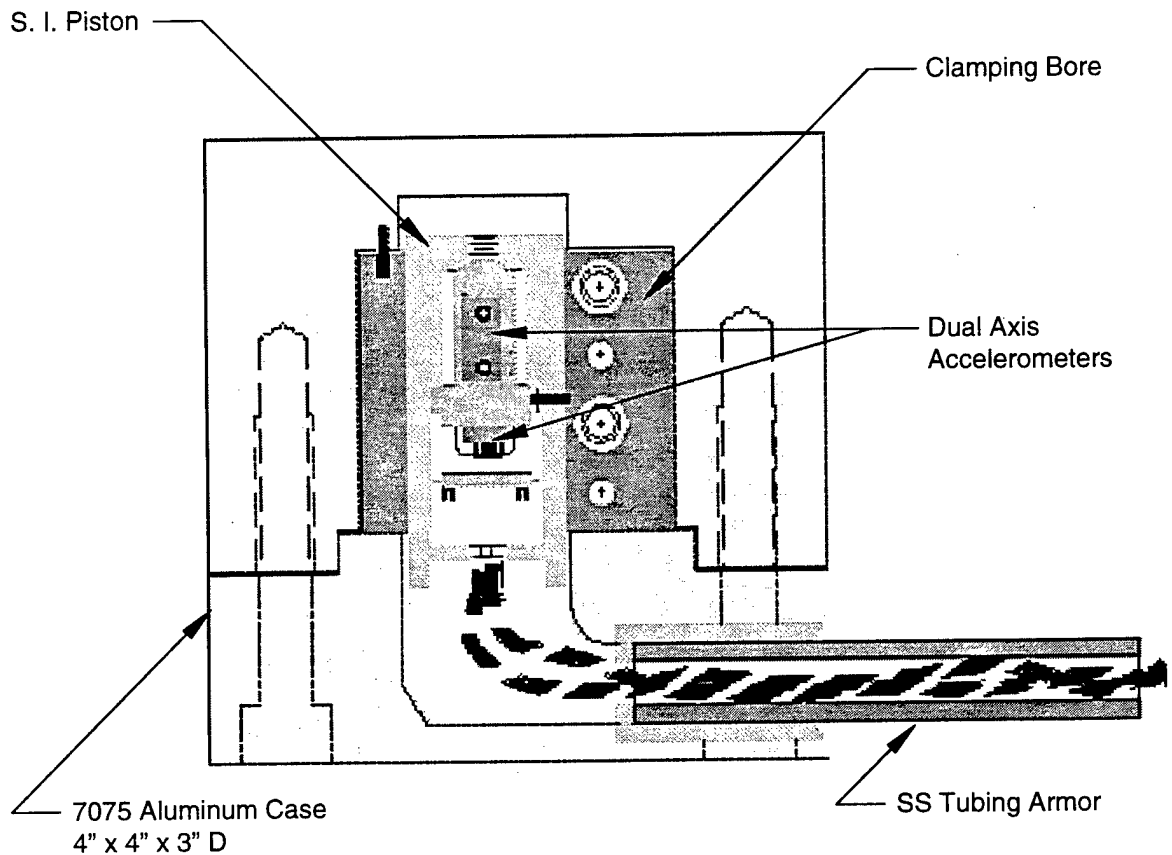


Figure 2-16. Shock isolated accelerometer.

article. This package performs several functions: it boosts the signal level to maximize the signal-to-noise ratio, it matches and drives long twinax transmission lines, and it injects a calibration pulse with a unique, embedded, ID code. An important feature of the differential architecture is that only the normal mode signal is amplified; common mode signals (such as noise) are passed with unity gain. Careful design and construction of the overall package protected the electronics from damage and upset due to high level shock.

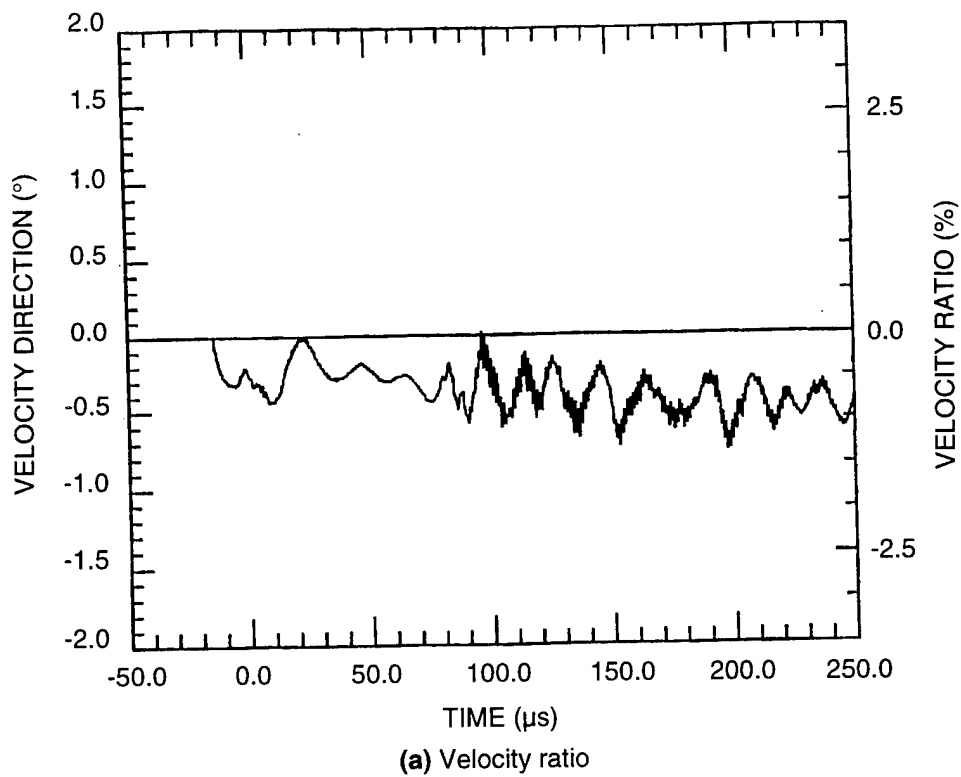
A differential integrator (INTAC) was located at the end of the line just ahead of the recorders. The velocity derived from acceleration is of primary interest (the first integral of the signal). Generally, accelerometer data are numerically integrated after recording, but this demands that the recording system have an enormous dynamic range to cover the huge variation in amplitude of the acceleration signal as well as the large uncertainties typically associated with the initial peak (i.e., the rise of the velocity waveform). The INTAC, however, removes this dynamic range requirement from the recording system entirely. The INTAC was carefully designed to have an extremely low noise floor and eliminate baseline offsets yet be dc responding.

Calibration of representative accelerometers was accomplished using a large scale Hopkinson bar (Brown and Drago, 1977; Petersen and Groethe, 1988; Ueda and Umeda, 1993) with a photo-optic displacement gage as a reference. These tests also established cross-axis sensitivity and zero offset susceptibility, as shown in Figure 2-17.

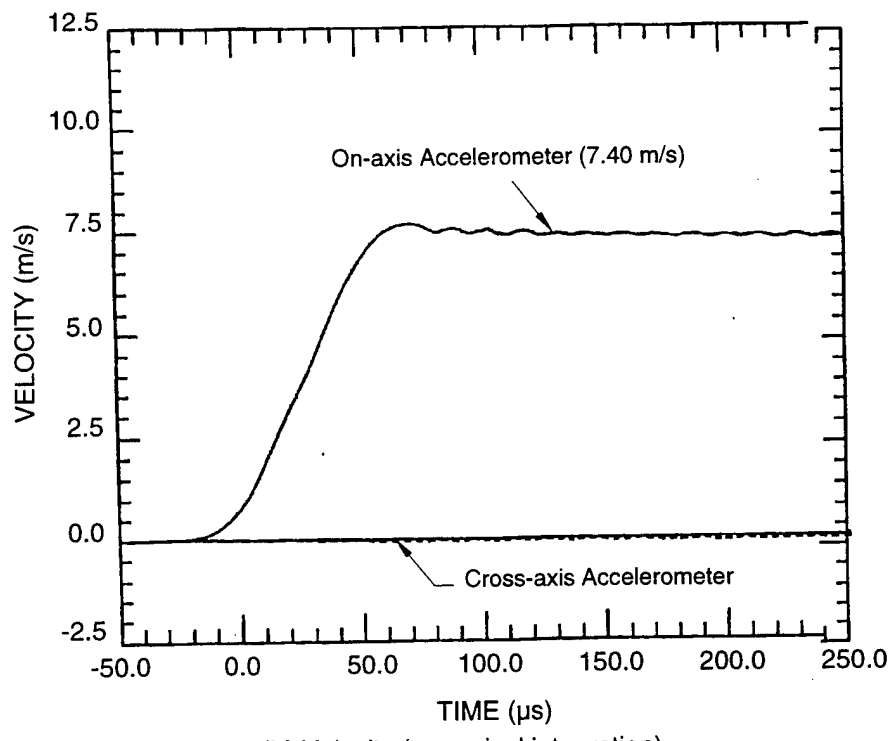
2.4.3 Closure Gages.

The closure gage design, shown in Figure 2-18(a), comprises a pair telescoping tubes with two optical transceivers mounted in the outer tube and precisely spaced circumferential grooves machined into the outer surface of the inner tube. The optical transceivers consist of a light-emitting diode (LED) and a photo diode that senses the LED light reflected from the grooved surface of the inner tube. As the two tubes slide past one another, the signal from the photo diode rises and falls according to the position of the photo diode relative to the crests and troughs of the grooves. The transceiver pair were spaced 1/4-groove apart to provide two signals that are 90° out of phase, thereby allowing the direction of motion (and motion reversals) to be detected unambiguously. Peaks and valleys in the signals were counted by computer and the known spacing of the grooves (1.27 mm) provided the calibration.

The closure gages were installed in the liner before the liner was installed in the test article. Each end of a gage had a spherical swivel joint attached to a small aluminum block that was anchored to the liner wall with screws from the outside, countersunk flush.

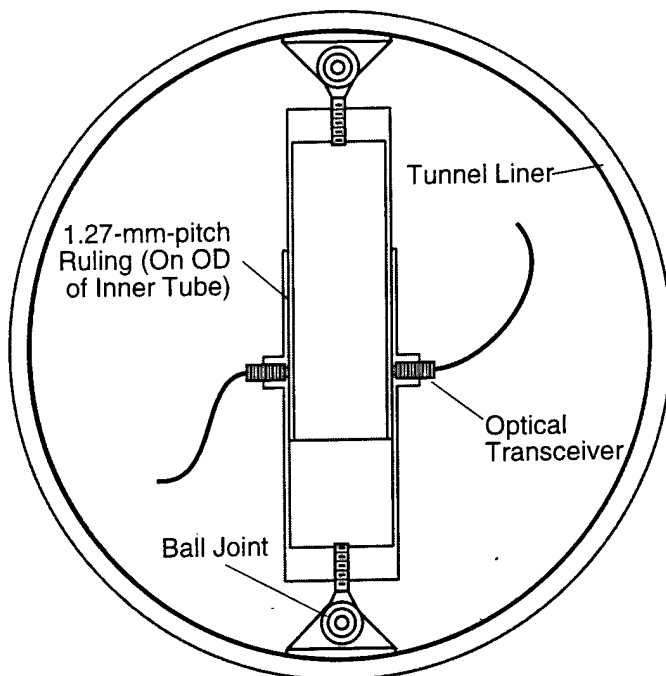


(a) Velocity ratio

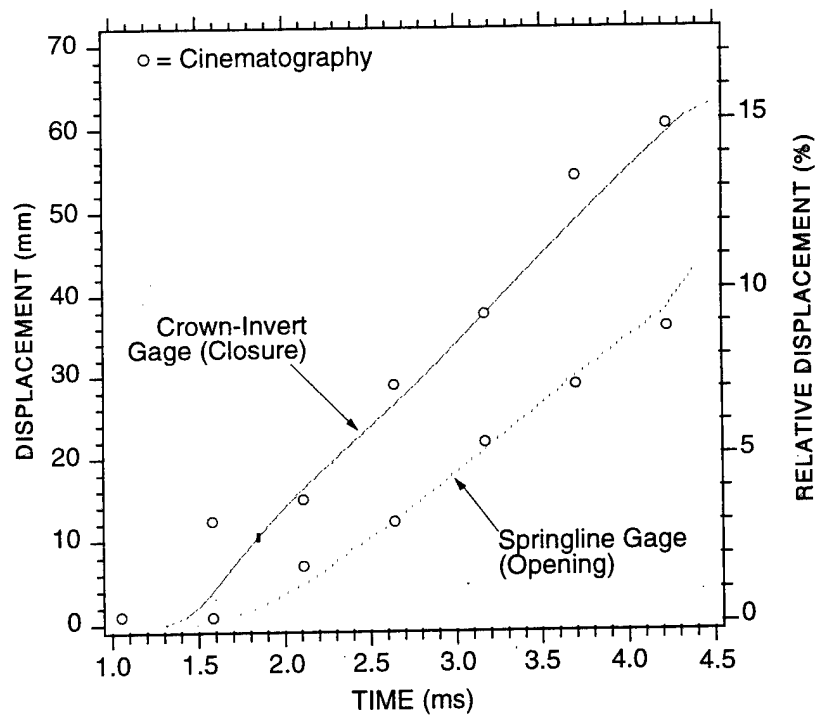


(b) Velocity (numerical integration)

Figure 2-17. Calibration tests to establish cross-axis sensitivity and zero offset susceptibility.



(a) Gage locations



(b) Dropweight test results

Figure 2-18. Tunnel closure gages.

Although the closure gages are inherently self-calibrated via the known spacing of the grooves in the inner tube, the performance of the gages was demonstrated and compared to high-speed photographic monitoring of the closure. In this demonstration, a 170-kg mass was dropped from a height of 26 m onto a short section of liner containing one vertically oriented and one horizontally oriented closure gage. Figure 2-18(b) shows that both closure gages survived and their records agreed with the motion monitored with the high-speed camera.

2.4.4 Stress Gages.

Limestone stresses were measured with flatpack stress gages, which comprise very thin stress-sensing elements sandwiched between layers of insulation inside a protective case. The width of the gage package is about 12 times greater than its thickness. This geometry minimizes the perturbation the gage makes to the stress field it is trying to measure. As shown in Figure 2-19, each flatpack was installed in a limestone brick by machining a channel in the bottom half of the brick and bonding the gage and the brick halves together with epoxy.

Figure 2-19 shows the interior design of the flatpacks. The ytterbium and constantan elements are piezoresistive materials (i.e., their resistances change under applied stress). These elements are insulated with Teflon® film, and the stainless steel case is welded together at its edges. In the flat foil geometry, the ytterbium element is highly sensitive to the applied normal stress (approximately 4% change in resistance per 100 MPa) but it can be perturbed by longitudinal strain. Constantan is commonly used for strain gages because of its relatively high resistivity and its low sensitivity to normal stress. The stress-sensing area of the flatpack is that of the ytterbium elements; the constantan element was used to monitor the longitudinal strain. Six ytterbium elements, each having dimensions 13 mm by 25 mm, were spaced about 75 mm apart so that the stress gage averaged the limestone stress over about a 400-mm length of the brick. The sensing area of the gages extended from near the tip of the case, which was placed at the vertical midplane of the test article, toward either the red or blue end of the test article.

The method for interpreting the resistance histories combines the piezoresistance relations and the constitutive relations for ytterbium and constantan to determine the normal stress and longitudinal strain histories that simultaneously satisfy these relations. Approximate properties of the element materials are available from other work (Chen et al., 1984), but laboratory calibration tests of the flatpacks are used to determine the best mechanical and piezoresistance coefficients for each gage. A computer program named PIEZOR (Gran and Seaman, 1997) solves the simultaneous set of nonlinear equations.

The flatpack stress gages were calibrated statically in a pressurized oil bath to 200 MPa. The average resistance change of the six ytterbium elements, the constantan element, the temperature of the oil, and the

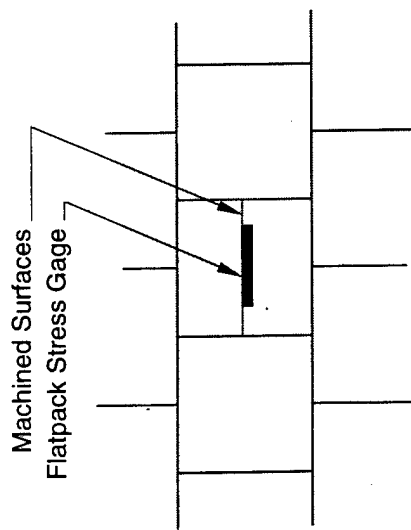
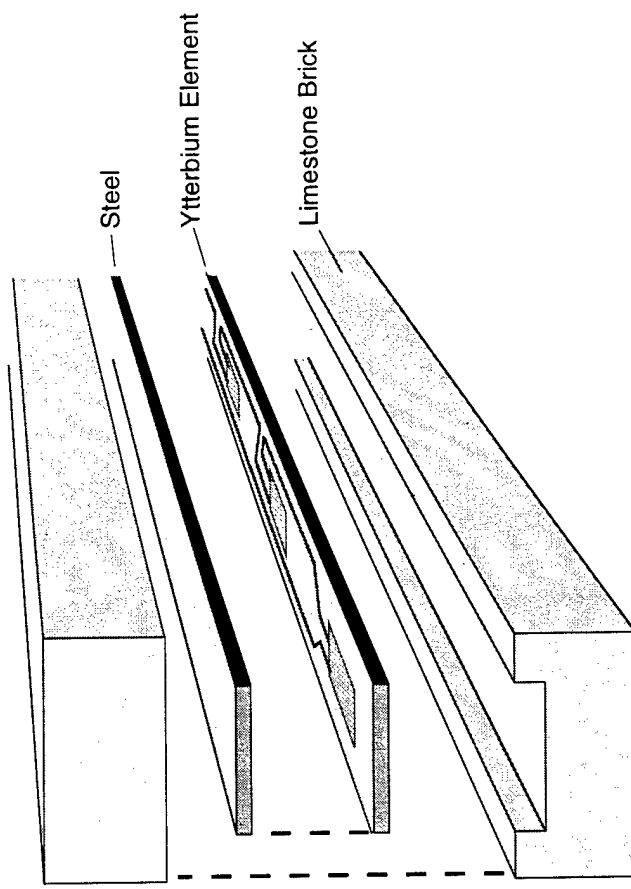


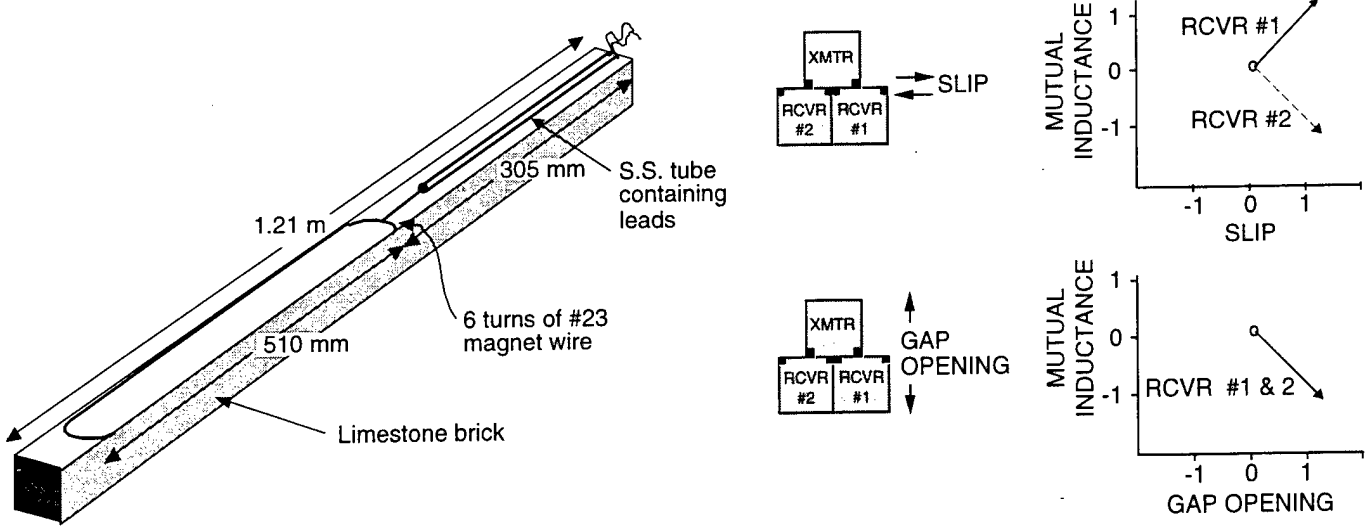
Figure 2-19. Installation of flatpack stress gage in a 51- x 51-mm limestone brick.

pressure were recorded. The strains were, in all cases, small enough to be ignored (demonstrating uniaxial strain conditions) and the ytterbium element resistances were compensated for the effect of temperature (Lilley and Stephens, 1971). Up to 100 MPa (the peak recorded in the MIGHTY NORTH 1 experiment), the calibrations of the eight flatpacks plus two spares exhibited a standard deviation of only 3% of peak. In addition, the average property was nearly linear and agreed almost identically with the published properties of ytterbium (Gran and Seaman, 1997; Lilley and Stephens, 1971; Chen et al., 1984). Thus, the parameters of the published properties were used in the data reduction to convert resistance change to stress and to compensate for longitudinal strain.

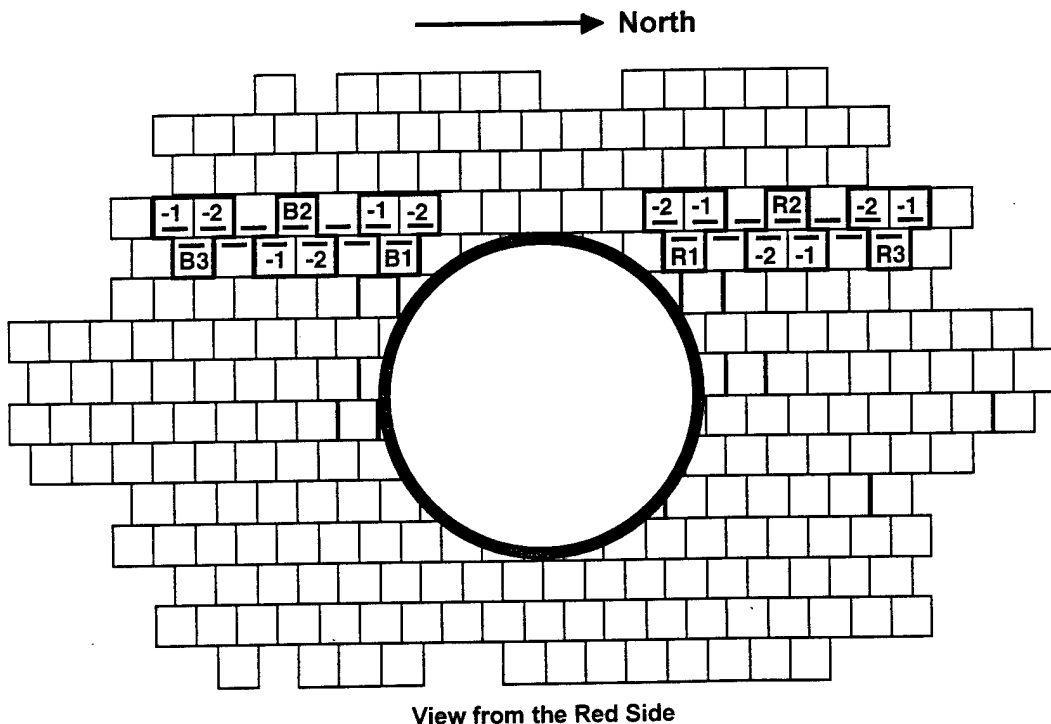
2.4.5 Joint Slip Gages.

Horizontal slip between adjacent bricks was measured through the change in mutual inductance between two electromagnetic coils embedded in opposing brick faces. As shown in Figure 2-20, the coils were epoxied into grooves milled into 1.2-m limestone bricks, in a manner minimizing the alteration of the limestone joint surfaces. The coils were 510 mm long and centered 305 mm from the end of the brick, which was placed at the midplane of the test article, as shown in Figure 2-15. The individual coils were fielded in groups of three as shown in Figure 2-20. The transmitter coil was pulsed with a high current, square, wave train at about 100 kHz. The signal from each receiver coil was phase decoded and filtered to produce a voltage proportional to the mutual inductance between the coil and the transmitter. The mutual inductance changes as the bricks slide relative to each other. However, the mutual inductance will also change if a gap opens between bricks. To discriminate between slip and gap opening two receivers were used with one transmitter. For slip, the coupling between the transmitter and receiver #1 will increase, while the coupling between the transmitter and receiver #2 will decrease; whereas for gap opening, the coupling will decrease uniformly for both receiver #1 and #2.

We calibrated the joint slip gages in the laboratory by measuring the mutual inductance as a function of coil offset, and the effect of the aluminum liner was quantified.



(a) Overall view



(b) Slip gage locations

Figure 2-20. Electromagnetic slip gage brick.

SECTION 3

RESULTS

3.1 GENERAL.

The data return from the active gages in the test article was excellent, with the exception of the closure gages. All 22 velocity measurements and all 8 stress measurements were successful. All the slip gages functioned, but some were interrupted fairly early because of limestone fracture and some had such small slips that the signal was no larger than the background noise. The closure gages were inoperable at the time of the test; the optical transceivers failed sometime after the placement of the concrete in the testbed.

The symmetry of the environment and test article response was also excellent. For example, the side-to-side asymmetry (North-to-South in Figures 2-14 and 2-15) exhibited by the measurements of peak vertical velocity was less than 5%. Peak stresses varied side-to-side by 12% on average. The asymmetry is statistically significant in the sense that the peak velocities and stresses on one side were uniformly greater than those on the other side by an amount within the capability of the measurement system to detect. However, the asymmetry was not significant to the objectives of the experiment. Thus, the concept of a symmetric field is justified.

3.2 VELOCITIES.

We obtained extremely high quality data from the accelerometers. All gages survived the test except one, 4V, which failed but only after capturing the important features of the waveform. One gage, 12V, suffered from a bad connector at a lightning protection junction-box. However, good quality data were recovered from this gage through careful scaling and filtering.

Figure 3-1 is a composite plot illustrating the excellent precision and symmetry obtained from the four independent measurements of vertical velocity at the tunnel depth. The positive phase duration at the tunnel depth was about 2 ms, which was the design objective (Goodfellow and Rinehart, 1995). Figure 3-2 shows plots of the vertical velocities down the two sides of the test article. Figure 3-3 shows plots of the horizontal motion along the sides of the test article. Zero time in these plots (and all the history plots that follow) is the initiation time of the explosive charge. The arrival of the stress wave at the top of the test article was 2.13 ms.

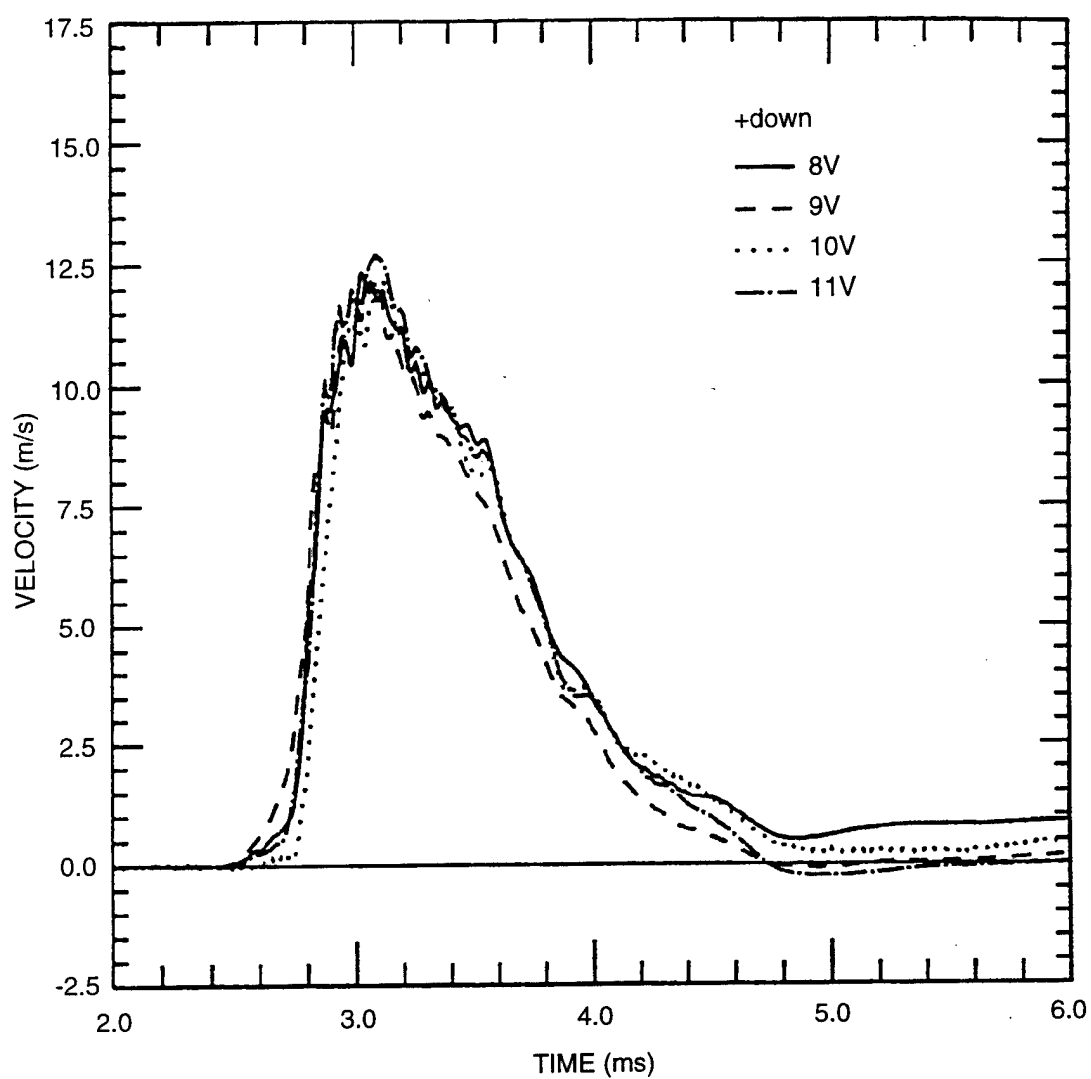
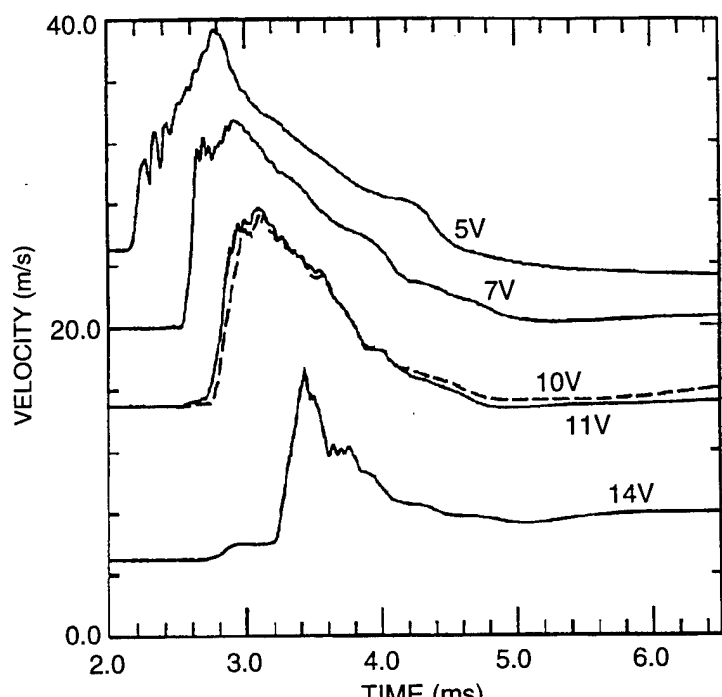
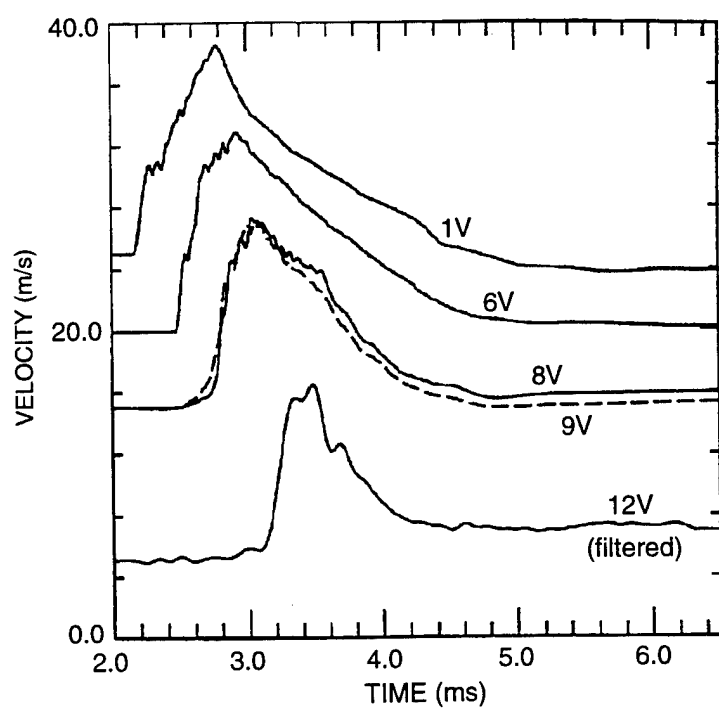


Figure 3-1. Four vertical velocities measured at the tunnel depth.

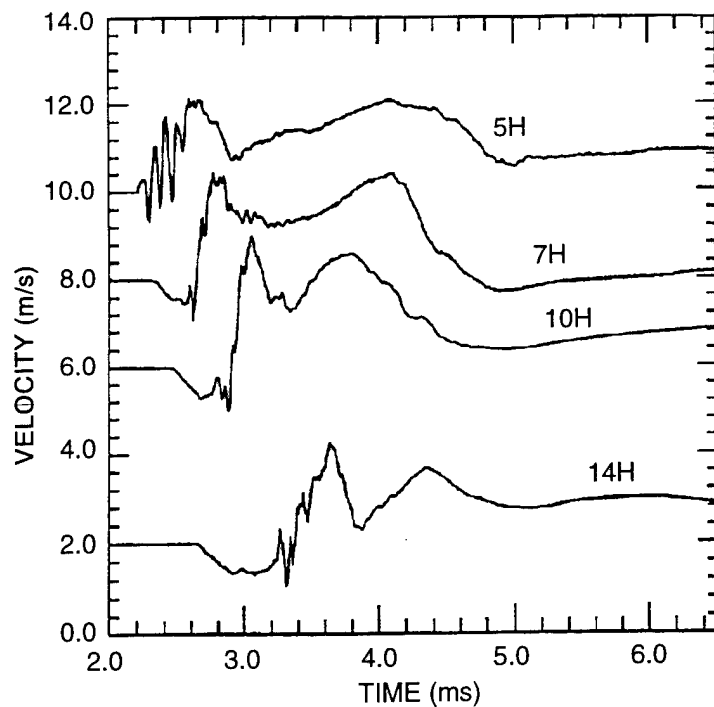


(a) North side

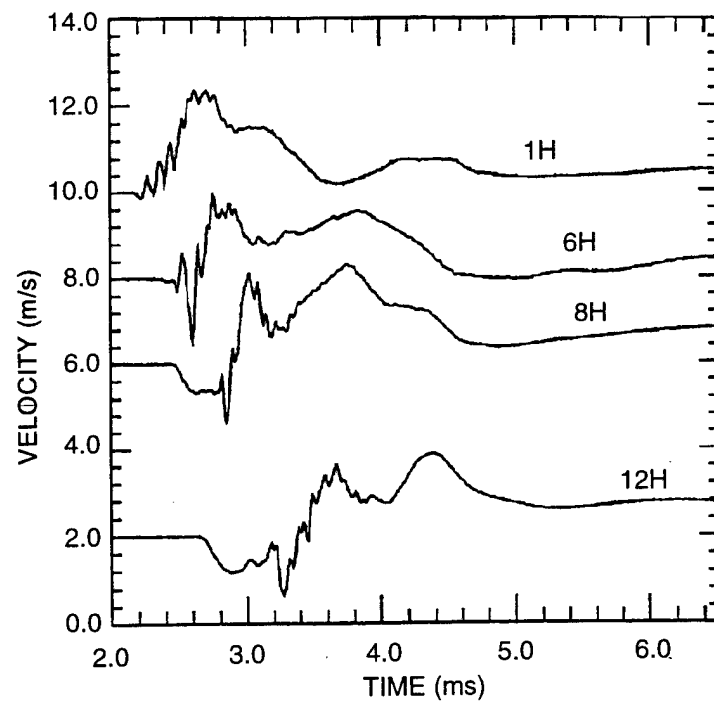


(b) South side

Figure 3-2. Composite of test article vertical velocities.



(a) North side



(b) South side

Figure 3-3. Composite of test article horizontal velocities.

The vertical velocities show the evolution of a precursor and the steepening of the front of the main wave. The velocity of the main wave is much lower than the P-wave speed in intact limestone and is apparently so low because of the time needed to close the gaps at the joints. In fact, the additional time needed to propagate through the test article is consistent with the nominal peak particle velocity and the total amount of gap. The precursor may be an elastic precursor transmitted through the brick contact points, but it was more likely produced by the stress wave in the concrete testbed, which outran the stress wave in the limestone. The initial motion in the horizontal direction was inward, showing clearly that the stress wave in the concrete testbed had outrun the stress wave in the jointed limestone test article by about 0.5 ms at the bottom of the test article.

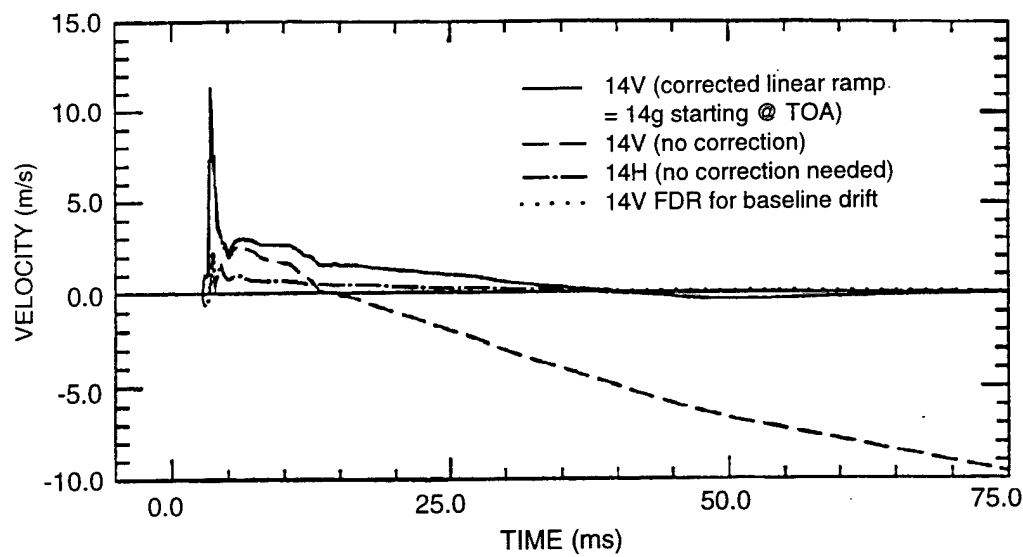
The zero-shifts on this experiment were exceedingly small (less than 0.5% of the peak acceleration), and in several cases there was no shift. The data were corrected by subtracting a linear ramp starting at the time of arrival so that the very late time velocity was brought to zero. Figure 3-4(a) shows the uncorrected and corrected waveforms for 14V. Also plotted is the horizontal component, 14H, which shows no zero-shift. Both the uncorrected waveform for 14H and the corrected waveform for 14V cross zero at about 40 ms. This supports the validity of the simple correction technique used. In any case, the impact of the correction during the simulation time is minimal, as shown in Figure 3-4(b).

Shock-isolation was minimally activated on only three gages: 10V, 12V, and 14V. In all three cases, the associated piston displacements were very small, less than 1 mm. The impact on waveform fidelity was also very small. Gages 10V and 11V were "back-to-back" measurements, and the shock-isolation for gage 11V was not activated. The difference in the displacement at the time of peak velocity for the two gages is approximately equal to the observed piston displacement for 10V, ~0.53 mm.

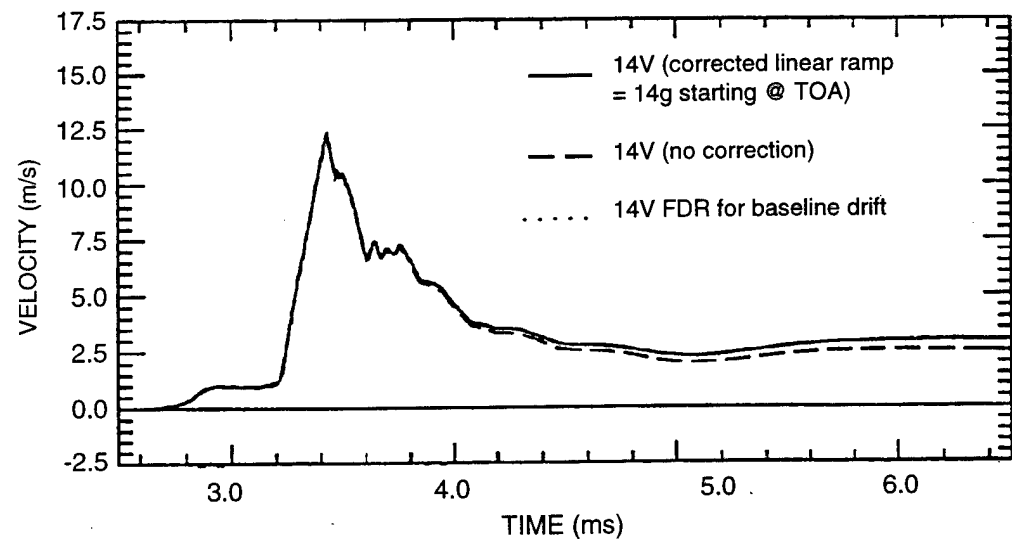
3.3 BOUNDARY CONDITIONS.

The primary purpose of the velocity measurements was to provide data from which to define a continuous velocity boundary condition for computational analyses of the experiment. A velocity boundary condition was created by reconstructing the material velocity field all along the two-dimensional boundary defined by the locations of the accelerometers (slightly inboard of the actual limestone/concrete interface) projected onto the vertical midplane of the test article. The velocity field was assumed symmetric about the vertical plane through the axis of the cylindrical opening.

As illustrated in Figure 3-5, each measured velocity pulse was decomposed into phases representing the key features of the pulse: a precursor, a shock, a ramp to peak, a decay shoulder, and a decay. The amplitude and duration of each phase were tabulated and the functional forms were found that best fit the variation of these parameters with measurement position. The actual phases of each pulse were then

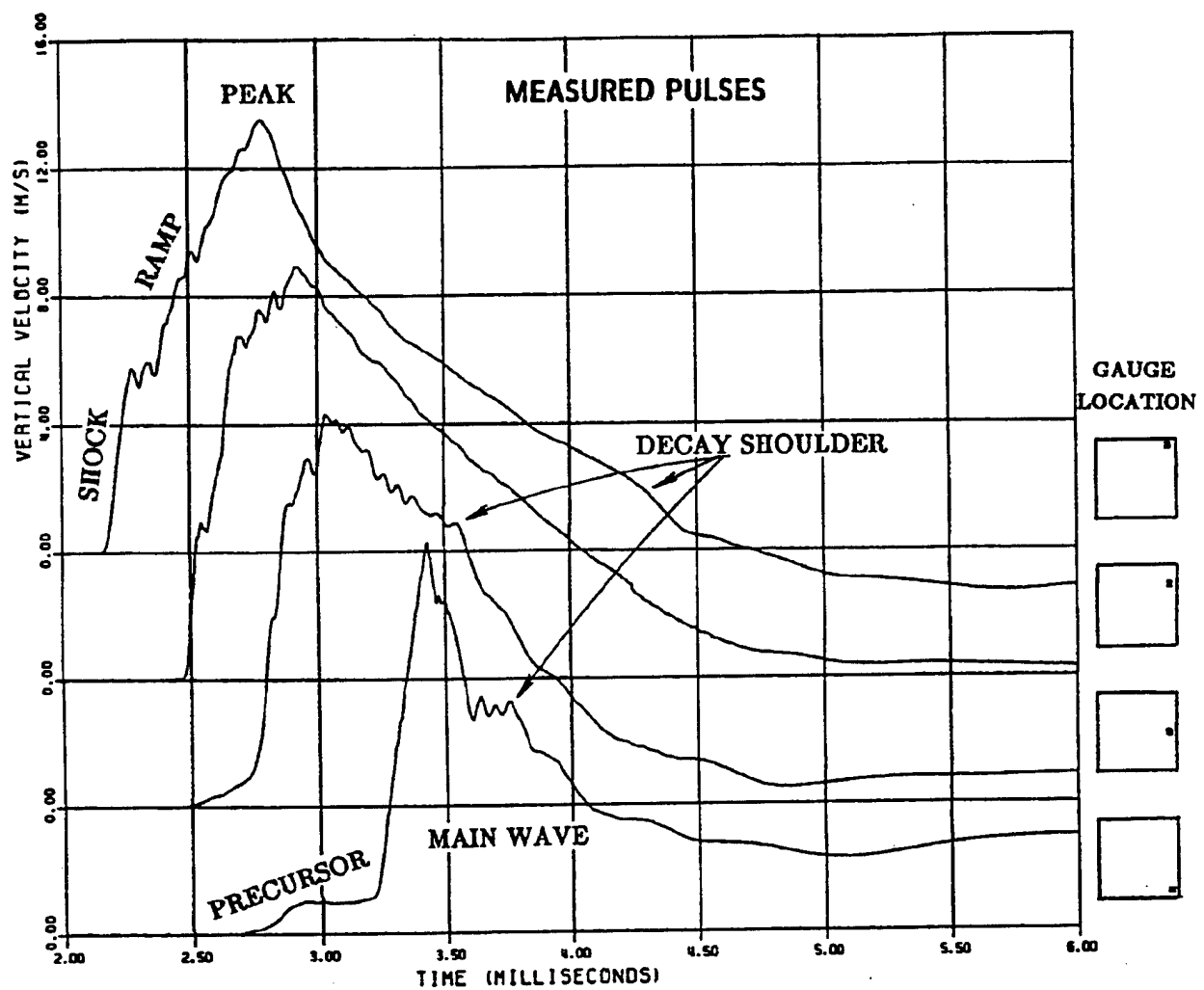


(a) Long duration plot



(b) Short duration plot

Figure 3-4. Zero-shifts and impact of correction.



INPUT PARAMETERS READ FROM PULSES:

- TIME OF PRECURSOR ARRIVAL, t_a
- TIME OF MAIN-WAVE ARRIVAL, t_m
- TIME OF SHOCK PEAK, t_s
- TIME OF PEAK VELOCITY, t_p
- TIME OF SHOULDER DECAY FROM PEAK, t_d
- PRECURSOR AMPLITUDE, u_p
- SHOCK AMPLITUDE, u_s
- PEAK VELOCITY, U
- VELOCITY AT SHOULDER DURING DECAY, u_d

Figure 3-5. Decomposition of velocity pulses into phases.

normalized by the *fit* values of the amplitude and duration, preserving continuity at the seams between phases by linearly variable amplitude normalization. Simple spatial interpolation then provided normalized phases at the points on the boundary between measurement stations. Finally, the interpolated normalized phases were rescaled to fit values of amplitude and duration. In this manner, not only is the generation and degeneration of waveform features preserved but also the "noise" in the measured pulses is captured in the continuous field.

The uncertainty in the fit is quite low. For example, with 0.9 confidence, the peak vertical velocity is uncertain by less than 10% at all points. That is, for a large number of identical experiments, 90% would produce fits to the peak vertical velocities within 10% of this fit. Similarly, with 0.9 confidence, the peak horizontal velocity is uncertain by about 10%, and shock transit time through the test article is uncertain by about 6%.

3.4 CLOSURES.

The closure gages, even having been extensively tested during the design and fabrication phase, did not function during the test. Posttest recovery of the liner led to the determination that all eight photo diodes were inoperable, but how or when they were damaged could not be determined.

Lack of dynamic closure data was, in part, mitigated by the opportunity to make posttest measurements of permanent closure when the liner was recovered from the test article. The recovered liner was mounted in a special spindle with two radial arms attached to the axle, supporting a measurement track running along the outside of the liner. A deflection gage attached to the track could be positioned to measure the outside radius of any point on the liner. The radius was measured first at the point of the crown at one end. The deflection gage was set to zero at that single point so all the radius measurements were taken relative to that point; then the radius at each point was obtained by adding the radius of the reference point, which is $R = 198.48$ mm. Measurements were taken along a generator at intervals of 25.4 mm and at angular intervals of 8° ; this angle subtends an arc of about 28.37 mm, which is comparable to the axial spacing. These spacings provide 4095 readings on 45 generators and 91 circles. These measurements were fit with two, single, Fourier series using 10 terms for the angular coordinate and 20 terms for the length coordinate.

$$w(\theta) = r(\theta) - r_0(\theta) = \frac{1}{2} c_0 + \sum_{n=1}^{10} c_n \cos(n\theta) + d_n \sin(n\theta) \quad (3.1)$$

$$w(x) = r(x) - r_0(x) = \frac{1}{2} a_0 + \sum_{n=1}^{20} a_n \cos(n\pi x/L) + b_n \sin(n\pi x/L) \quad (3.2)$$

Pretest radii were determined from measurements of crown-invert diameter and springline diameter at nine equally spaced positions along the length of the liner. At all axial locations, the pretest radius was adequately represented by

$$r_0(\theta) = R_0 - R_2 \cos 2\theta \quad (3.3)$$

where R_0 averaged 203.26 mm and R_2 averaged 0.33 mm.

The character of the deformed shape is displayed in Figures 3-6 and 3-7, which show plots of the deformed circumference at three axial positions and the deformed meridian along the crown, invert, and both springlines.

The circumferential deformation exhibits excellent side-to-side symmetry (North-to-South in Figures 2-14 and 2-15) and is dominated by the symmetric mode ($n = 0$) and the ovaling mode ($n = 2$). Higher order modes were not noticeable and higher order terms were essentially negligible. Evidence of variation along the length of the liner is clear, with maxima and minima coincident with the locations of the joints between brick *ends* (at $x = 0$ and $x = \pm 610$ mm). Over the central half of the length (-610 mm $< x < +610$ mm), the average crown-invert deflection is -10.31 mm (closure) with a standard deviation of 0.72 mm. The average springline diameter change is +5.43 mm (opening) with a standard deviation of 1.40 mm. Related to the original outer diameter, these measurements give an average vertical closure of 2.5% and an average springline opening of 1.3%.

3.5 STRESSES.

All the flatpack stress gages provided clear signals for the duration of the experiment. Figure 3-8 provides a typical example of ytterbium and constantan resistance histories. In general, the strains registered by the constantan elements were small (0.2%), but were important in determining the resolved stresses, particularly for stresses below about 30 MPa.

The stresses measured by FP25 and FP26, shown in Figure 3-9(a), probably best indicate the "free field" stress at the depth of the lined cylindrical opening in the test article, because these gages were about one liner diameter from the springline. The peak stress here was about 75 MPa, the rise time was about 300 μ s, and the pulse duration was about 3.5 ms. The records from these two gages are nearly identical, indicating very good symmetry in the stress wave. Stresses very near the springlines are given by FP23 and FP28, shown in Figure 3-9(c). These records are also nearly identical, but the peak stresses are about 100 MPa. Gages FP29 and FP22 were located between these two pairs but, contrary to expectations, the stresses they recorded were not intermediate. As shown in Figure 3-9(b), the peaks average about 55 MPa (lower than the 75 MPa measured further from the tunnel) and the symmetry is not nearly as good.

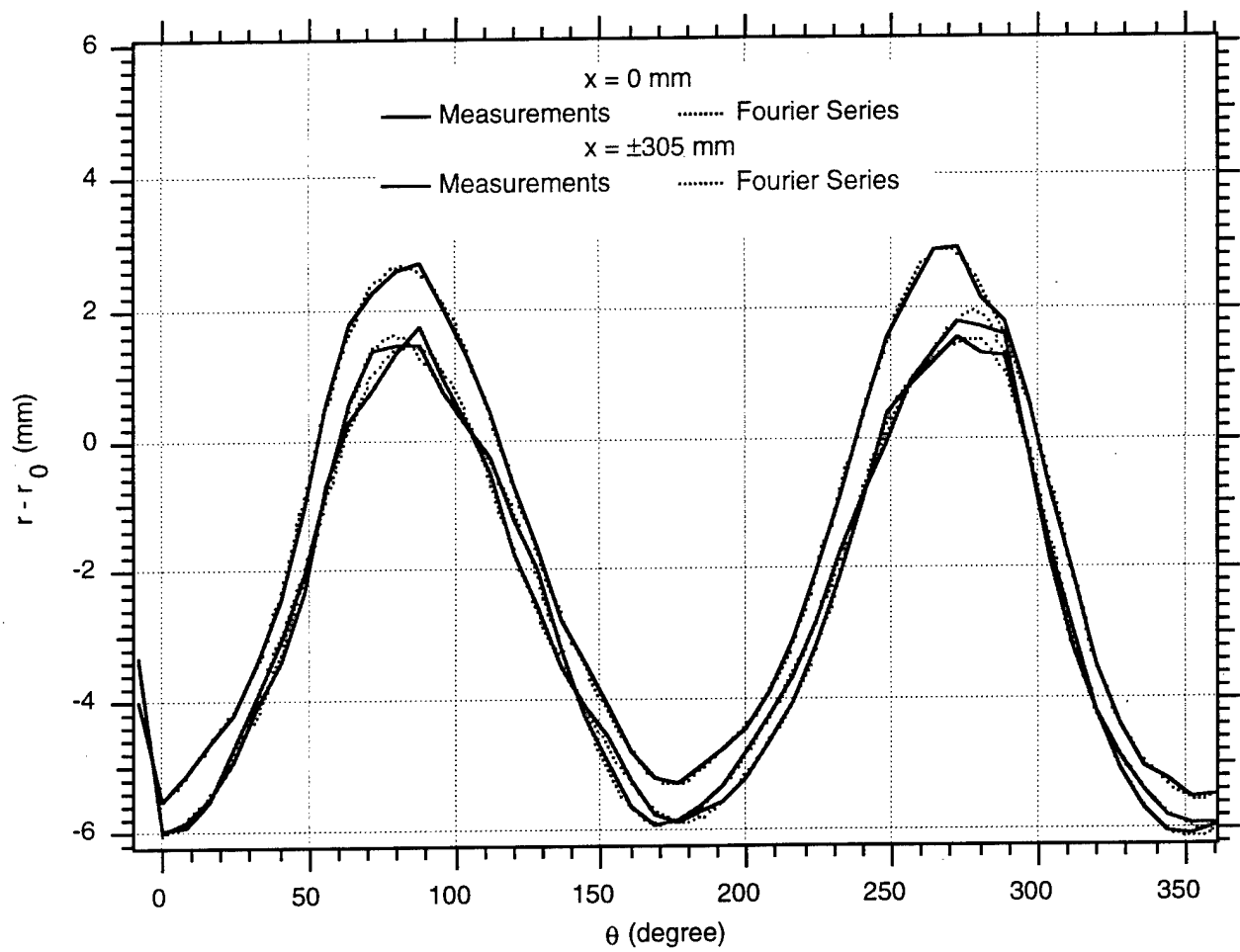


Figure 3-6. Circumferential variation of liner deformation.

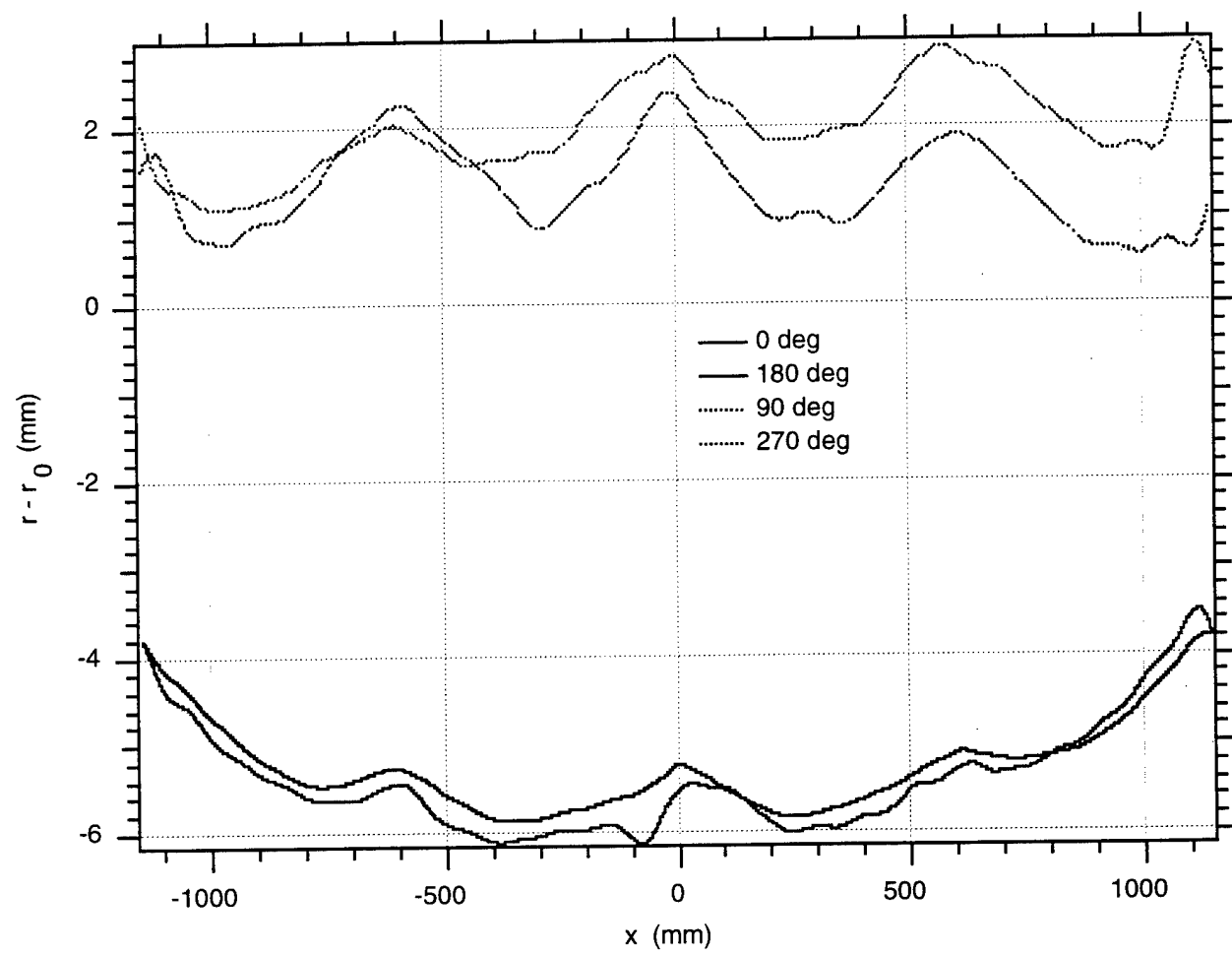


Figure 3-7. Axial variation of liner deformation.

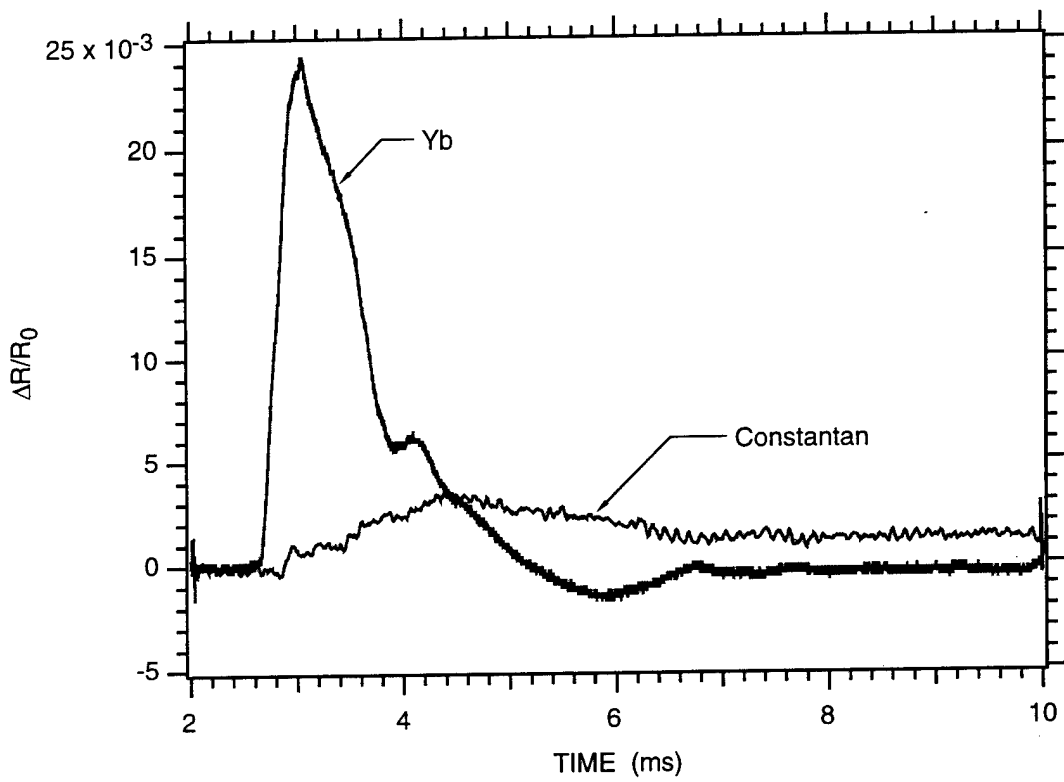


Figure 3-8. Typical resistance histories.

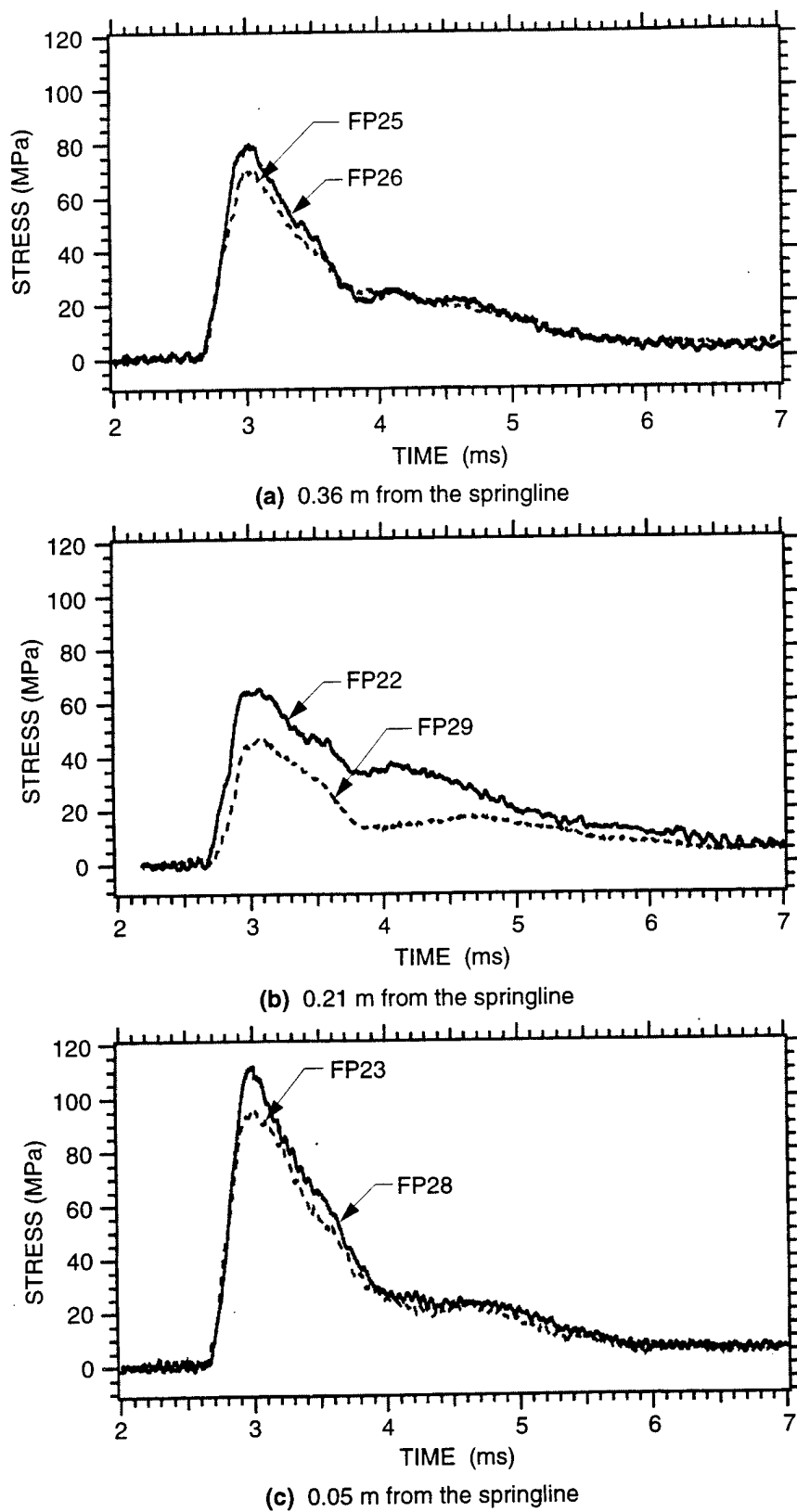


Figure 3-9. Vertical stresses 25 mm above the plane of the springline.

The stresses above the tunnel crown were measured by FP24 and FP27. The records from these gages, plotted in Figure 3-10, clearly show that the incoming stress wave was clipped by reflections from the tunnel. Also, the rise time at the 230-mm depth in the test article (FP24) was about twice as long as at the tunnel springline depth (FP 25 and 26), indicating that the stress wave front steepened as it propagated through the jointed limestone which is similar to the effect observed in the velocity measurements.

3.6 JOINT SLIP.

Data were obtained from all slip gages, although the amount of slip during the time of interest was on the order of 1 mm, and at most locations was much smaller than pretest predictions. Consequently, each signal had to be filtered to some extent to remove the transmitter cross-coupling noise. In addition, some of the signals indicated intermittent shorting of a winding or two of the sensor coil, but in general this could be corrected in the data processing.

As mentioned above, the slip gages were arranged in sets of two receivers with one transmitter coil so that slip produced a positive signal in one receiver and a negative signal in the other. This mirror image response is apparent in the data and is shown in Figure 3-11(a) for gage B2 (the gages are "turned on" at zero time, producing the initial step up from the baseline). When converted to slip, the records shown in Figure 3-11(b) are produced. Positive slip corresponds to bricks above the interface moving outward (away from the lined opening) relative to the bricks below the interface. Slip during the first few milliseconds at this location is positive and very small and slip grows negatively until the horizontal motion ceases (indicated by the horizontal velocity). This pattern of early, small, positive slip followed by late larger slip is typical of the rest of the measurements, although not all showed the same extreme negative excursion. The permanent slip determined posttest from a measurement of mutual inductance is well within the uncertainty of the late-time dynamic measurement. The estimates of uncertainty are based on prefueling laboratory measurements.

In addition to the posttest mutual inductance measurement, we made a physical inspection of permanent slip. As described below, scribe lines made between brick layers during the assembly of the test article were used as reference points for measurement of posttest slip. Figure 3-12 is a graph of the permanent slip measured at the interface tangent to the crown of the liner using the two techniques. The average is $-1 \text{ mm} \pm 0.5 \text{ mm}$ (s.d.) for the EM technique and $-2 \text{ mm} \pm 0.7 \text{ mm}$ (s.d.) for the physical inspection. In essence, we performed an *in-situ* gage validation.

During the passage of the main stress wave through the test article, the slip gages closest to the lined opening, R1 and B1, show an initial slip of between $+0.5$ and $+2 \text{ mm}$, as shown in Figure 3-13(a) and (b). The transmitter for B1 failed at $t = 3 \text{ ms}$, and the signal from R1-2 became very noisy when receiver

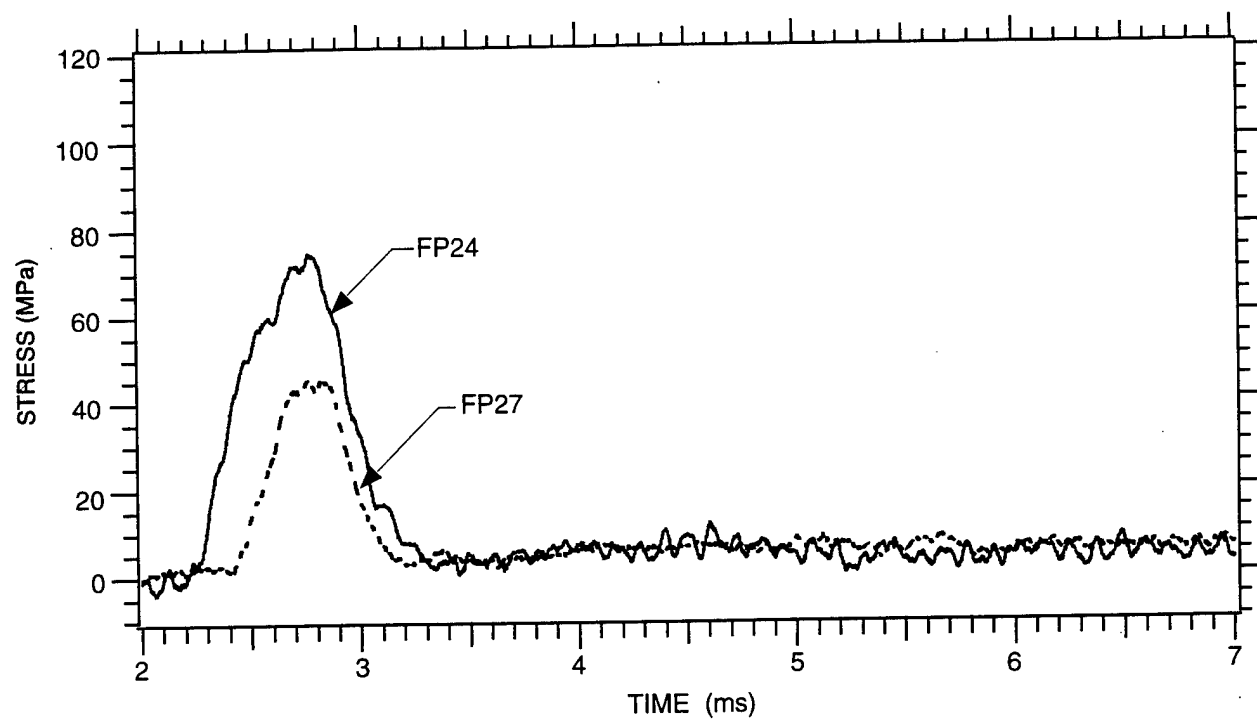
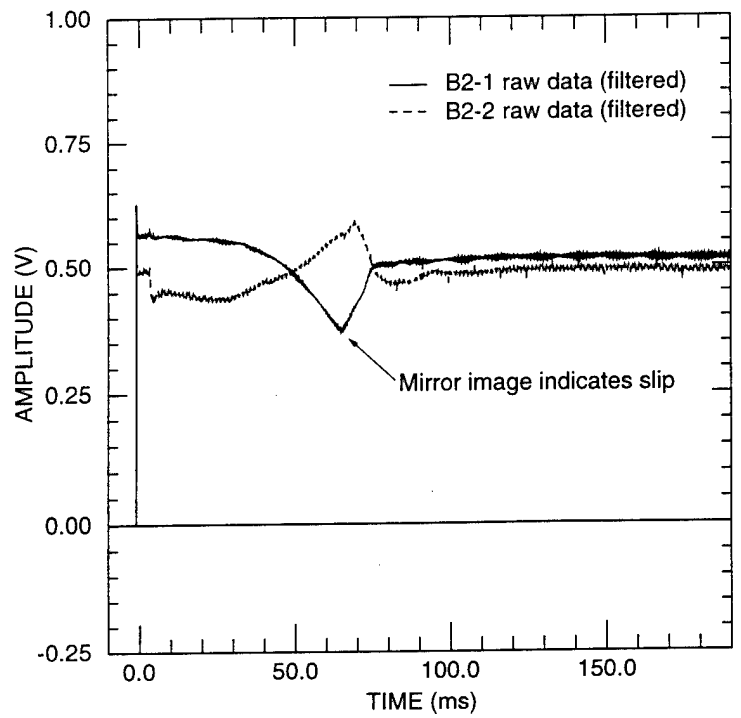
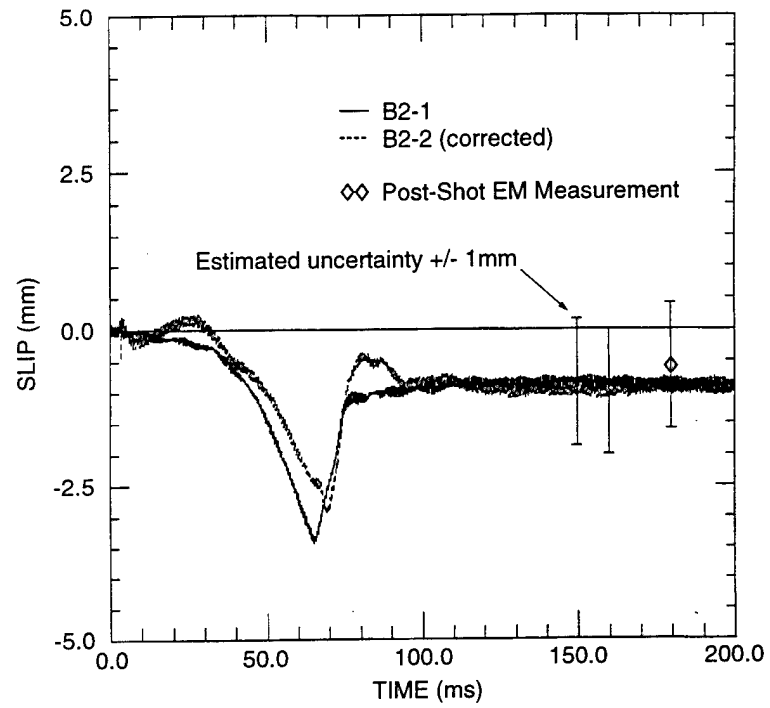


Figure 3-10. Vertical stresses on the center line, 0.84 m and 0.53 m above the tunnel axis (0.64 m and 0.33 m above the crown).



(a) Raw data for B2 showing mirror image signal



(b) Data from B2 reduced to slip with post-test determination of permanent slip

Figure 3-11. EM slip gage data.

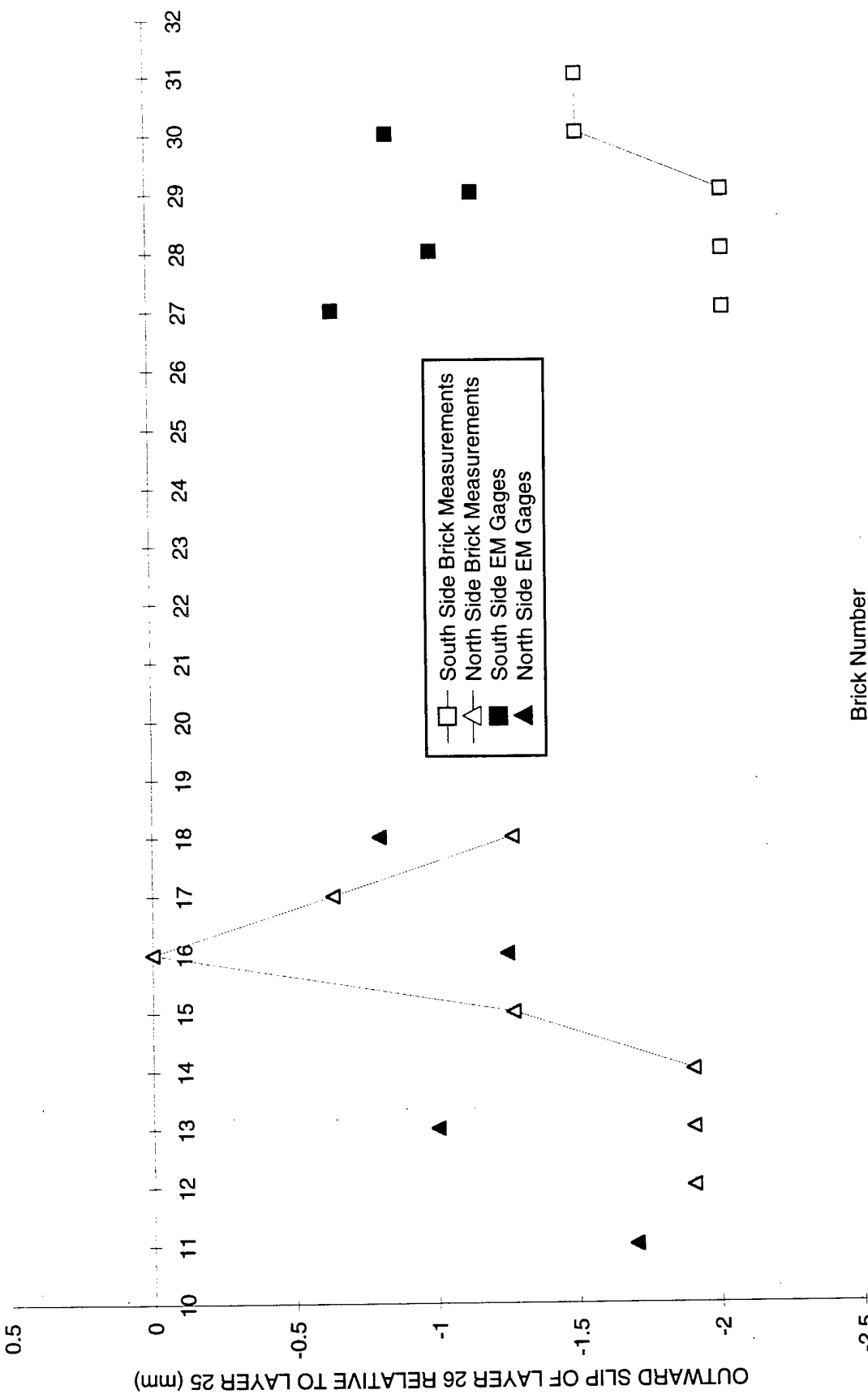
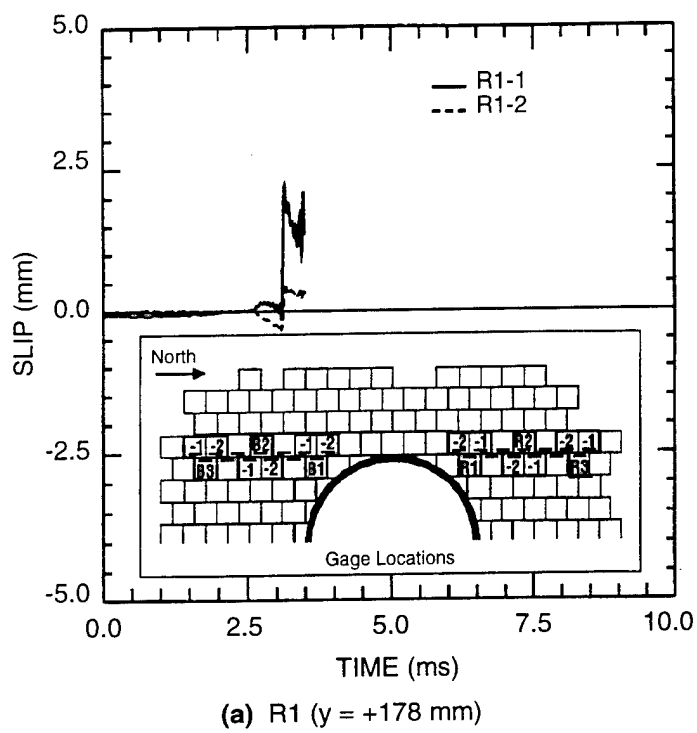
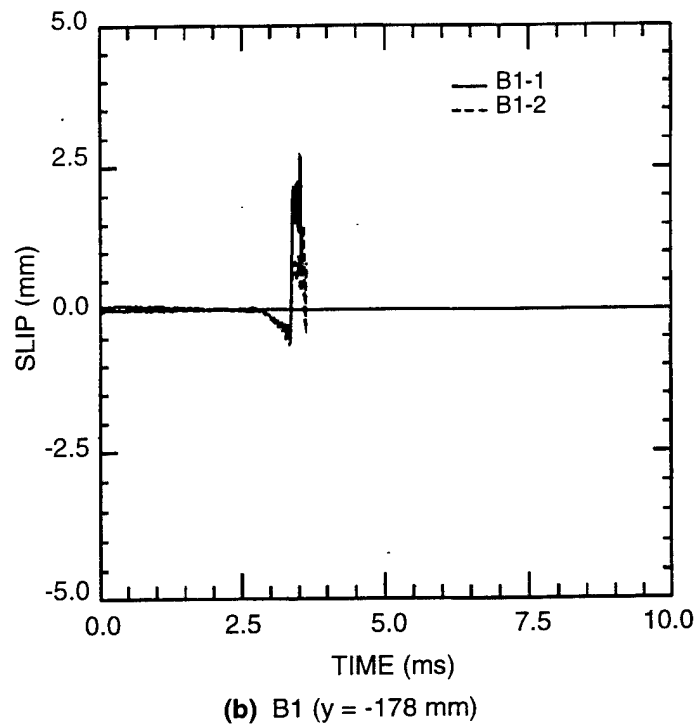


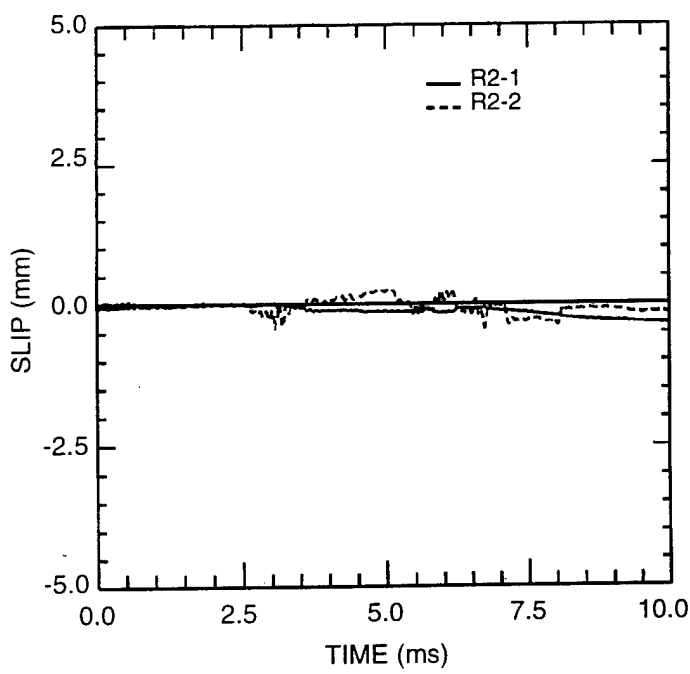
Figure 3-12. Posttest slip at the EM slip gage interface estimated uncertainties are ± 1 mm for all measurements.



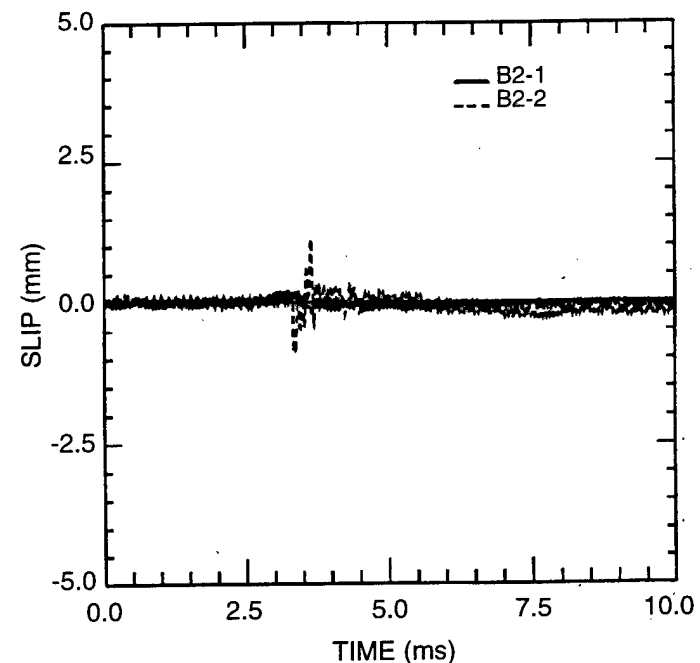
(a) R1 ($y = +178$ mm)



(b) B1 ($y = -178$ mm)



(c) R2 ($y = +305$ mm)



(d) B2 ($y = -305$ mm)

Figure 3-13. Horizontal slip measurements.

R1-1 failed at $t = 3.5$ ms. However, the noise burst attenuated, allowing the R1-1 signal to be interpretable again after a few milliseconds; the late-time slip was about -1 mm. Figure 3-13(c) and (d) shows that little or no slip occurred during the simulation time for B2 and R2, although they both indicated a late-time slip of -1.2 mm. Cross-coupling between transmitters occurred in the gages furthest out, R3 and B3, and signal contamination was significant enough to require very heavy low pass filtering. The late time slip indicated by both gages (-0.9 mm) is in agreement with the measured permanent slips and is consistent with the other gages, but the quality of the records is not sufficient to precisely evaluate the slip during the simulation time, except to suggest that it is very small.

Thus, in general, the dynamic slip measurements were successful, but most of the slip at the measurement locations occurred much later than the time of interest, and even the peak total slip was very small.

3.7 POSTTEST OBSERVATIONS.

Following the test, the concrete surrounding the test article was removed so that we could observe the damage to the limestone bricks and the deformed shape of the liner. The bricks were removed layer by layer and the profile of each layer was measured. The locations of all visible cracks were noted. Near the opening, permanent relative slip between bricks was measured using scribe lines placed in the bricks during the stacking. The liner was removed and its deformed shape was measured all along its length. These data provide invaluable insight into the response mechanisms of an opening in jointed rock. The test article was excavated by removing the test-bed concrete above and around it to a depth just below the opening. Then the concrete cover of the test article was removed from the top and both ends. Each brick was removed, one by one, and measurements were made of overall test article dimensions and relative displacement between bricks at each layer.

Measurements of test article height indicated (on average) no change (within the accuracy of those measurements), although the inside surface of the concrete walls showed evidence that the limestone moved downward relative to the concrete. Measurable expansion of the test article occurred in both lateral directions (about 1%), accounted for entirely by the opening of end-to-end joints and side-to-side joints and fractures. The only evidence of limestone compaction was at the surface of the liner. Almost all the brick damage was in the form of vertical splitting down the centerline, typically running the entire length of a brick. However, as discussed below, this damage was concentrated around the opening. Unsplit bricks removed from the test article had the same dimensions (statistically) as pretest.

The displacement and fracture patterns that were observed and quantified are of vertical cleavage emanating upward from the springlines forming a chimney of bricks separated from the rest. The cleavage fractures tended to occur slightly toward each other and disappeared before reaching the top surface. Figure 3-14

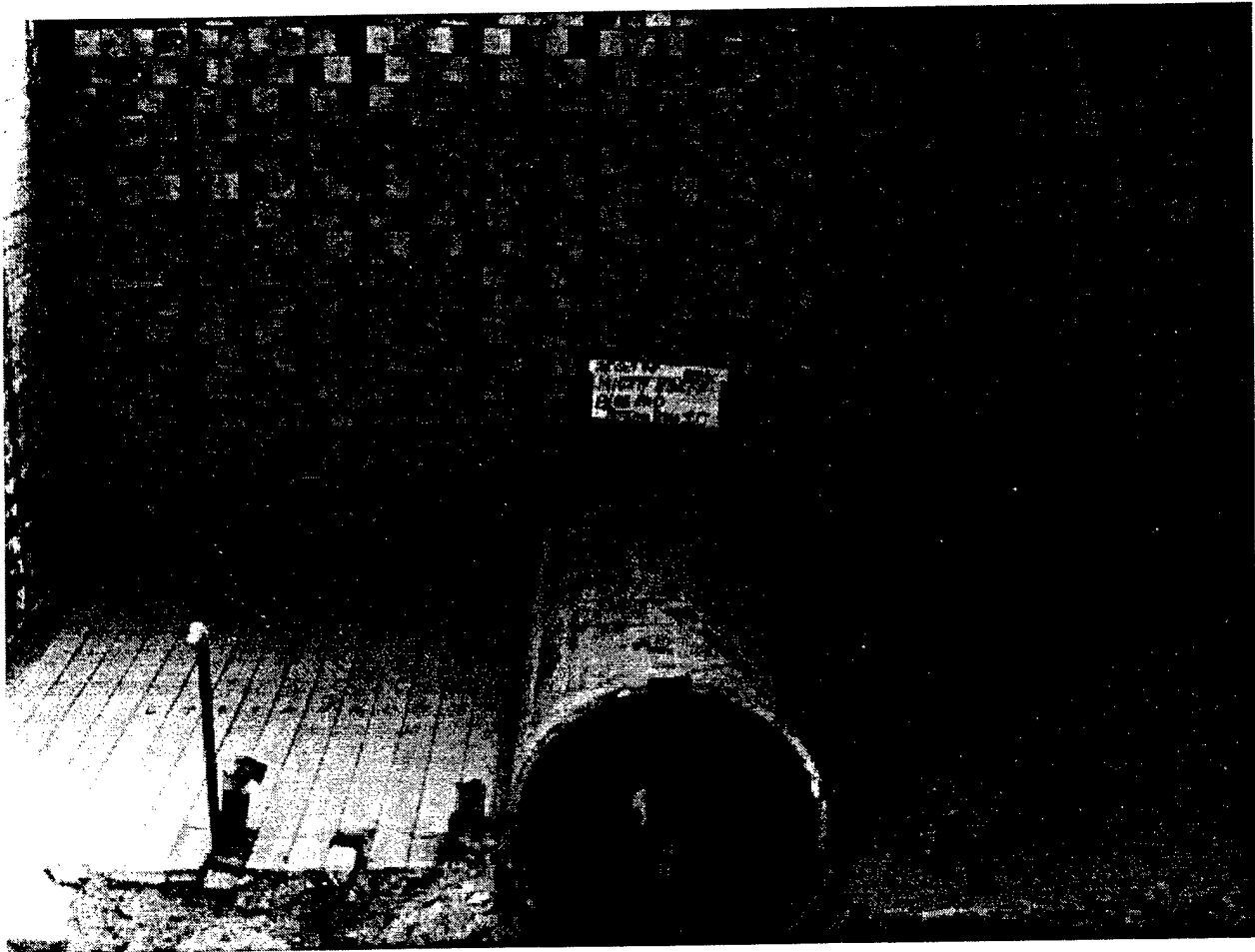


Figure 3-14. MIGHTY NORTH 1 jointed limestone faulting above the tunnel.

shows the upper half of the midplane of the test article during disassembly. Above the springlines, the relative displacement at the cleavage planes was about 10 mm, with the bricks within the chimney moving downward relative to the rest of the test article. The cleavage planes also extended downward from the springlines, but only a few layers. In this region, the relative displacement was about 2 mm, with the material outside the cleavage planes moving downward relative to the material between the cleavage planes. The sum of the shear displacement above the opening and below the opening (about 12 mm) agrees very well with the average crown-invert deformation of the liner.

Layer profiles were measured ± 305 mm from the midplane by measuring the distance from the top of each brick to a tight string nominally 50 mm above the layer and stretched from one side of the test article to the other. For split bricks, we recorded two measurements. The vertical displacement patterns determined from these measurements are illustrated in Figure 3-15 for one section. In this figure, the relative vertical displacements have been amplified by a factor of 2 and no horizontal displacements are included. Figure 3-16 shows an expanded view of the bricks near the opening (with zero displacement); the areas of comminution are noted.

Average horizontal expansion in each layer was determined from pretest and posttest measurements of the width (w) of the test article at each end and at the midplane. These expansions, plotted in Figure 3-17, average about 0.7% and show a trend of larger expansions toward the bottom of the test article. These measurements were made with a tape measure and an error of 1 mm corresponds to about 0.0005.

Permanent relative horizontal slip was also measured ± 305 mm from the midplane, in the ten layers above the springline, over a width encompassing ten bricks to each side of the axis of the opening. During assembly of the test article, a tool-steel scribe was used to scratch a line in the top of each brick along the edge of the brick placed above it. Then the distance from the vertical face of the upper brick to the scribe line was measured posttest. The slip of each brick relative to the one just below was determined for the ten layers just above the springlines, and the measurements from the four quadrants of the test article (in plan view) were averaged. Unfortunately, most of the scribe lines were damaged by flaking off at their edges and their width grew to about 1.25 mm, so there is about that much uncertainty in these measurements. Also, the fracture of some bricks prohibited several measurements, requiring interpolation between measurements.

Figure 3-18 shows the compilation of the permanent cumulative slip (relative to the interface between layers 21 and 22). The diameter of the opening spans from brick 17 to brick 26; only the right half of the measured zone is displayed because the averaged data are symmetric. Outside the vertical faults at brick 26, the slip between layers was generally less than 1 mm and the cumulative slip in this region relative to the interface at the springline was essentially zero up to layer 26, but over 1 mm outward slip was

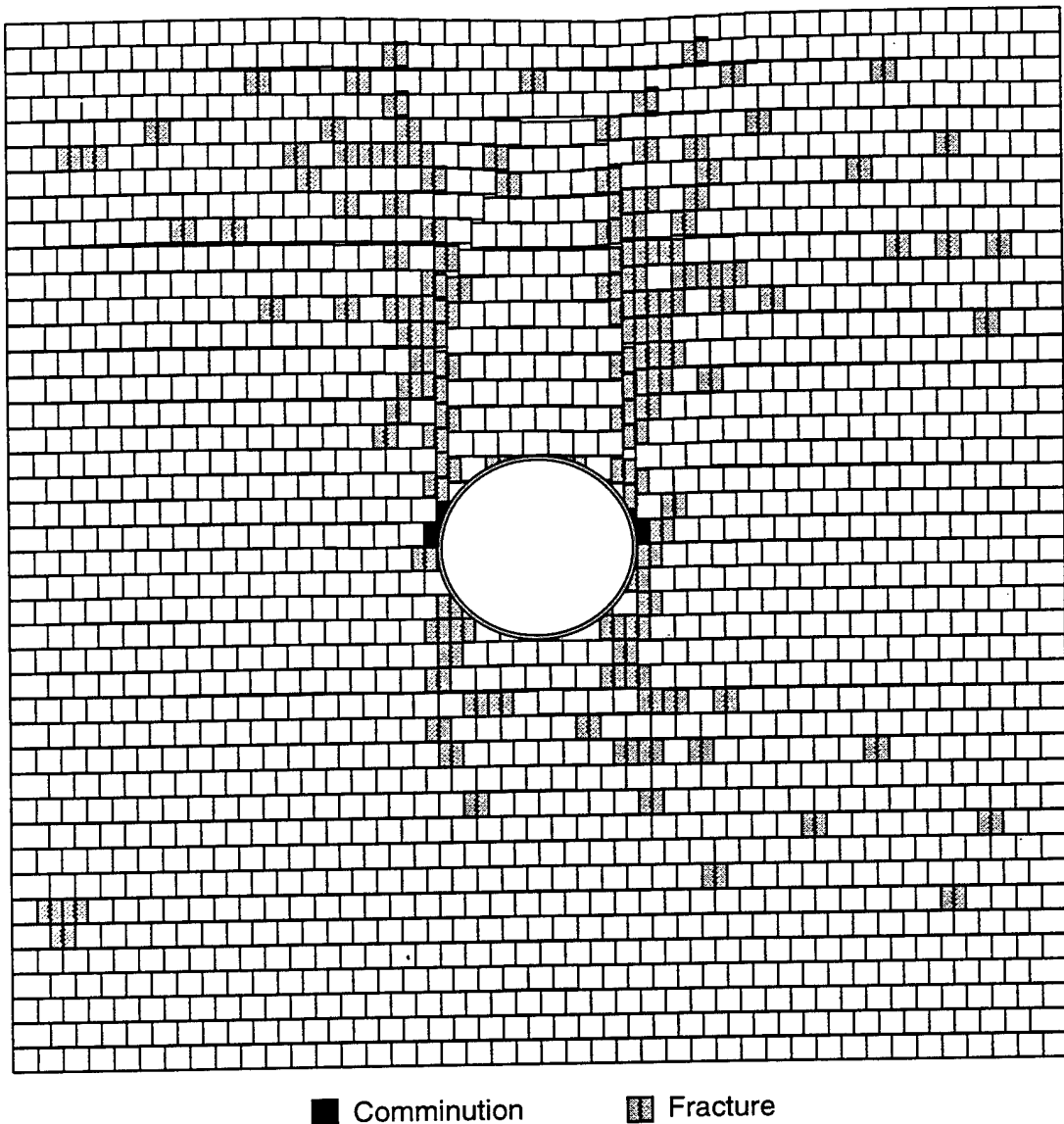


Figure 3-15. MIGHTY NORTH 1 jointed limestone deformation and damage at $x = +305$ mm.
(Vertical Displacement Scale Factor = 2)

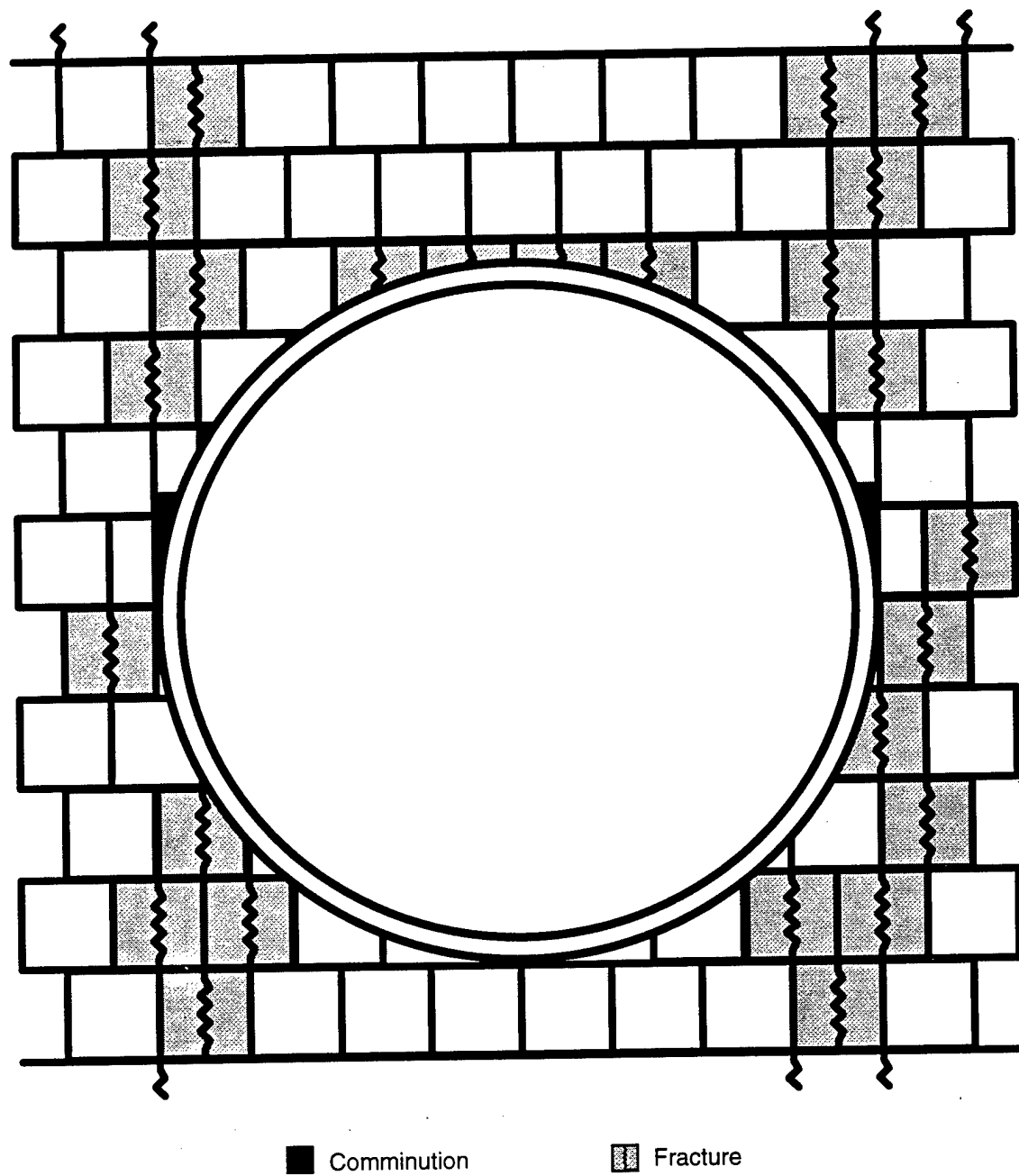


Figure 3-16. MIGHTY NORTH 1 jointed limestone deformation and damage at $x = +305$ mm.
(Vertical Displacement Scale Factor = 0)

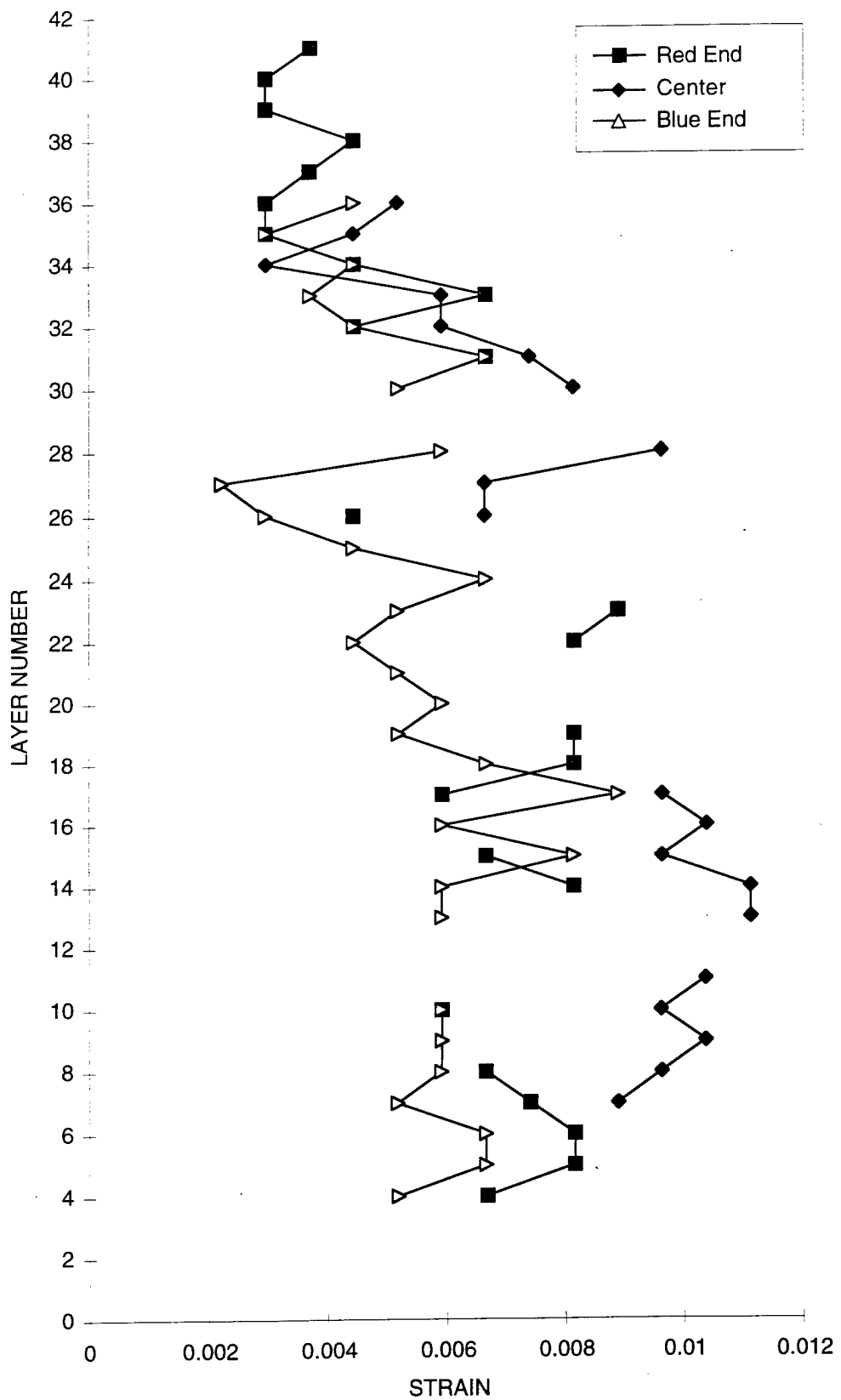


Figure 3-17. MIGHTY NORTH jointed limestone test article posttest horizontal strains.

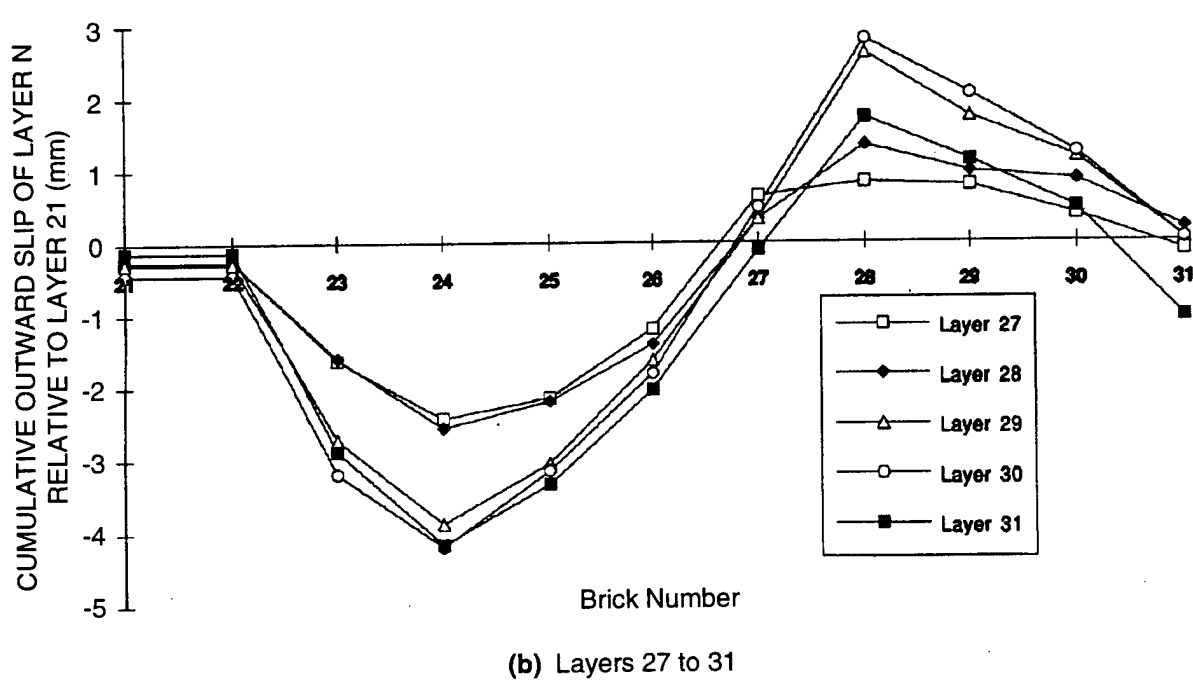
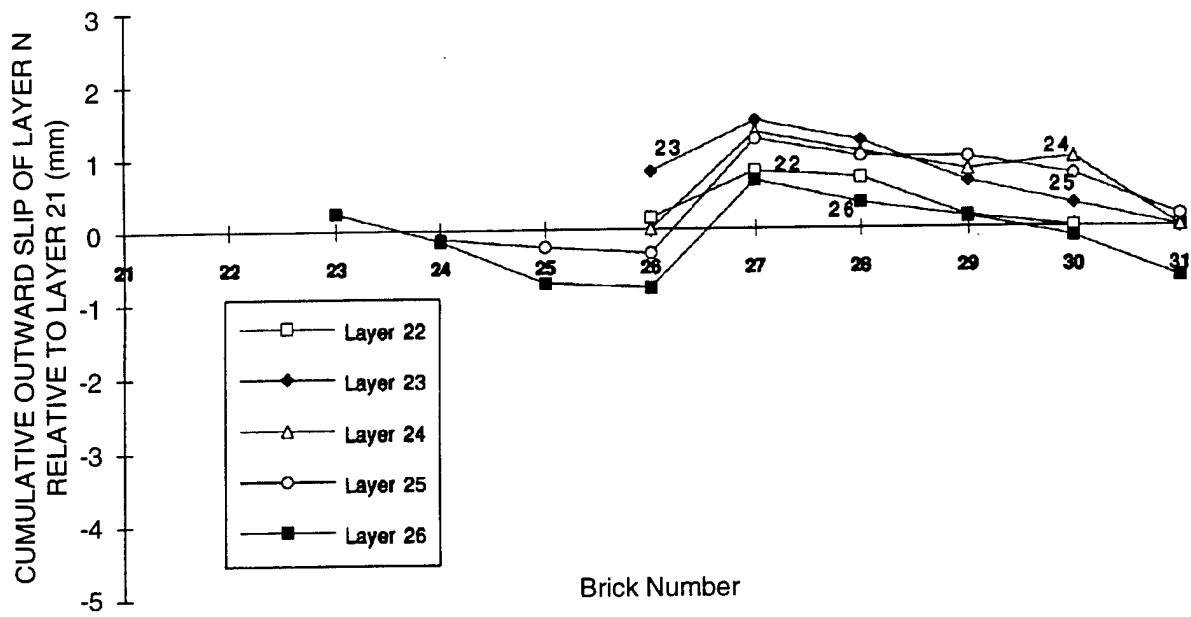


Figure 3-18. Average symmetric cumulative slip measurements.

measured between layers 29 and 28. Within the chimney directly over the lined opening, the largest slips occurred between layers 27 and 26 (one interface above the crown of the liner and the interface with the electromagnetic slip gages) and between layers 29 and 28. The cumulative slip in this region was negative (inward relative to the interface at the springline) and it localized at these two interfaces.

Figure 3-19 presents a simplified kinematic interpretation of the slip pattern. Recall that the springlines of the liner moved outward about 2 mm. Also, the wedge-shaped bricks in layer 23 (just above the springline) were pushed down and between the liner and the innermost brick of layer 22, which would tend to push the bricks in layer 22 outward further relative to the springline interface, as shown in Figure 3-16. Thus, the bricks outside the chimney generally moved outward, and all layers split at the vertical fault and the outer bricks moved along with the material below while the bricks within the chimney lagged.

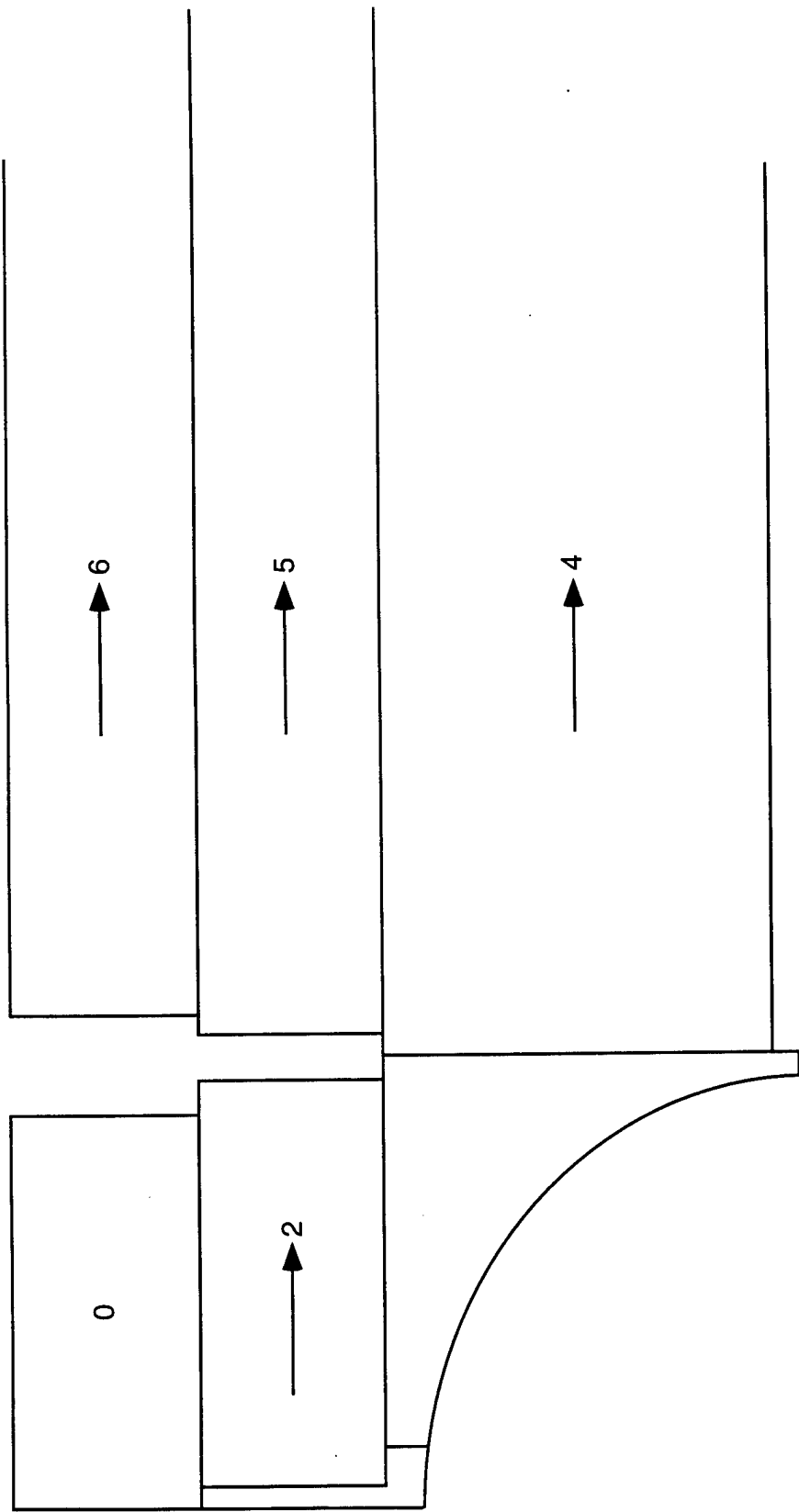


Figure 3-19. Simplified kinematic interpretation of the slip pattern.

SECTION 4

CONCLUSIONS AND RECOMMENDATIONS

4.1 CONCLUSIONS.

Designing, fabricating, characterizing, instrumenting, fielding, and inspecting the MIGHTY NORTH 1 jointed limestone test article was a significant challenge but a tremendous success. The quality of the assembly was extremely high, the precision of the measurements was excellent, and the response information obtained is extremely important. The velocity data were particularly outstanding.

The posttest measurements clearly indicated the directionality of the response. That is, the damage in the jointed limestone was not symmetric from top to bottom. Much more shear displacement at the vertical faults occurred above the tunnel than below it. Also, with this response mechanism (shear plugging above the tunnel), the role of the liner is significant.

The response of the central half (end-to-end) of the test article was very uniform, as observed in the posttest measurements of the tunnel liner and brick damage. All the active measurements were made in this region. The combination of uniform response, precision measurements, boundary condition definition, and material properties make this test suitable for use in validating computer models for deformation of structures in jointed media.

4.2 RECOMMENDATIONS.

The posttest measurements of residual deformation in the test article were credible and valuable, and should be performed on future tests. Assembling the test article at SRI facilities in Menlo Park, with access to shops, labs, and stores worked well. Shipment to the test site and placement into the test article went smoothly. Remote assembly also allowed testbed preparation and test article construction to proceed in parallel, savings many weeks of project time. As always, more measurements should be included, especially of velocity and stress.

The systematic failure of the closure gages makes it obvious that a redundant design of closure gages should have been included. Even simple strain gages on the inside surface of the liner would provide the time history of deformation. These should be included in future tests.

Perhaps a higher load would be more interesting. To study the role of the joints in the observed fracture patterns, we recommend fielding a test article with thicker bricks and one with irregular joints spacing (brick width). Because so little slip occurred, there does not appear to be good reason to study joint roughness, but perhaps joint opening (gap) could be varied.

SECTION 5

REFERENCES

1. Senseny, P. E. and H. E. Lindberg, "Theoretical and Experimental Study of Deep-Based Structures in Intact and Jointed Rocks," SRI Final Report for Contract DNA001-76-C-0385 (September 1979). (UNCLASSIFIED)
2. Senseny, P.E. and D.A. Simons, "Comparison of Calculational Approaches for Structural Deformation in Jointed Rock," *Int. J. for Numer. and Anal. Meth. in Geomech.* **18**, 327-344 (1994). (UNCLASSIFIED)
3. Chen, D. Y., Y. M. Gupta, and M. H. Miles, "Quasistatic Experiments to Determine Material Constants for the Piezoresistance Foils Used in Shock Wave Experiments," *J. Appl. Phys.* **55**(11), 3984 (June 1984). (UNCLASSIFIED)
4. Gran, J. K. and L. Seaman, "Analysis of Multiple Piezoresistance Measurements to Determine Stress in Divergent Flow," *ASCE J. of Engng. Mech.* (January 1997). (UNCLASSIFIED)
5. Lilley, E. M. and D. R. Stephens, "Electrical Resistance of Ytterbium as a Function of Temperature and Pressure," UCRL-51006, Lawrence Radiation Laboratory, University of California, Livermore, CA (February 1971). (UNCLASSIFIED)
6. Goodfellow, G. and E. Rinehart, "MIGHTY NORTH 1, Volume 2—Results Report," Defense Nuclear Agency, Field Command, POR 7484-2 (August 1995). (UNCLASSIFIED)
7. Simons, D. A., "Numerical and Analytical Solutions to Benchmark Problems Related to Tunnel Mechanics," DNA-TR-92-176 (September 1993). (UNCLASSIFIED)
8. Hoek, E. and E. T. Brown, "Underground Excavations in Rock," The Institution of Mining and Metallurgy, London (1980). (UNCLASSIFIED)
9. Fossum, A.F., P.E. Senseny, T.W. Pfeifle and K.D. Mellegard, "Experimental Determination of Probability Distributions for Parameters of a Salem Limestone Cap Plasticity Model," *Mech. of Mater.* **21**, 119-137 (1995). (UNCLASSIFIED)
10. Brown, G. W. and G. A. Drago, "Shock Calibration of Accelerometers Using Hopkinson's Bar," UCRL 13725, ME #77-3, University of California, Berkeley, CA (March 1977). (UNCLASSIFIED)
11. Petersen, C. F. and M. A Groethe, "Reasearch on HML/ASH Environment, Task 6—Instrumentation Development, ASH," DNA-TR-88-69 (February 1988). (UNCLASSIFIED)
12. Ueda, K. and A Umeda, "Characterization of Shock Accelerometers Using Davies Bar and Strain Gages," *Experimental Mechanics*, 228-233 (September 1993). (UNCLASSIFIED)
13. Senseny, P. E., J. Duffy, and R. H. Hawley, "Experiments on Strain Rate History and Temperature Effects during the Plastic Deformation of Close-Packed Metals," *ASME Journal of Applied Mechanics* **45**(1), 60-66 (1978). (UNCLASSIFIED)

14. Clifton, R. J., "High Strain Rate Behavior of Metals," *ASME Applied Mechanics Reviews* 43(5), Part 2, S9-S22 (1990). (UNCLASSIFIED)
15. Gilat, A., "An Experimental and Numerical Investigation of Pressure-Shear Waves in 6061-T6 Aluminum and Alpha-Titanium," PhD Thesis, Division of Engineering, Brown University (August 1982). (UNCLASSIFIED)
16. Simons, J. W., L. Seaman, P. R. Gefken, and A. L. Florence, "Tunnel Tests in Limestone," DNA-TR-92-164 (October 1992). (UNCLASSIFIED)
17. Klopp, R. W. et al., "Laboratory Tests in Support of the Underground Technology Program (UTP)," DNA-TR-94-183-Rev. (December 1994). (UNCLASSIFIED)

DISTRIBUTION LIST
DSWA TR-96-63

DEPARTMENT OF DEFENSE

DEFENSE INTELLIGENCE AGENCY
ATTN: TWJ

DEFENSE SPECIAL WEAPONS AGENCY
ATTN: OPS
ATTN: PMT, P SENSENY
2 CY ATTN: TRC
ATTN: WEL, D RICE
ATTN: WEP, W ULLRICH

DEFENSE TECHNICAL INFORMATION
2 CY ATTN: DTIC/OCP

FC DEFENSE SPECIAL WEAPONS AGENCY
ATTN: FCTO
ATTN: FCTOS
ATTN: FCTT, DR BALADI

DEPARTMENT OF THE ARMY

ADVANCED RESEARCH PROJECT AGENCY
ATTN: DEFENSE SCIENCES OFFICE

U S ARMY CORPS OF ENGINEERS
ATTN: CERD-L

U S A RMY ENGINEER DIST OMAHA
ATTN: MROED-S H GAUBE

U S ARMY ENGR WATERWAYS EXPER STATION
ATTN: C D NORMAN
ATTN: CEWES-SD
ATTN: MR L K DAVIS, CEWES-SE
ATTN: DR D BANKS, CEWES-GS
ATTN: J WARRINER, WESGR-M
ATTN: TECHNICAL LIBRARY
ATTN: W MCMAHON
ATTN: W MILLER

DEPARTMENT OF THE AIR FORCE

AIR FORCE CTR FOR STUDIES & ANALYSIS
ATTN: AFSAA/SAI, RM 1D363 THE PENTAGON

AIR UNIVERSITY LIBRARY
ATTN: AUL-LSE

DEPARTMENT OF ENERGY

LOS ALAMOS NATIONAL LABORATORY
ATTN: MS P364 REPORT LIBRARY

SANDIA NATIONAL LABORATORIES
ATTN: A F FOSSUM
ATTN: J D ROGERS
ATTN: T BERGSTRESSER
ATTN: TECH LIB

OTHER GOVERMENT

CENTRAL INTELLIGENCE AGENCY
ATTN: OSWR/NED 5S09 NHB

DEPARTMENT OF DEFENSE CONTRACTORS

ANALYTIC SERVICES, INC. (ANSER)
ATTN: K BAKER

APPLIED RESEARCH ASSOCIATES, INC.
ATTN: C J HIGGINS

APPLIED RESEARCH ASSOCIATES, INC.
ATTN: S BLOUIN

APPLIED RESEARCH ASSOCIATES, INC.
ATTN: R FRANK

APPLIED THEORY, INC.
2 CY ATTN: JOHN G TRULIO

APTEK, INC.
ATTN: B LEWIS
ATTN: Y MURRY

BOEING TECHNICAL & MANAGEMENT SVCS, INC.
ATTN: M/S 3H-29, W M LEAVENS
ATTN: MS 3W-41, A W SPENCER
ATTN: R BRYAN CAIRNS M/S 8H-05

ITT RESEARCH INSTITUTE
ATTN: DOCUMENTS LIBRARY
ATTN: M JOHNSON

JAYCOR
2 CY ATTN: CYRUS P KNOWLES

KAMAN SCIENCES CORP.
ATTN: RICHARD KEEFFE

KAMAN SCIENCES CORPORATION
ATTN: DASIAC
ATTN: DASIAC/DARE

LACHEL AND ASSOCIATES, INC
ATTN: C LINAMEN
ATTN: J BECK

LOGICON R AND D ASSOCIATES
ATTN: DR T A PUCIK
ATTN: LIBRARY

LOGICON R AND D ASSOCIATES
ATTN: E HUMPHREYS

MAXWELL TECHNOLOGIES, INC
ATTN: K D PYATT, JR

NTS ENGINEERING
ATTN: S SHORT

PACIFIC-SIERRA RESEARCH CORP.
ATTN: H BRODE

PACIFIC-SIERRA RESEARCH CORP.
ATTN: D GORMLEY

SCIENCE APPLICATIONS INTL CORP
ATTN: H PRATT
ATTN: TECHNICAL REPORT
SYSTEM

SCIENCE APPLICATIONS INTL CORP
ATTN: W LAYSON

SOUTHWEST RESEARCH INSTITUTE
ATTN: B THACKER

SRI INTERNATIONAL
2 CY ATTN: DR JIM GRAN
2 CY ATTN: MARK A GROETHE

THE AEROSPACE CORP
ATTN: LIBRARY ACQ M1/199

TITAN CORPORATION
ATTN: J THOMSEN

TITAN CORPORATION
ATTN: LIBRARY
ATTN: S SCHUSTER
ATTN: Y M ITO

TRW SPACE & DEFENSE SECTOR
SPACE
ATTN: OUT6, W WAMPLER

UTD, INC.
ATTN: E FOSTER

WEIDLINGER ASSOCIATES, INC.
ATTN: E WONG
ATTN: H LEVINE

WEDLINGER ASSOCIATES, INC
ATTN: I SANDLER